

AFWAL-TR-86-3030
VOLUME I

AD-A259 188



2

FATIGUE CRACK GROWTH AND RETARDATION DUE TO OVERLOADS IN METAL-MATRIX COMPOSITES

Volume I - Fatigue Crack Growth in Boron-Aluminum
Metal-Matrix Composites

C. T. Sun, J. F. Doyle and S. Rizzi
School of Aeronautics and Astronautics
Purdue University
West Lafayette, IN 47907

DTIC
ELECTE
DEC 29 1992
S A D

August 1986

Final Report for June 1982 to December 1985

Approved for public release; distribution unlimited



92-32875

FLIGHT DYNAMICS LABORATORY
AIR FORCE WRIGHT AERONAUTICAL LABORATORIES
AIR FORCE SYSTEMS COMMAND
WRIGHT-PATTERSON AIR FORCE BASE, OHIO 45433-6553

92 12 28 035

NOTICE

WHEN GOVERNMENT DRAWINGS, SPECIFICATIONS, OR OTHER DATA ARE USED FOR ANY PURPOSE OTHER THAN IN CONNECTION WITH A DEFINITELY GOVERNMENT-RELATED PROCUREMENT, THE UNITED STATES GOVERNMENT INCURS NO RESPONSIBILITY OR ANY OBLIGATION WHATSOEVER. THE FACT THAT THE GOVERNMENT MAY HAVE FORMULATED OR IN ANY WAY SUPPLIED THE SAID DRAWINGS, SPECIFICATIONS, OR OTHER DATA, IS NOT TO BE REGARDED BY IMPLICATION, OR OTHERWISE IN ANY MANNER CONSTRUED, AS LICENSING THE HOLDER, OR ANY OTHER PERSON OR CORPORATION; OR AS CONVEYING ANY RIGHTS OR PERMISSION TO MANUFACTURE, USE, OR SELL ANY PATENTED INVENTION THAT MAY IN ANY WAY BE RELATED THERETO.

THIS REPORT HAS BEEN REVIEWED BY THE OFFICE OF PUBLIC AFFAIRS (ASD/PA) AND IS RELEASABLE TO THE NATIONAL TECHNICAL INFORMATION SERVICE (NTIS). AT NTIS IT WILL BE AVAILABLE TO THE GENERAL PUBLIC INCLUDING FOREIGN NATIONS.

THIS TECHNICAL REPORT HAS BEEN REVIEWED AND IS APPROVED FOR PUBLICATION.



GEORGE P. SENDECKYJ, Aero Engr
Fatigue, Fracture & Reliability Grp
Structural Integrity Branch



KEVIN L. BOYD, Actg Tech Mgr
Fatigue, Fracture & Reliability Grp
Structural Integrity Branch

FOR THE COMMANDER



JAMES L. RUDD, Chief
Structural Integrity Branch
Structures Division

IF YOUR ADDRESS HAS CHANGED, IF YOU WISH TO BE REMOVED FROM OUR MAILING LIST, OR IF THE ADDRESSEE IS NO LONGER EMPLOYED BY YOUR ORGANIZATION PLEASE NOTIFY WL/FIBEC, WRIGHT-PATTERSON AFB, OH 45433-6553 TO HELP MAINTAIN A CURRENT MAILING LIST.

COPIES OF THIS REPORT SHOULD NOT BE RETURNED UNLESS RETURN IS REQUIRED BY SECURITY CONSIDERATIONS, CONTRACTUAL OBLIGATIONS, OR NOTICE ON A SPECIFIC DOCUMENT.

UNCLASSIFIED

SECURITY CLASSIFICATION OF THIS PAGE

REPORT DOCUMENTATION PAGE

1a. REPORT SECURITY CLASSIFICATION UNCLASSIFIED			1b. RESTRICTIVE MARKINGS N/A		
2a. SECURITY CLASSIFICATION AUTHORITY N/A			3. DISTRIBUTION/AVAILABILITY OF REPORT APPROVED FOR PUBLIC RELEASE; DISTRIBUTION UNLIMITED		
2b. DECLASSIFICATION/DOWNGRADING SCHEDULE N/A			5. MONITORING ORGANIZATION REPORT NUMBER(S) AFWAL-TR-86-3030, Vol. I		
4. PERFORMING ORGANIZATION REPORT NUMBER(S)			7a. NAME OF MONITORING ORGANIZATION Air Force Wright Aeronautical Laboratories Flight Dynamics Laboratory AFWAL/FIBEC		
6a. NAME OF PERFORMING ORGANIZATION Purdue University		6b. OFFICE SYMBOL (If applicable)		7b. ADDRESS (City, State and ZIP Code) W-PAFB, OH 45433-6553	
6c. ADDRESS (City, State and ZIP Code) West Lafayette, IN 47907		8a. NAME OF FUNDING/SPONSORING ORGANIZATION Flight Dynamics Laboratory		8b. OFFICE SYMBOL (If applicable) AFWAL/FIBEC	
6c. ADDRESS (City, State and ZIP Code) AFWAL/FIBEC W-PAFB, OH 45433-6553		9. PROCUREMENT INSTRUMENT IDENTIFICATION NUMBER F33615-82-K-3218			
11. TITLE (Include Security Classification) see block 16		10. SOURCE OF FUNDING NOS			
		PROGRAM ELEMENT NO. 61102F		PROJECT NO. 2307	
				TASK NO. N1	
				WORK UNIT NO. 20	
12. PERSONAL AUTHOR(S) C.T. Sun, J.F. Dogle and S.A. Rizzi					
13a. TYPE OF REPORT FINAL		13b. TIME COVERED FROM June 82 TO Dec 85		14. DATE OF REPORT (Yr., Mo., Day) August 1986	
				15. PAGE COUNT 134	
16. SUPPLEMENTARY NOTATION FATIGUE CRACK GROWTH AND RETARDATION DUE TO OVERLOADS IN METAL-MATRIX COMPOSITES. Vol. I - FATIGUE CRACK GROWTH IN BORON-ALUMINUM METAL-MATRIX COMPOSITES					
17. COSATI CODES			18. SUBJECT TERMS (Continue on reverse if necessary and identify by block number)		
FIELD	GROUP	SUB. GR.	METAL-MATRIX COMPOSITES, BORON-ALUMINUM, CRACK GROWTH, CRACK RETARDATION, FATIGUE		
11	04				
19. ABSTRACT (Continue on reverse if necessary and identify by block number)					
<p>The fatigue crack growth in a Boron-Aluminum metal matrix composite is investigated. The material consists of 11 plies of diffusion bonded 5.6 mil boron fibers in a 6061 aluminum matrix. In this study, the composite is characterized as an orthotropic elastic-plastic material using uniaxial test specimens. The constraint effect of the plasticity encountered in specimens with stress gradients is characterized using a tapered specimen. The modeling is verified on a specimen with a centered circular hole and specimens with transverse and oblique fatigue cracks.</p> <p>A series of baseline fatigue tests are performed on transverse and oblique fatigue cracks. The baseline tests are run at room temperature using a 10 Hz sinusoidal loading with a minimum applied load near zero. An effective stress intensity factor is developed to correlate all the baseline fatigue data.</p> <p>Overload tests are carried out on transverse and oblique cracked specimens. The specimens are cycled as was done in the baseline tests, and a single tensile overload was performed. Cyclic loading to near failure followed. The post-overload crack growth behavior first accelerates, then decelerates. This crack growth eventually assumes its pre-overload state.</p>					
20. DISTRIBUTION/AVAILABILITY OF ABSTRACT UNCLASSIFIED/UNLIMITED <input checked="" type="checkbox"/> SAME AS RPT <input checked="" type="checkbox"/> DTIC USERS <input type="checkbox"/>			21. ABSTRACT SECURITY CLASSIFICATION UNCLASSIFIED		
22a. NAME OF RESPONSIBLE INDIVIDUAL GEORGE P. SENDECKYJ			22b. TELEPHONE NUMBER (Include Area Code) (513) 255-6104		22c. OFFICE SYMBOL AFWAL/FIBEC

FOREWORD

This report was prepared in the School of Aeronautics and Astronautics, Purdue University, West Lafayette, Indiana. The work was performed under Contract No. F33615-82-K-3218.

The work reported herein was performed during the period June 1982 to December 1985. Dr. C.T. Sun and Dr. J.F. Doyle are professors and S.A. Rizzi is a graduate student, all from the School of Aeronautics and Astronautics at Purdue University.

Accession For	
NTIS CRA&I	<input checked="" type="checkbox"/>
DTIC TAB	<input type="checkbox"/>
Unannounced	<input type="checkbox"/>
Justification	
By	
Distribution /	
Availability Codes	
Dist	Avail and/or Special
A-1	

TABLE OF CONTENTS

	Page
SECTION 1: INTRODUCTION.	1
SECTION 2: CHARACTERIZATION OF BORON/ALUMINUM.	3
CHARACTERIZATION FOR UNCONSTRAINED PLASTICITY.	3
CHARACTERIZATION FOR CONSTRAINED PLASTICITY.	6
Experimental Setup and Data Acquisition.	6
Calibration.	7
TAPERED SPECIMEN	10
SPECIMEN WITH A CENTERED CIRCULAR HOLE	11
Elastic Analysis	12
Elastic Results.	13
Elastic-Plastic Analysis	13
Elastic-Plastic Results.	14
SPECIMEN WITH A TRANSVERSE CRACK	15
SPECIMEN WITH AN OBLIQUE CRACK	16
DISCUSSION	17
SECTION 3: BASELINE FATIGUE.	44
FATIGUE SPECIMEN DESIGN.	44
Design Criterion	46
Data Acquisition	47
Fatigue Precracking.	48
90 DEGREE BASELINE TESTS	49
45 DEGREE BASELINE TESTS	52
15 DEGREE BASELINE TESTS	52

TABLE OF CONTENTS (Concluded)

	Page
PRELIMINARY DATA REDUCTION	55
DISCUSSION	56
SECTION 4: DATA REDUCTION AND CORRELATION.	72
ANISOTROPIC STRESS INTENSITY FACTOR FORMULATION.	72
Near Field Interpretation of K Effective	74
Computation of K Effective	78
STRESS INTENSITY FACTOR CALIBRATION.	79
CRACK GROWTH PREDICTION.	82
Determination of a_{66}	82
Paris Law Parameters	83
Computer Modelling	83
DISCUSSION	85
SECTION 5: OVERLOAD TESTS.	97
90 DEGREE OVERLOAD TESTS	97
45 DEGREE OVERLOAD TESTS	100
15 DEGREE OVERLOAD TESTS	101
CORRELATION OF OVERLOAD EFFECTS.	102
Change in Crack Growth Rate.	103
Change in Life	103
DISCUSSION	104
SECTION 6: SUMMARY AND RECOMMENDATIONS.	116
Recapitulation of Major Results.	116
Recommendations for Further Study.	119
LIST OF REFERENCES.	121

LIST OF FIGURES

Figure	Page
2.1 Effective stress versus effective plastic strain.	20
2.2 Stress versus longitudinal strain for various fiber orientations.	21
2.3 Stress versus longitudinal strain for various fiber orientations shown on a reduced scale	22
2.4 Transverse versus longitudinal strain for various fiber orientations. The different orientations are vertically displaced for clarity.	23
2.5 Transverse versus longitudinal strain for various fiber orientations shown on a reduced scale. The different orientations are vertically displaced for clarity	24
2.6 Photograph of the experimental setup used for the material characterization	25
2.7 Calibration of Daytronics Data Acquisition System using a cantilever beam. (a) Applied force versus the Wheatstone bridge voltage. (b) Daytronics output versus Wheatstone bridge voltage.	26
2.8 Schematic of the tapered specimen, B25.	27
2.9 Stress-strain and strain-strain relationships for the tapered specimen. (a) Net section stress versus longitudinal strain. (b) Transverse versus longitudinal strain. The data for the 45 degree coupon specimen is included for comparison.	28
2.10 Schematic of the specimen with a circular hole, D4.	29
2.11 Longitudinal and transverse strain variation with distance from the edge of the hole. The remote load is 400 lb.	30
2.12 Strain history from gages along a line 90 degrees to the loading. Notice the high residual strains near the edge of the hole.	31

LIST OF FIGURES (Continued)

Figure		Page
2.13	Longitudinal strain variation along a line 90 degrees to the loading. (a) Loaded State, (b) Residuals from prior loading.	35
2.14	Transverse strain variation along a line 90 degrees to the loading. (a) Loaded State, (b) Residuals from prior loading.	36
2.15	Longitudinal, transverse, and shear strain components at the delta rosette in the (a) Loaded State and (b) Residuals from prior loading.	37
2.16	Schematic for the specimen with a transverse crack, B26	38
2.17	Strain history at the gages of specimen B26 during a 1.5 overload. Notice that gage 1 failed during the test.	39
2.18	Schematic for the specimen with an oblique crack, B27	41
2.19	Strain history at the gages of specimen B27 during a 1.5 overload.	42
3.1	Specimen cutting plan for plates A and B, in (a) and (b), respectively	59
3.2	Specimen cutting plan for plates C and D, in (a) and (b), respectively	60
3.3	Some typical fatigue specimens. 90, 45, and 15 degree specimens shown in (a), (b), and (c), respectively.	61
3.4	Fatigue specimen design curves for 90, 45, and 15 degree orientations in (a), (b), and (c), respectively. Hatched areas represent the design region.	62
3.5	Photograph of the experimental setup used in the fatigue testing. A travelling microscope was used to measure the crack length and the MTS recorded the cycles	63
3.6	Crack growth data for 90 degree baseline tests. (a) Specimen A10 - $\Delta\sigma = 9537$ psi, $R = 0.01$. (b) Specimen C2 - $\Delta\sigma = 6430$ psi, $R = 0.03$. (c) Specimen C3 - $\Delta\sigma = 7280$ psi, $R = 0.03$	64

LIST OF FIGURES (Continued)

Figure	Page
3.7 Crack growth data for 45 degree baseline specimen D1. $\Delta\sigma = 6,800$ psi, $R = 0.03$	65
3.8 Crack growth data for 15 degree baseline tests. (a) Specimen A2 - $\Delta\sigma = 10,784$ psi, $R = 0.01$. (b) Specimen C6 - $\Delta\sigma = 9,681$ psi, $R = 0.03$. (c) Specimen C7 - $\Delta\sigma = 12,180$ psi, $R = 0.03$. (d) Specimen C8b - $\Delta\sigma = 12,800$ psi, $R = 0.02$. (e) Specimen C9 - $\Delta\sigma = 13,300$ psi, $R = 0.01$	66
3.9 Crack growth rate data for 90 degree baseline tests. (a) Specimen A10 - $\Delta\sigma = 9537$ psi, $R = 0.01$. (b) Specimen C2 - $\Delta\sigma = 6430$ psi, $R = 0.03$. (c) Specimen C3 - $\Delta\sigma = 7280$ psi, $R = 0.03$	68
3.10 Crack growth rate data for 45 degrees baseline specimen D1. $\Delta\sigma = 6,800$ psi, $R = 0.03$	69
3.11 Crack growth rate data for 15 degree baseline tests. (a) Specimen A2 - $\Delta\sigma = 10,784$ psi, $R = 0.01$. (b) Specimen C6 - $\Delta\sigma = 9,681$ psi, $R = 0.03$. (c) Specimen C7 - $\Delta\sigma = 12,180$ psi, $R = 0.03$. (d) Specimen C8b - $\Delta\sigma = 12,800$ psi, $R = 0.02$. (e) Specimen C9 - $\Delta\sigma = 13,300$ psi, $R = 0.01$	70
4.1 $K_I/\sigma\sqrt{\pi a}$ versus (a/w) . The lines represent equation (3.27).	87
4.2 $K_{II}/\sigma\sqrt{\pi a}$ versus (a/w) . The lines represent equation (3.28).	88
4.3 $\log_{10} da/dN$ vs $\log_{10} \sigma\sqrt{\pi a}$ for the 90, 45, and 15 degree baseline fatigue data	89
4.4 $\log_{10} da/dN$ vs $\log_{10} \bar{K}$ for the 90, 45, and 15 degree baseline fatigue data. Notice that the three sets of data collapse onto a single curve. The data from 6061-T651 aluminum is shown for comparison	90
4.5 Crack growth data for 90 degree baseline tests. (a) Specimen A10 - $\Delta\sigma = 9537$ psi, $R = 0.01$. (b) Specimen C2 - $\Delta\sigma = 6430$ psi, $R = 0.03$. (c) Specimen C3 - $\Delta\sigma = 7280$ psi, $R = 0.03$	91

LIST OF FIGURES (Continued)

Figure

Page

4.6	Crack growth rate data for 90 degree baseline tests. (a) Specimen A10 - $\Delta\sigma = 9537$ psi, $R = 0.01$. (b) Specimen C2 - $\Delta\sigma = 6430$ psi, $R = 0.03$. (c) Specimen C3 - $\Delta\sigma = 7280$ psi, $R = 0.03$	92
4.7	Crack growth data for 45 degree baseline specimen D1. $\Delta\sigma = 6,800$ psi, $R = 0.03$	93
4.8	Crack growth rate data for 45 degree baseline specimen D1. $\Delta\sigma = 6,800$ psi, $R = 0.03$	94
4.9	Crack growth data for 15 degree baseline tests. (a) Specimen C8b - $\Delta\sigma = 12,800$ psi, $R = 0.02$. (b) Specimen C9 - $\Delta\sigma = 13,300$ psi, $R = 0.01$	95
4.10	Crack growth rate data for 15 degree baseline tests. (a) Specimen C8b - $\Delta\sigma = 12,800$ psi, $R = 0.02$. (b) Specimen C9 - $\Delta\sigma = 13,300$ psi, $R = 0.01$	96
5.1	Crack growth data for 90 degree overload tests. (a) Specimen A11 - $\Delta\sigma = 9370$ psi, $R = 0.01$. (b) Specimen A12 - $\Delta\sigma = 9313$ psi, $R = 0.01$. (c) Specimen A13 - $\Delta\sigma = 9313$ psi, $R = 0.01$. (d) Specimen C1 - $\Delta\sigma = 5780$ psi, $R = 0.04$. (e) Specimen C4 - $\Delta\sigma = 5780$ psi, $R = 0.04$. (f) Specimen C5 - $\Delta\sigma = 5780$ psi, $R = 0.04$	106
5.2	Crack growth rate data for 90 degree overload tests. (a) Specimen A11 - $\Delta\sigma = 9370$ psi, $R = 0.01$, 1.5x overload (b) Specimen A12 - $\Delta\sigma = 9313$ psi, $R = 0.01$, 1.5x overload (c) Specimen A13 - $\Delta\sigma = 9313$ psi, $R = 0.01$, 2.0x overload (d) Specimen C1 - $\Delta\sigma = 5780$ psi, $R = 0.04$, 1.25x overload (e) Specimen C4 - $\Delta\sigma = 5780$ psi, $R = 0.04$, 1.35x overload (f) Specimen C5 - $\Delta\sigma = 5780$ psi, $R = 0.04$, 1.45x overload	108
5.3	Crack growth data for 45 degree overload tests. (a) Specimen D2 - $\Delta\sigma = 6800$ psi, $R = 0.03$. (b) Specimen D3 - $\Delta\sigma = 6800$ psi, $R = 0.03$	110
5.4	Crack growth rate data for 45 degree overload tests. (a) Specimen D2 - $\Delta\sigma = 6800$ psi, $R = 0.03$, 1.25x overload (b) Specimen D3 - $\Delta\sigma = 6800$ psi, $R = 0.03$, 1.35x overload	111

LIST OF FIGURES (Concluded)

Figure		Page
5.5	Crack growth data for 15 degree overload tests. (a) Specimen C10 - $\Delta\sigma = 12,800$ psi, $R = 0.02$. (b) Specimen B29 - $\Delta\sigma = 12,800$ psi, $R = 0.02$. (c) Specimen B28 - $\Delta\sigma = 12,800$ psi, $R = 0.02$	112
5.6	Crack growth rate data for 15 degree overload tests. (a) Specimen C10 - $\Delta\sigma = 12,800$ psi, $R = 0.02$, 1.25x overload (b) Specimen B29 - $\Delta\sigma = 12,800$ psi, $R = 0.02$, 1.61x overload (c) Specimen B28 - $\Delta\sigma = 12,800$ psi, $R = 0.02$, 1.92x overload.	113
5.7	Change in crack growth rate as a function of the overload for the three specimen geometries.	114
5.8	Change in life due to the overload as a function of the overload for the three specimen geometries.	115

LIST OF TABLES

Table	Page
2.1 A summary of the mechanical properties of B/A1.	18
2.2 Strain gage positions for the specimen with a centered circular hole.	19
3.1 A listing of fatigue and characterization specimens cut from plates A and B as shown in Figure 2.1.	57
3.2 A listing of fatigue and characterization specimens cut from plates C and D as shown in Figure 2.2.	58
4.1 Summary of finite element data for SIF calibration.	86
5.1 Change in fatigue crack growth rate after overload.	105

SECTION 1

INTRODUCTION

Metal matrix composites (MMC) have demonstrated their practicality for use in aerospace structures through extensive study in recent years. Their high impact resistance and good thermal and electrical conductivities allow them to be utilized in applications not suited for polymer matrix composites.

The MMC of interest in this research is a unidirectional Boron-Aluminum (B/Al) composite. In particular, the fatigue crack growth is investigated. A prerequisite for this is the material characterization. Kenaga [1] has successfully characterized B/Al as an elastic-plastic orthotropic material using the usual elastic formulation (see Jones [2]) and a plastic formulation based on the anisotropic plastic flow rule proposed by Kachanov [3]. His results are reviewed with the objective of obtaining more accurate elastic and plastic constants. The constraint effect on plasticity observed in [1] is further investigated.

A stress analysis of discontinuities in B/Al is undertaken. A knowledge of the state of stress and strain at discontinuities will aid in understanding the fatigue crack growth behavior. In the past, fracture criterion have been proposed for B/Al having various discontinuities by Mar and Lin [4] and Adsit and Waszczak [5]. In the present study, a specimen with a centered circular hole is used to obtain experimental data and compared to concurrent work by Leewood [6] using

a finite element method (FEM). The work by Kenaga [1] on transverse and oblique fatigue cracks is re-examined and compared with the FEM results.

Although Peters [7] argues that concepts of linear elastic fracture mechanics (LEFM) are not applicable to MMC's, this approach is nevertheless used since work by Awerbuch and Hahn [8, 9, 10, and 11] on the fracture properties of unidirectional B/Al and Bsic/Ti substantiate the applicability of LEFM. Aside from the fatigue work performed by Kenaga [1] on unidirectional B/Al, the only other known studies in this area are by Kendall [12] and Simonds [13].

Baseline fatigue tests on specimens with single edge notches are performed to collect crack growth data. Transverse and off-axis tests are performed. Awerbuch and Hahn, and Konish [14] found that the isotropic stress intensity factor solution can be used for orthotropic materials with transverse cracks provided an orthotropy correction factor is used. This approach is extended to correlate the off-axis data with the transverse data.

Overload tests are also performed on transverse and off-axis specimens in which a single tensile overload is applied. The crack growth data is collected. The acceleration and deceleration effects following the overload as found by Kenaga [1] are further investigated. An attempt is made to correlate the amount of overload with the acceleration and deceleration for the various geometries.

With the FEM [6] and experimental data collected, an outline for further research is written so that the fatigue crack growth and overload effects may be described in terms of micromechanical behavior and crack tip plasticity.

SECTION 2: CHARACTERIZATION OF BORON/ALUMINUM

The material, Boron/Aluminum metal-matrix composite, was previously characterized as being orthotropic elastic-plastic [1]. This characterization is reconsidered for constrained plasticity.

CHARACTERIZATION FOR UNCONSTRAINED PLASTICITY

A characterization of the material was performed using stress-strain data obtained from a series of uniaxial tests with the fibers at orientations of 0, 10, 20, 30, 45, 60, and 90 degrees to the load [1]. The elastic constants are [1]:

$$\begin{aligned} E_1 &= 29.4 \text{ ksi} & E_2 &= 19.1 \text{ ksi} \\ \nu_{12} &= 0.169 & G_{12} &= 7.49 \text{ ksi} \end{aligned} \quad (2.1)$$

The plastic orthotropic formulation gives the following equations for the effective stress, effective plastic strain, and the plastic Poisson's ratio effect [1]:

$$\begin{aligned} \bar{\sigma} &= 3/2 \sqrt{r_{11}\sigma_{11}^2 + \sigma_{22}^2 + 2r_{12}\sigma_{11}\sigma_{22} + 2r_{66}\sigma_{12}^2} \\ \left[d\bar{\epsilon}^p \right]^2 &= 2/3 \left[de_{11}^p{}^2 + r_{11}de_{22}^p{}^2 - 2r_{12}de_{11}^p de_{22}^p \right. \\ &\quad \left. + 2(r_{11} - r_{12}^2) de_{12}^p{}^2 / r_{66} \right] / [r_{11} - r_{12}^2] \end{aligned} \quad (2.2)$$

$$\frac{de^p_{T\theta}}{de^p_{\theta}} = \frac{(r_{11} + 1 - 2r_{66})\sin^2\theta\cos^2\theta + r_{12}(\sin^4\theta + \cos^4\theta)}{r_{11}\cos^4\theta + \sin^4\theta + 2(r_{12} + r_{66})\sin^2\theta\cos^2\theta}$$

where the r values are coefficients which describe the amount of anisotropy in the plasticity. The r values are determined by a trial and error approach using a computer program called EFF.F, which calculates the effective plastic strain and effective stress from the plastic stress-strain experimental data. The r values are changed so that the effective stress-strain curves collapse onto a single curve for the different angles. The r values are found to be:

$$\begin{aligned} r_{11} &= 0.001 & (\text{no units}) \\ r_{12} &= -0.01 \\ r_{66} &= 1.9 \end{aligned} \tag{2.3}$$

The effective stress versus the effective plastic strain is shown in Figure 1.1.

A three parameter work hardening model is employed and has the form [1],

$$\bar{\epsilon}^p = \begin{cases} 0 & : \bar{\sigma} \leq \bar{\sigma}_y \\ (\bar{\sigma}/A)^B - (\bar{\sigma}_y/A)^B & : \bar{\sigma} \geq \bar{\sigma}_y \end{cases} \tag{2.4}$$

The work hardening parameters are chosen so that they model the collapsed effective stress versus effective plastic strain curve. This

is done by trial and error. The work-hardening parameters are found to be:

$$\begin{aligned} A &= 60 \text{ ksi.} \\ B &= 5.8 \\ \bar{\sigma}_y &= 13.5 \text{ ksi.} \end{aligned} \tag{2.5}$$

The solid line in Figure 2.1 represents the resulting model.

Note that the r vales are different from those in [1] which reports values of 0.017, -0.01, and 1.8, for r_{11} , r_{12} , and r_{66} , respectively. Also, the work hardening parameters differ from those in [1] which reports values of $A = 64$ ksi, $B = 5.8$, and $\sigma_y = 14.5$ ksi. There are two reasons for these differences. First, the 65 degree data were dismissed as erroneous since the elastic analysis indicated an elastic Poisson's ratio of 0.656, which is very much higher than the others. Secondly, the curve-fit was performed on an effective plastic strain range from 0 to 5,000 micro-strain and effective stress range from 0 to 25 ksi. In [1], the effective plastic strain range was from 0 to 100,000 micro-strain and an effective stress range from 0 to 50 ksi.

The equations for the elastic-plastic orthotropic characterization were put into a computer program called UNIAX.F [1]. This program was then used to model the experimental data with the values found above. The stress versus longitudinal strain is plotted in Figure 2.2 for the full range of the data and UNIAX model. It is seen that UNIAX models the data very well. In a close-up view of the above

plot near the linear region, Figure 2.3, UNIAX is seen to also do well. Notice that as the angle increases from 0 to 90 degrees, the curves show less and less work-hardening until a minimum at 60 degrees, and then more for the 90 degree curve. The transverse strain versus longitudinal strain is plotted in Figure 2.4. The curves are displaced for clarity. Again, UNIAX does well in modelling the data. The close-up view of the above plot, Figure 2.5, shows the same result. A summary of the mechanical properties is found in Table 2.1.

CHARACTERIZATION FOR CONSTRAINED PLASTICITY

In cases other than those of uniform stress, there is a constraining effect on the plasticity caused by the elastic fibers penetrating the plastic zone [1]. In order to model this behavior, a finite element analysis is needed. A tapered specimen is employed to produce a constraint effect in a nearly uniaxial state of stress [1]. Consideration of the constraint effect in a multi-axial state of stress uses a specimen with a centered circular hole, a specimen with a transverse fatigue crack [1], and a specimen with an oblique fatigue crack [1]. The experimental results are compared with the finite element analysis using ANPLAST [6].

Experimental Setup and Data Acquisition

A photograph of the experimental setup is shown in Figure 2.6. The gaged specimen is placed in the MTS 810. An eight channel Daytronics data acquisition system and a ten channel Vishay/Ellis strain indicator are used for the data acquisition.

In the Vishay/Ellis system, the active gages are wired into arm 1 of an external half Wheatstone bridge. Gages of the same resistance

mounted to another piece of Boron/Aluminum stock are wired into arm 2 of the bridge for temperature compensation. The strains are read directly and printed on a hard-copy output.

In the Daytronics system, the active gages are wired into arm 1 of an external half Wheatstone bridge and compensation gages into arm 2. The system provides an adjustable internal excitation and indicates on an LED the output in millivolts per volt of excitation. In addition, an RS232 port on the Daytronics is connected to an auxilliary RS232 port on the SAGE II computer. The SAGE II computer has an MC68000 microprocessor and runs the UCSD P-system operating system. A multi-purpose communications program called PASSAGE [15] is executed to establish the communications protocol. When the Daytronics is cycled, i.e. each channel scanned, the data are transferred to the SAGE II and stored on floppy disk. Using the same communications package, the data are later transferred to a DUAL VAX 11/780 UNIX for data reduction.

Calibration

The calibration of the Vishay/Ellis system was verified using a cantilever beam setup. This was accomplished by comparing the strain indicated by the Vishay/Ellis with that predicted from simple beam theory. The cantilever beam was aluminum with dimensions 0.091 inch thick by 1 inch wide. The distance from the gage to the applied load was 7.44 inches. From simple beam theory,

$$e = \frac{M y}{E I} \quad (2.6)$$

where

e = strain

M = applied moment = 7.44 F (inch-lbs)

F = applied force (lbs)

y = distance from the mid-plane of the beam = 0.046 (inch)

E = Modulus of Elasticity = 10×10^6 (psi)

I = Moment of Inertia = 62.80×10^{-6} (inch⁴)

For an applied force of 1.1 and 2.1 lbs., the theory predicts 593 and 1132 micro-strain, respectively. The Vishay/Ellis indicated strains of 580 and 1000 micro-strain, respectively. This was sufficient to give confidence in the way the Vishay/Ellis system was set up.

The Daytronics system was calibrated using a setup similar to the Vishay/Ellis calibration. A stand alone Wheatstone bridge was wired with the active cantilever gage (350 ohm and gage factor = 2.11) in arm 1 and three 350 ohm gages in arms 2, 3, and 4. A constant voltage source was used for the bridge excitation and a digital multimeter was used to read the output voltage. The equation for the Wheatstone bridge circuit is [16]:

$$\frac{\Delta E}{V} = \frac{r}{(1 + r)^2} \left[\frac{\Delta R_1}{R_1} - \frac{\Delta R_2}{R_2} + \frac{\Delta R_3}{R_3} - \frac{\Delta R_4}{R_4} \right] \quad (2.7)$$

where

ΔE = change in output voltage

V = excitation voltage

Having $r = \frac{R_2}{R_1} = \frac{R_3}{R_4} = 1$, and R_2 , R_3 , and R_4 fixed reduces (2.7) to:

$$\frac{\Delta E}{V} = \frac{1}{4} \left[\frac{\Delta R_1}{R_1} \right] \quad (2.8)$$

The strain is computed from:

$$e = \left[\frac{\Delta R_1}{R_1} \right] \frac{1}{S_g} = 4 \left[\frac{\Delta E}{V} \right] \frac{1}{S_g} \quad (2.9)$$

where

S_g = gage factor

A series of loadings were applied to the beam and the output in millivolts per volt of excitation was recorded. The data are plotted in Figure 2.7. The straight line represents a least-squares fit of the data. The strain calculated from Equation (2.9) corresponds with the elementary theory. The gage was next wired to the external half-bridge of the Daytronics and a load of 2.11 lbs was applied to the beam. The internal excitation of the Daytronics was set at 2 volts, and the transducer was adjusted so that the Daytronics indicated the same output in millivolts per volt of excitation as the least-squares fit of Figure 2.7. A series of loads were applied and the Daytronics output recorded. These are plotted against the Wheatstone bridge data in Figure 2.7. The solid line is a 45 degree line upon which the data should fall. Since the actual experiments used 120 ohm gages, a

cantilever beam with a 120 ohm gage was used to verify that the output is independent of the gage used. The data are seen to fall on the 45 degree line in Figure 2.7. The calibration was thus completed.

A computer program, called DATARED.F, was written to compute the strains from the Daytronics output. The required input is the Daytronics voltage, the gage factor, and the zero readings. Equation (2.9) is used to compute the strains.

TAPERED SPECIMEN

A tapered specimen is the simplest case of constrained plasticity. Consequently, the tapered specimen studied in [1] was reconsidered to try and understand constrained plasticity. A schematic of the tapered specimen is shown in Figure 2.8.

The longitudinal strains are plotted against the net section stress in Figure 2.9. Also plotted are the data from the 45 degree coupon specimen. The UNIAX model using the newly found properties and work-hardening parameters models the 45 degree coupon data well, as seen by the short dashed line in Figure 2.9. However, it does not model the tapered data accurately. Since the state of stress is very close to being uniaxial, then the difference between the tapered specimen and the uniaxial one must be due to a constraining effect on the plasticity caused by the long fibers. That is, while the specimen yields at higher loads for larger cross sectional areas, fibers generally extend into both elastic and plastic regions. The portion of the fibers in the elastic region cause a constraint because they do not allow the yielded material to flow freely.

This constraining effect can be compensated for by increasing the slope of the work-hardening curve. Whereas in the uniaxial situation the slope $B = 5.8$ models the data well, in the constrained case a value of $B = 7.2$ models the data well, as seen by the solid line in Figure 2.9. The finite element results [6] are plotted as the long dashed line.

A plot of the transverse versus longitudinal strain at gage 2 is shown in Figure 2.9. Note that data from gages 1 and 3 are interpolated to get the longitudinal strain at gage 2. The UNIAX model results are drawn as the solid line for $B = 7.2$ and as the dashed line for $B = 5.8$. Since there is little difference in the data and models, it may be concluded that the constraint effect does not change the relationship between the longitudinal and transverse strains significantly, that is, it is an effect associated with the relationship between the stress and longitudinal strain only. This supports the approach of modifying only the work-hardening.

SPECIMEN WITH A CENTERED CIRCULAR HOLE

It was desired to conduct an experiment which had the constraint effect of the fibers in a multi-axial state of stress. The motivation for this was to verify the elastic-plastic characterization for a multi-axial state of stress and to see if the new work-hardening parameter is valid for this state of stress. This is important to know because in the study of cracks, both of these conditions exist. A specimen with a circular hole was chosen for the analysis.

The specimen, D4, was cut from plate D using the same milling machine that was used to cut the fatigue specimens. A 0.75 inch

diameter circular brass electrode was used to cut the hole by EDM. Aluminum tabs were glued on to protect the material from the grips of the MTS. A schematic of the hole specimen is shown in Figure 2.10. Strip gages were chosen to be close to the hole as it is a stress concentration and would have a high strain gradient. Two strip gages were cut in half and mounted on the front and rear faces of the specimen at 0 and 90 degrees to the loading in order to pick up both longitudinal and transverse strain components at a given point. Away from the concentration, tee-stacked gages were chosen to give both components at these points. These did not have to be as small as the strip gages. A delta-rosette was also mounted at 30 degrees from the horizontal to obtain the state of stress at a point. The gage locations are tabulated in Table 2.2.

Elastic Analysis

Since a total of eighteen channels were available and 29 gages were mounted, not all gages could be monitored during the test. Therefore a preliminary study was conducted to determine which gages would be of most interest in an elastic-plastic analysis. The tests, all elastic, involved loading the specimen to 400 lbs and recording the data. The finite element analysis [6] indicated that a remote load of 400 lbs was about 50% of yield. In the first test, the remote gage, gage 26, and the longitudinal gages at 90 degrees, i.e., gages 1-7, were monitored. In the second test, the remote gage and the transverse gages at 90 degrees, i.e., gages 8-14, were monitored. In the third test, the remote gage and the longitudinal gages at 0 degree, i.e., gages 15-19, were monitored. In the fourth test, the

remote gage and the transverse gages at 0 degree , i.e., gages 20-25, were monitored. In a fifth test, the remote gage and the rosette were monitored. In all tests, the Daytronics was balanced at a zero load. The load was manually increased to 400 lbs and the Daytronics cycled, to record the data from each channel.

Elastic Results

The results are shown in Figure 2.11 for the longitudinal and transverse strains. The strains are plotted versus the radial distance. The solid lines represent the finite element results. Considering the low strains and the scale of the plot, the comparison is reasonably good. Note that in Figure 2.11, the longitudinal strain at 0 degree is small compared to that at 90 degrees, while both transverse strains are relatively small.

Elastic-Plastic Analysis

It was decided to run the elastic-plastic analysis with gages 8-14 and 26 hooked up to the Daytronics and gages 1-7 and the rosette (27, 28, and 29) hooked up to the Vishay/Ellis. During the test, the Daytronics continually cycled, except when the Vishay readings were taken. The Vishay was cycled at several points during the test. In the first phase of the test, the MTS ramp loaded the specimen, in load control, at a rate of 1 lb/sec. The ramp was paused at 400 lbs to cycle the Vishay. This was done to verify the preliminary analysis. The ramp was started again up to a load at 1000 lbs and paused to cycle the Vishay. The ramp was started in the unloading mode and the load decreased to 0 lb at the same rate. The Vishay was again cycled. In the second phase, the ramp was initiated at 0 lb and continued to

1400 lbs at the same rate. The Vishay was then cycled. The ramp was then started in the unloading mode and the load decreased back to 0 lb . A Vishay reading was taken. In the third phase, the ramp was initiated at 0 lbs and continued to 1800 lbs at the previous rate. The Vishay was then cycled. The ramp then unloaded the specimen to 0 lb , at which time another Vishay reading was taken. In the fourth phase, the ramp was initiated at 0 lb and continued to 2200 lbs at a rate of 2.3 lbs/sec. A Vishay reading was then taken. The ramp loading continued to 2500 lbs and paused to cycle the Vishay. The ramp was started in the unloading mode and continued to 0 lb . A final Vishay reading was then taken.

Elastic-Plastic Results

The longitudinal strains were computed and a three point average used for smoothing as well as thinning. The strains for gage 8, the closest to the hole, are plotted in Figure 2.12. Note that there are minimal residual strains after the first cycle with more and more after the following cycles. The strains for the remaining gages, 9-14 and 26, are also plotted in Figure 2.12. The solid lines in Figure 2.12 represent the finite element modelling [6]. Note that the amount of residual strain decreases as the distance from the hole increases, with virtually no residual strains recorded by gages 14 and 26. To get a better idea of how these strains vary with distance from the hole, plots of the strain versus the radial distance from the hole at a given load were generated. Figure 2.13 shows the strains in gages 8-14 at the points where Vishay readings were taken. The residual longitudinal strains are similarly shown in Figure 2.13. The solid

lines in Figure 2.13 represent the finite element modelling [6].

The transverse strains from the Vishay were similarly plotted. Figure 2.14 shows the strains in gages 2-7. The finite element analysis is also shown as the solid line.

The rosette data was reduced according to the formulas [16]:

$$\begin{aligned}e_x &= \frac{1}{3} [2(e_{27} + e_{29}) - e_{28}] \\e_y &= e_{28} \\e_{xy} &= \frac{1}{\sqrt{3}} [e_{29} - e_{27}]\end{aligned}\tag{2.10}$$

where

e_x = transverse strain

e_y = longitudinal strain

e_{xy} = shear strain

$e_{27,28,29}$ = strain from gages 27,28, and 29.

The components of strain in the loaded states are plotted in Figure 2.15. The residual strains are also plotted in Figure 2.15. The load indicated on the x-axis is the previous loading state. The finite element results [6] are drawn as solid lines.

SPECIMEN WITH A TRANSVERSE CRACK

The transversely cracked specimen data reported by Kenaga [1] was reviewed in light of the above observations on the constraint effect and the multi-axial stress state.

The schematic of the specimen is shown in Figure 2.16. Again, strip gages were used to zoom in on the strains at the crack tip. The crack was grown to a length of 0.311 inch at a maximum cyclic stress of 9.4 ksi. At this point, a 1.5 overload with a maximum stress of 14.1 ksi was applied. Note that prior to the overload, the Daytronics was zeroed. During the overload, the strains were recorded. The strains at gages 1-10 and the remote gage are shown in Figure 2.17. Note that gage 1 failed during the test.

The finite element analysis [6] is also shown for comparison. Whereas the finite element analysis of the hole modelled the unyielded material from the start of the test, the finite element analysis of the transverse crack did not. In this case, the finite element analysis started at one cycle prior to the overload.

The data indicates that the cycling tends to soften the material.

SPECIMEN WITH AN OBLIQUE CRACK

The specimen with the oblique crack reported by Kenaga [1] was also reviewed.

The schematic for this specimen is shown in Figure 2.18. The crack was grown to a length of 0.397 inch at a maximum cyclic stress of 6.66 ksi. A 1.5 overload with a maximum stress of 10 ksi was applied. The Daytronics was zeroed prior to the overload. During the overload, the strains were recorded. The strains at gages 1-10 and the remote gage are shown in Figure 2.19.

The finite element analysis [6] is also shown for comparison. Since the finite element analysis was run the same way as for the transverse crack, the results are similar. Again, the experimental results indicate work-softening.

DISCUSSION

The use of uniaxial specimens in the characterization of Boron/Aluminum gives good elastic and plastic constants and work-hardening parameters for unconstrained plasticity. However, because of the constraint effect, the work hardening exponent had to be increased from 5.8 to 7.2 to model the tapered specimen. The elastic and remaining plastic properties, however, remain unchanged. The multi-axial stress state was modelled well for the circular hole experiment. In the case of the transverse and oblique crack, the essence of the strain histories during an overload was captured by the finite element modelling. However, because the analysis did not contain a damage accumulation parameter, the results are not as good as for the hole.

Table 2.1 A summary of the mechanical properties of B/A1

Fiber Angle (Deg)	Elastic Modulus (msi)	Elastic Poissons's Ratio	Plastic Poisson's Ratio	Ultimate Stress (ksi)	Yield Stress (ksi)
0	27.05	0.232	0.577	202.1	none
10	31.54	0.213	0.881	70.4	36.1
20	26.96	0.278	0.750	51.6	19.7
30	20.86	0.287	0.685	34.2	12.1
45	15.99	0.260	0.654	25.2	12.7
60	19.18	0.164	0.400	17.6	9.0
90	18.22	0.157	0.002	22.2	10.9

Table 2.2 Strain gage positions for the specimen with a centered circular hole.

Gage Number	Gage Type	Gage Factor	X Position (inches)	Y Position (inches)
1	EA-13-031MH-120	2.12	0.436	0.000
2	EA-13-031MH-120	2.12	0.492	0.000
3	EA-13-031MH-120	2.12	0.593	0.000
4	EA-13-031MH-120	2.12	0.653	0.000
5	EA-13-031MH-120	2.12	0.753	0.000
6	WA-13-030WT-120	2.08	1.072	0.000
7	WA-13-030WT-120	2.08	1.375	0.000
8	EA-13-031MH-120	2.12	0.424	0.000
9	EA-13-031MH-120	2.12	0.503	0.000
10	EA-13-031MH-120	2.12	0.587	0.000
11	EA-13-031MH-120	2.12	0.661	0.000
12	EA-13-031MH-120	2.12	0.746	0.000
13	WA-13-030WT-120	2.08	1.072	0.000
14	WA-13-030WT-120	2.08	1.375	0.000
15	EA-13-031MH-120	2.12	0.000	0.444
16	EA-13-031MH-120	2.12	0.000	0.494
17	EA-13-031MH-120	2.12	0.000	0.604
18	EA-13-031MH-120	2.12	0.000	0.652
19	EA-13-031MH-120	2.12	0.000	0.762
20	WA-13-030WT-120	2.08	0.000	1.882
21	EA-13-031MH-120	2.12	0.000	0.424
22	EA-13-031MH-120	2.12	0.000	0.509
23	EA-13-031MH-120	2.12	0.000	0.584
24	EA-13-031MH-120	2.12	0.000	0.669
25	EA-13-031MH-120	2.12	0.000	0.743
26	WA-13-030WT-120	2.08	0.000	1.882
27	EA-13-125YA-120	2.05	-0.831	-0.480
28	EA-13-125YA-120	2.05		
29	EA-13-125YA-120	2.05		

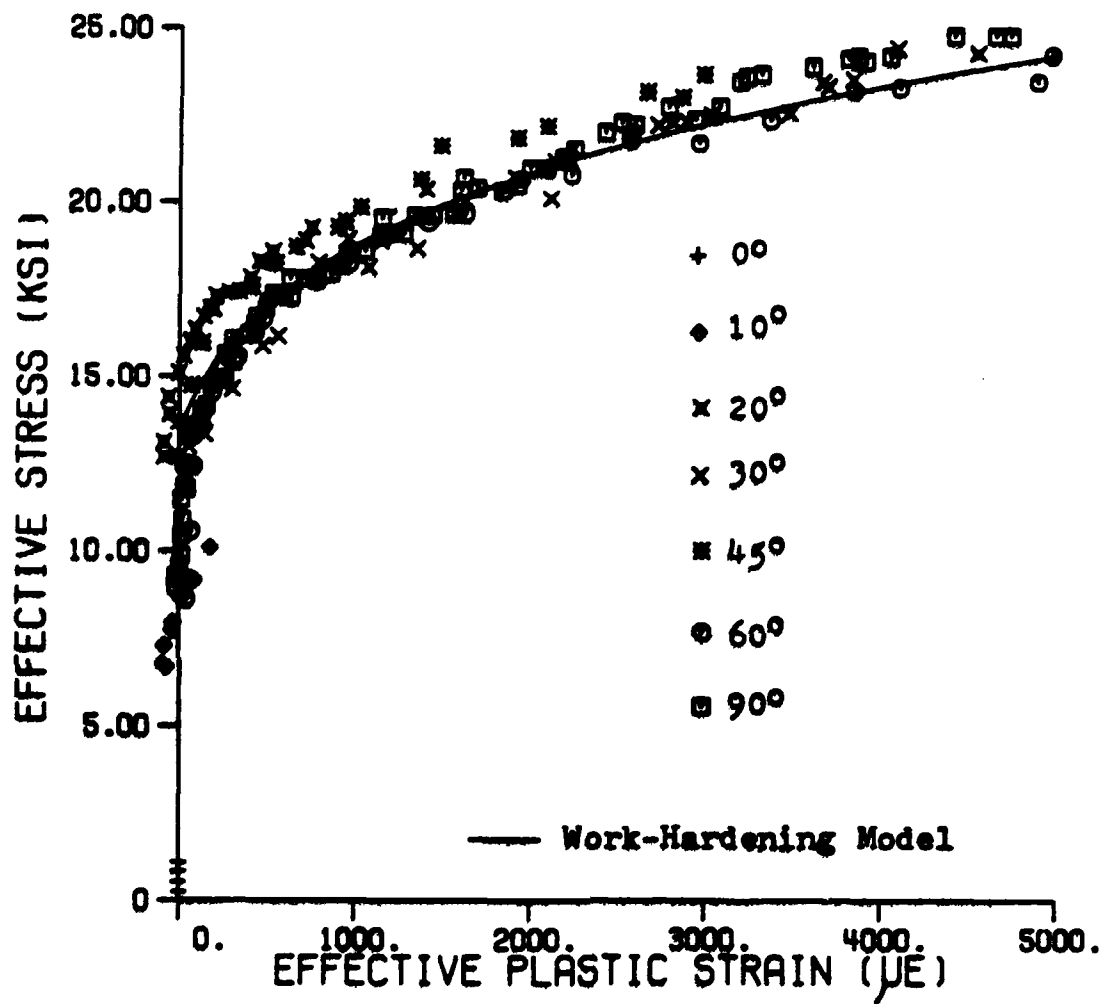


Figure 2.1 Effective stress versus effective plastic strain.

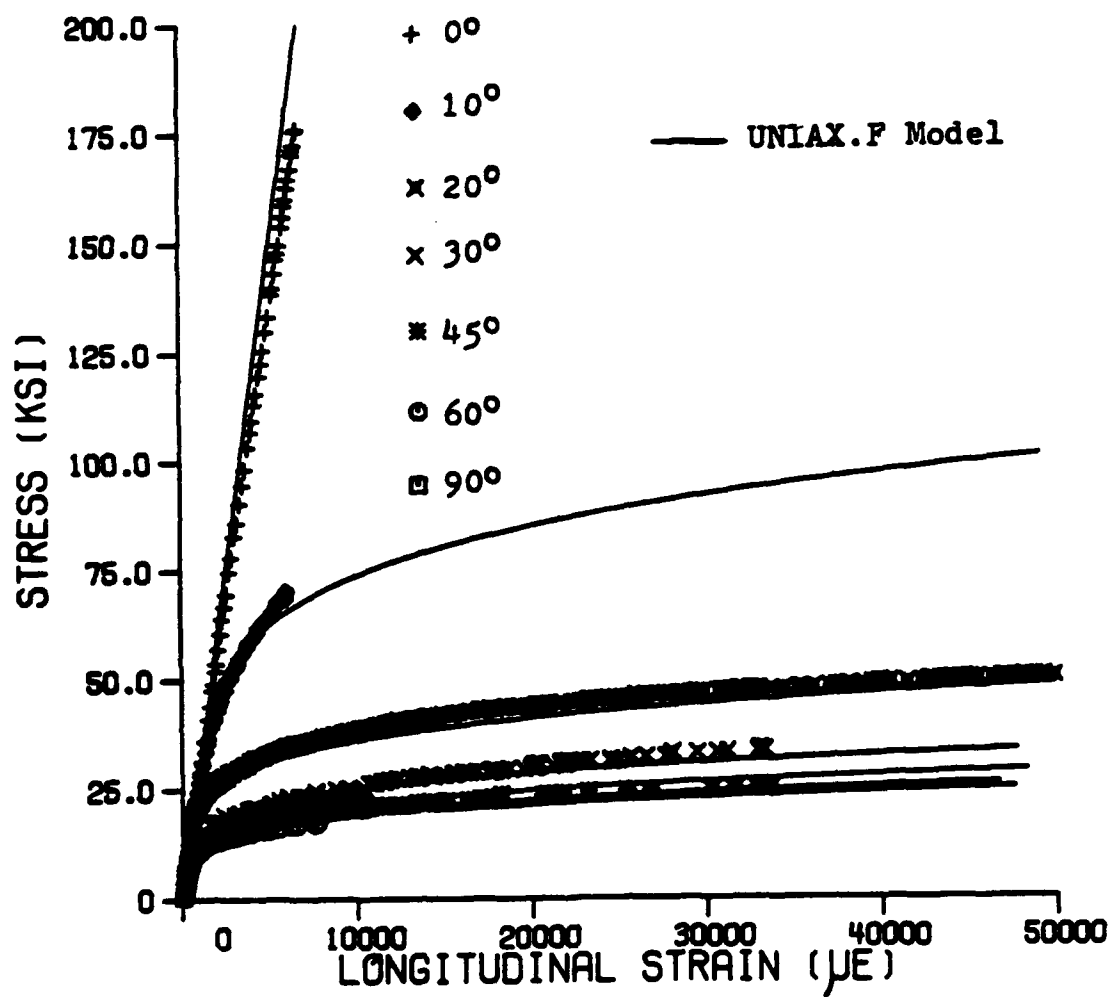


Figure 2.2 Stress versus longitudinal strain for various fiber orientations.

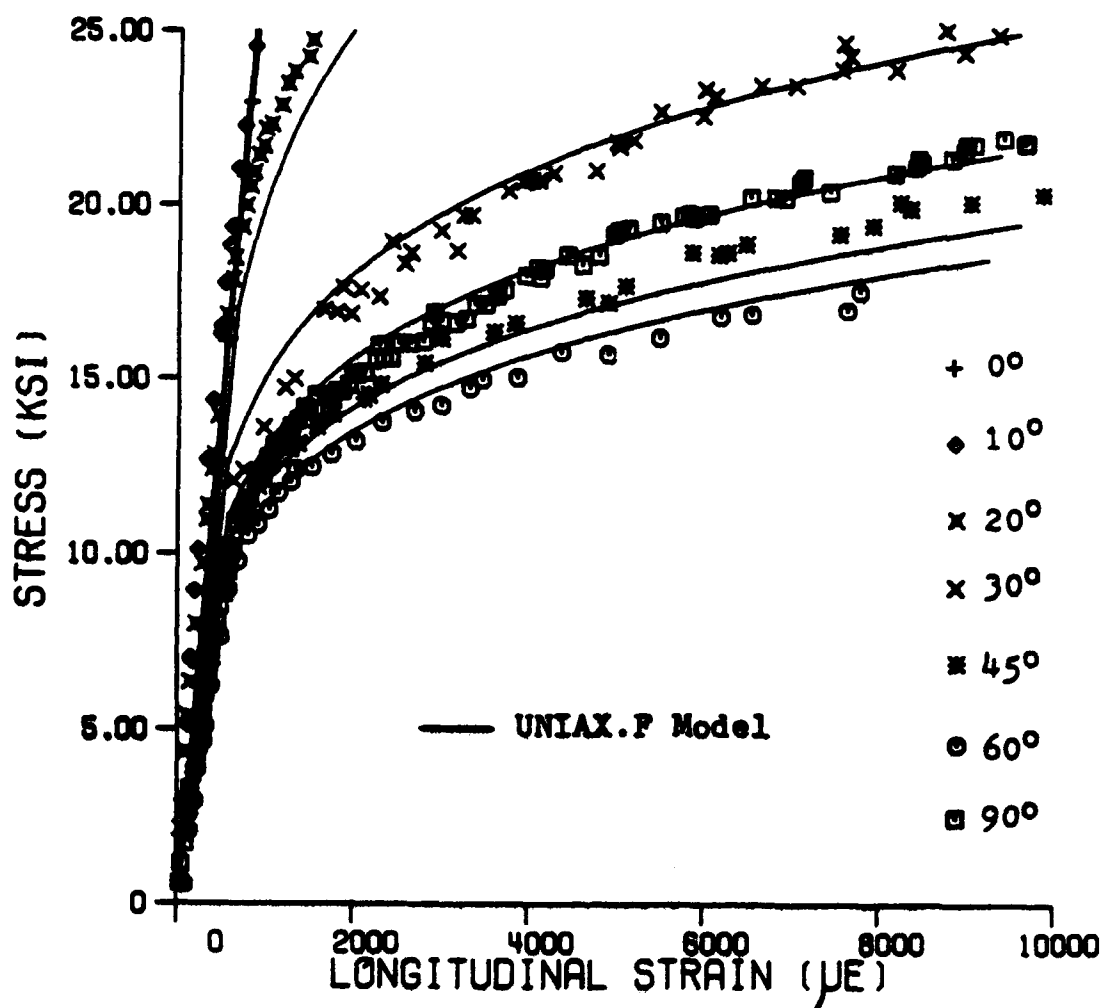


Figure 2.3 Stress versus longitudinal strain for various fiber orientations shown on a reduced scale .

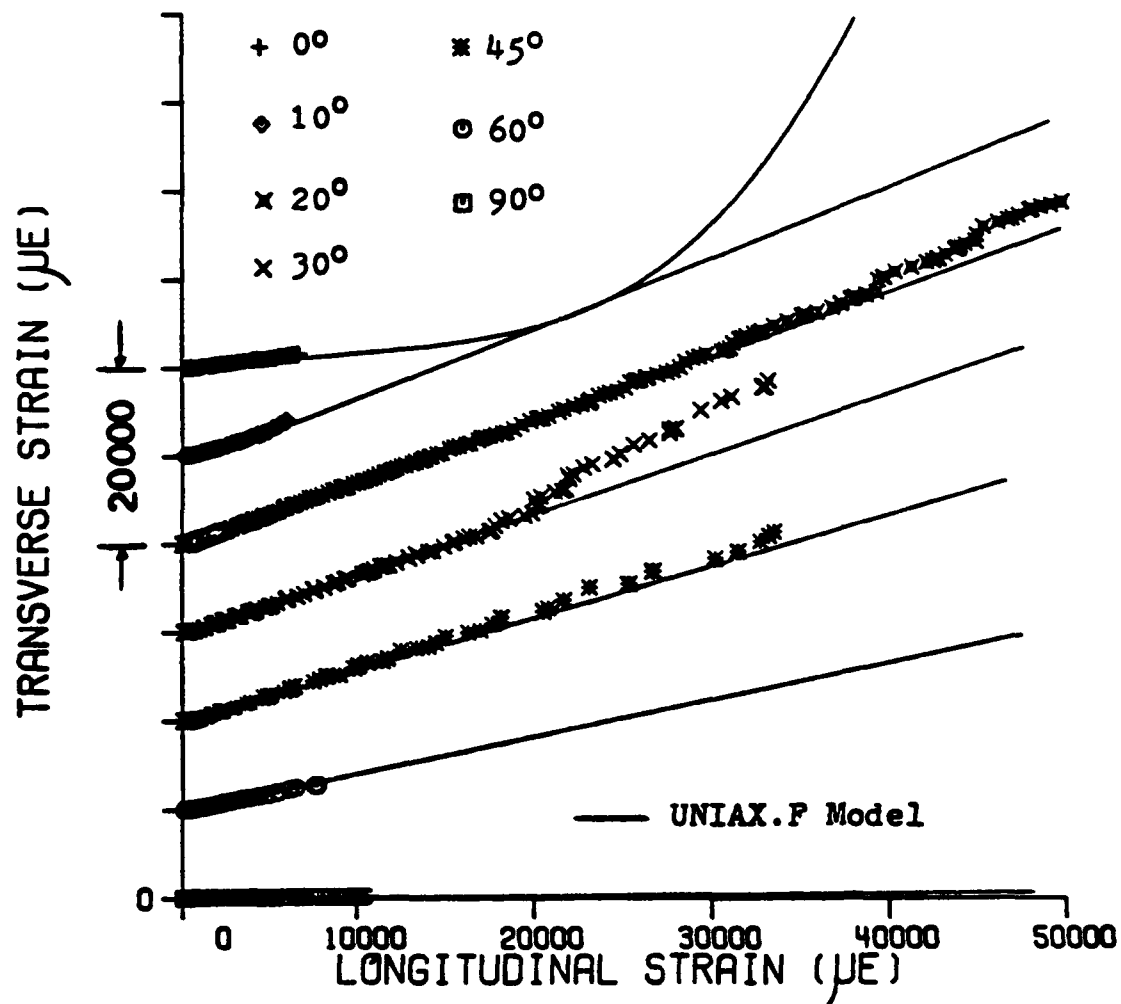


Figure 2.4 Transverse versus longitudinal strain for various fiber orientations. The different orientations are vertically displaced for clarity.

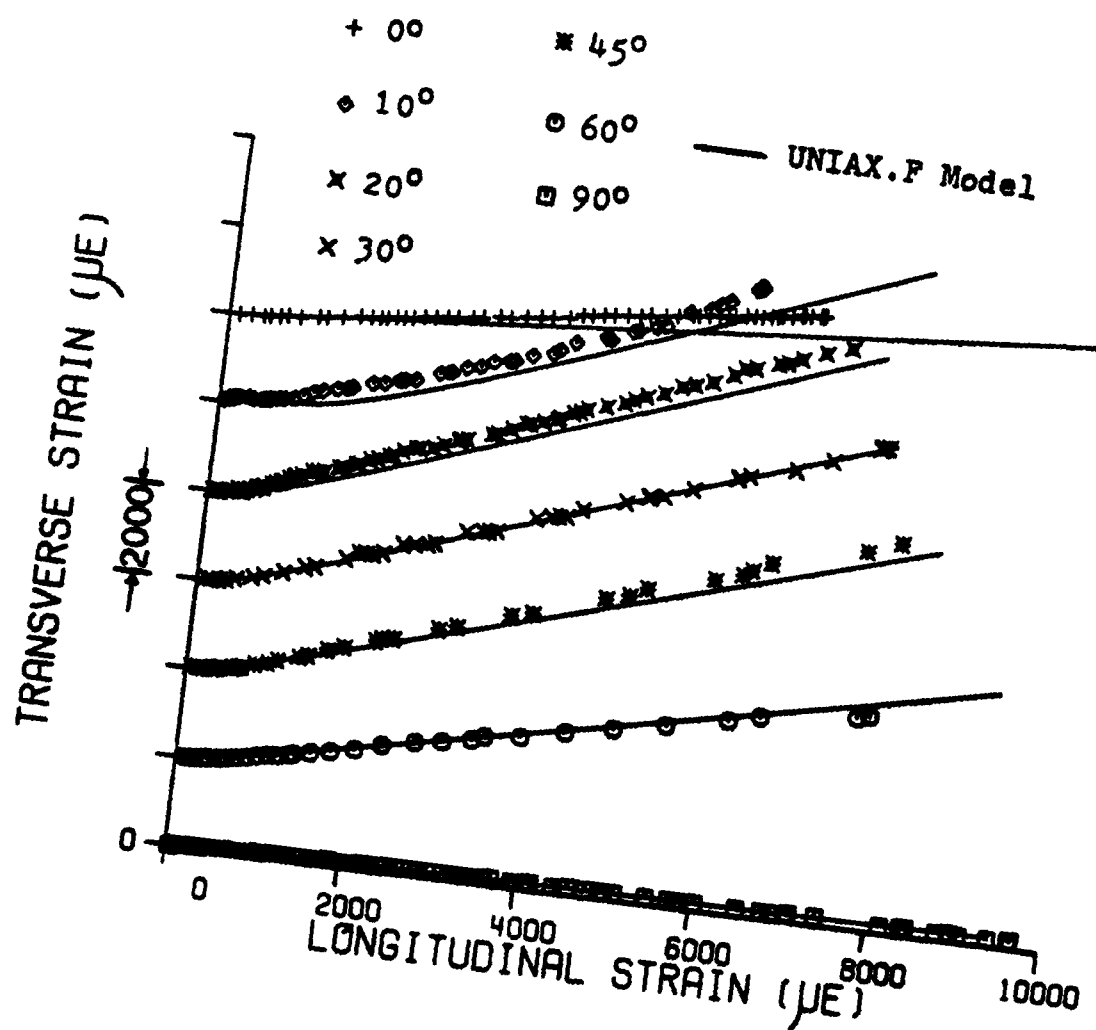


Figure 2.5 Transverse versus longitudinal strain for various fiber orientations shown on a reduced scale. The different orientations are vertically displaced for clarity.

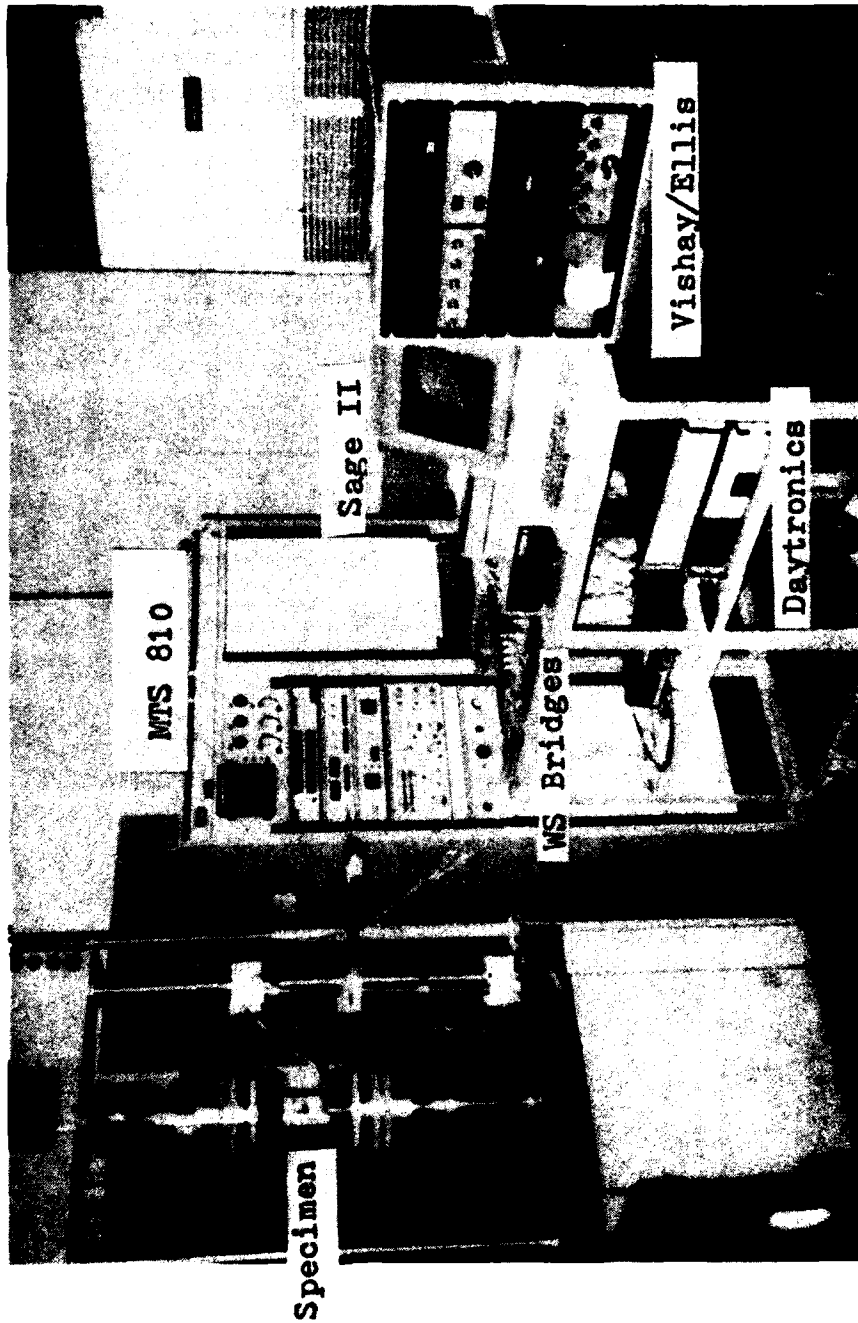


Figure 2.6 Photograph of the experimental setup used for the material characterization .

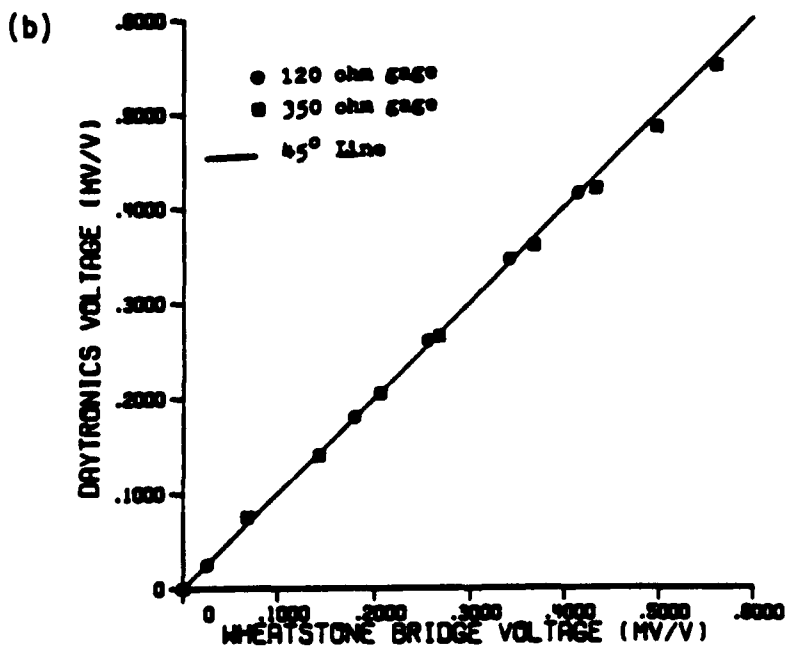
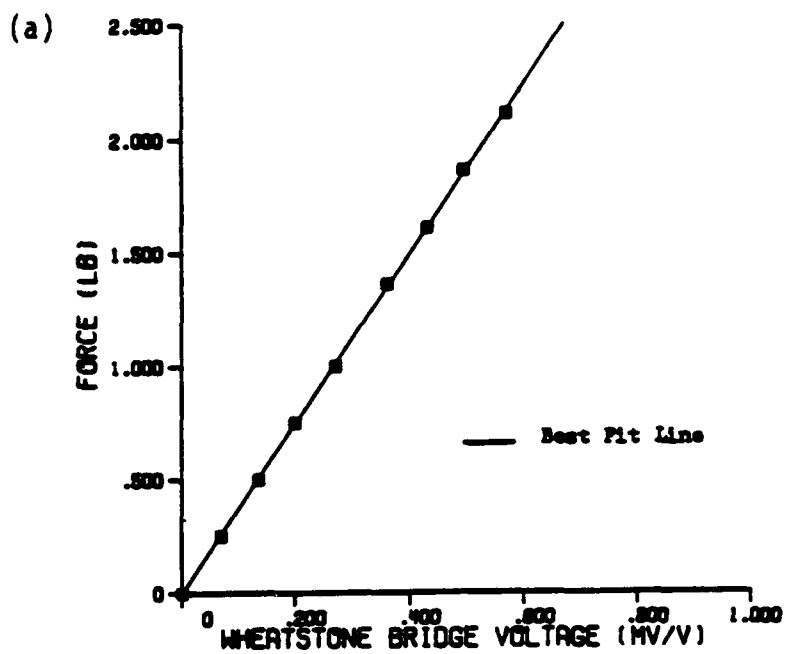


Figure 2.7 Calibration of Daytronics Data Acquisition System using a cantilever beam. (a) Applied force versus the Wheatstone bridge voltage. (b) Daytronics output versus Wheatstone bridge voltage.

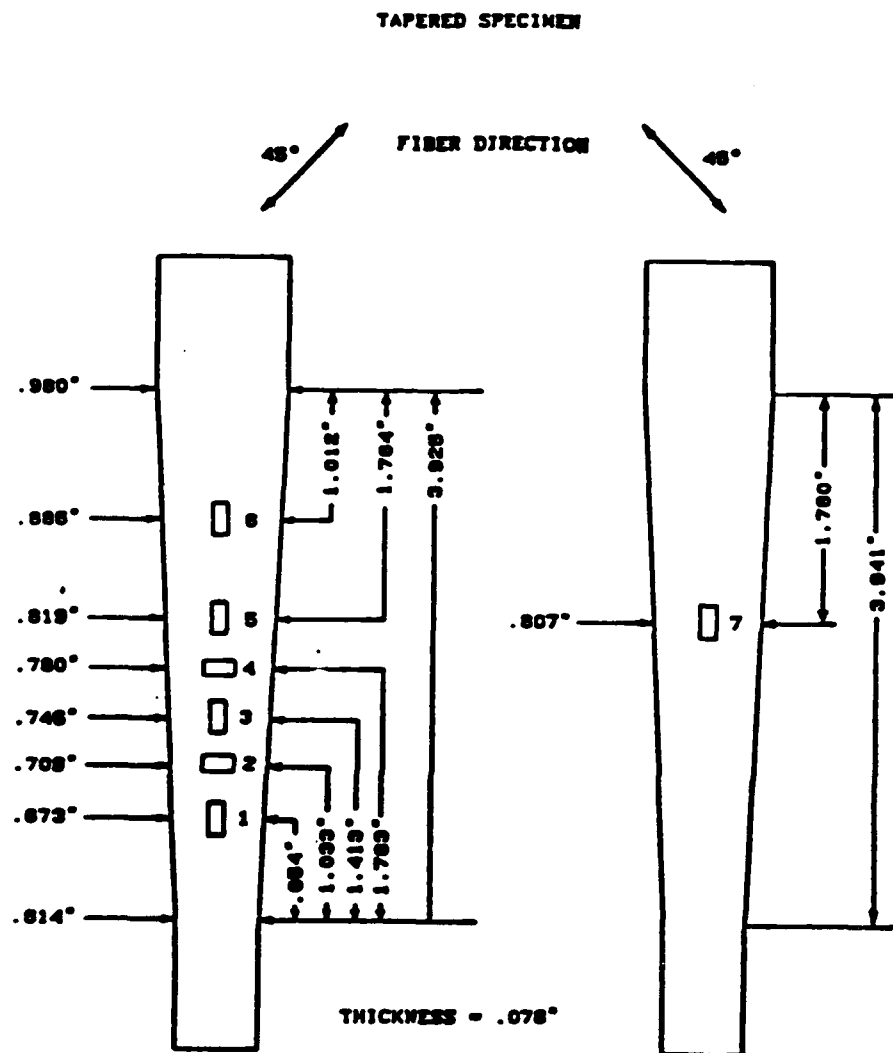


Figure 2.8 Schematic of the tapered specimen, B25.

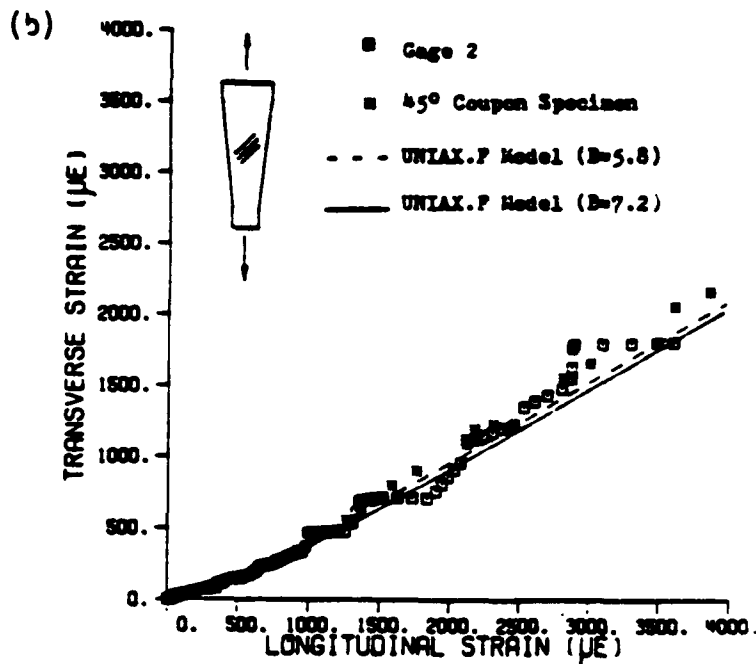
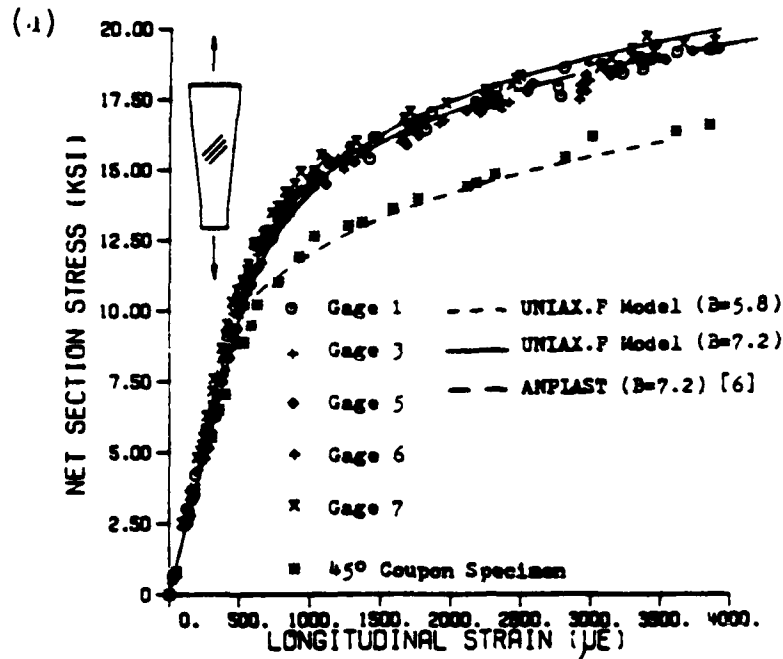


Figure 29 Stress-strain and strain-strain relationships for the tapered specimen.
 (a) Net section stress versus longitudinal strain.
 (b) Transverse versus longitudinal strain. The data for the 45 degree coupon specimen is included for comparison.

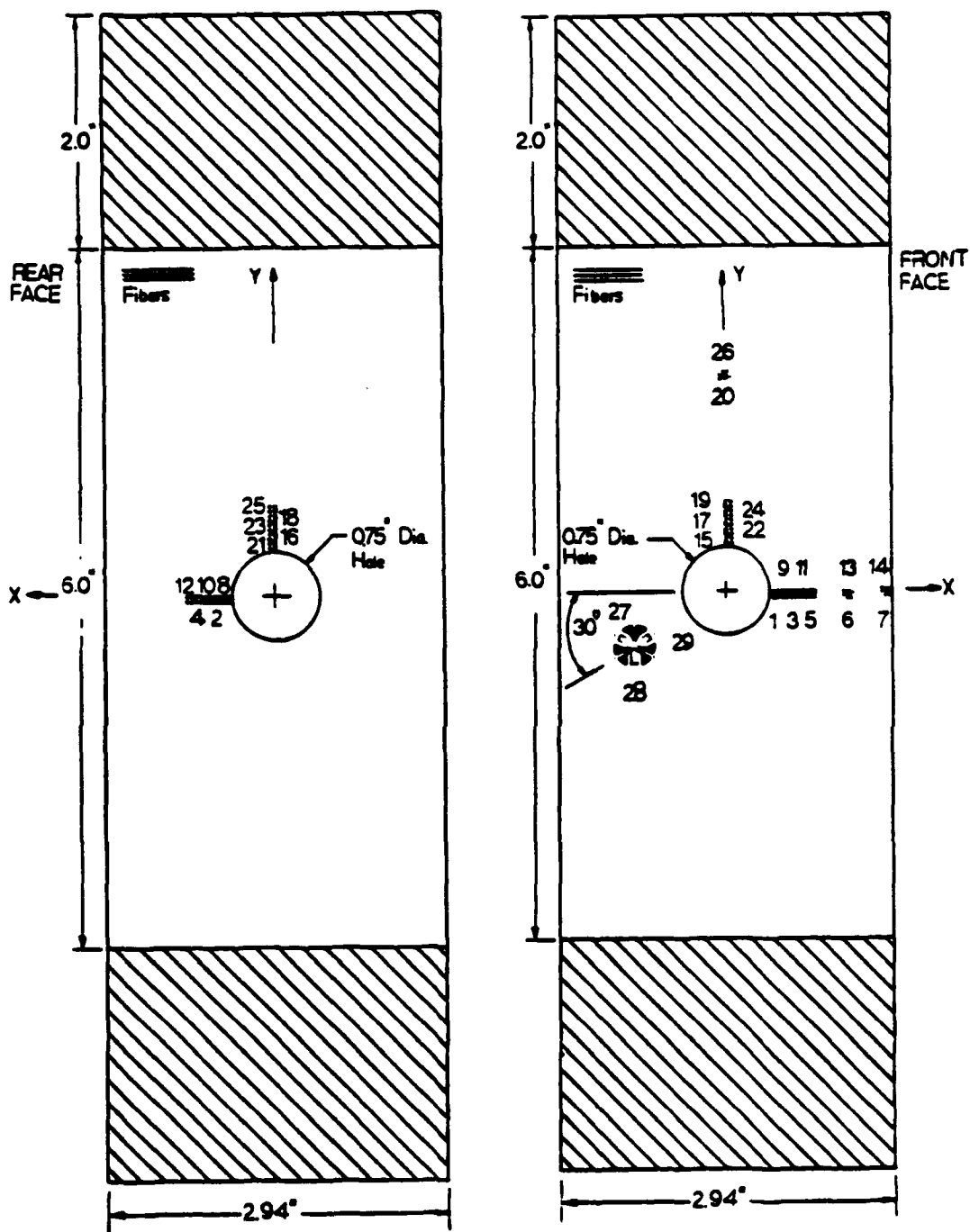


Figure 2.10 Schematic of the specimen with a circular hole, D4.

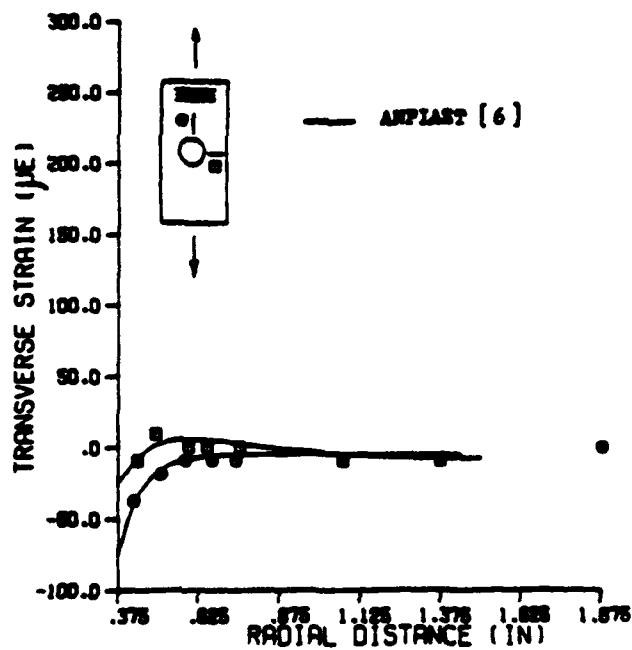
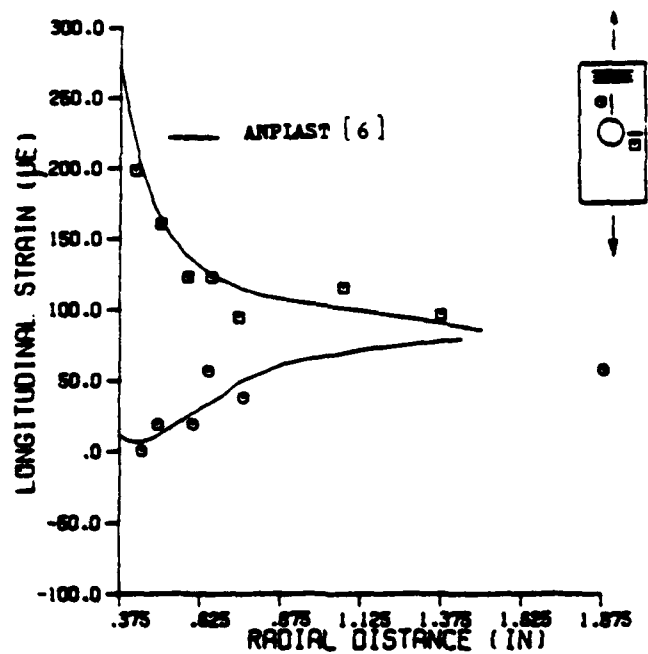


Figure 2.11 Longitudinal and transverse strain variation with distance from the edge of the hole. The remote load is 400 lb.

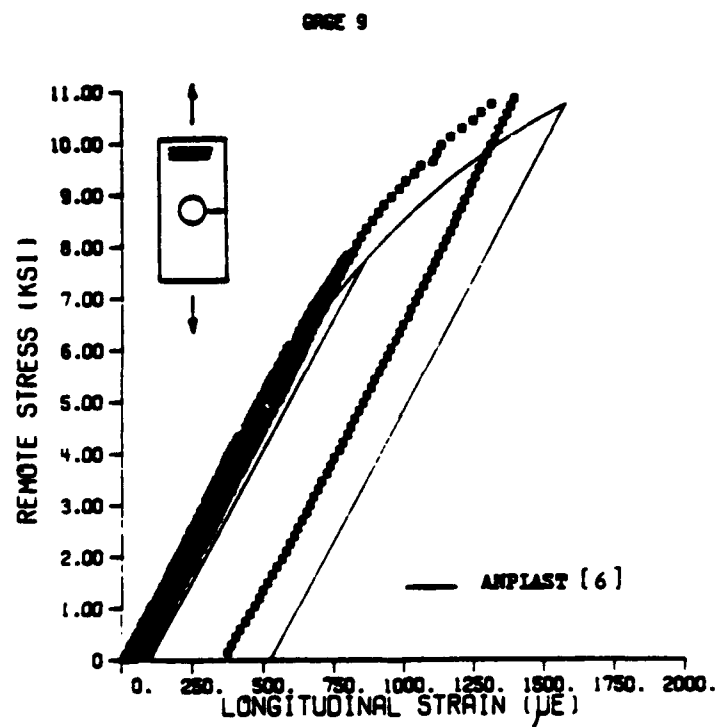
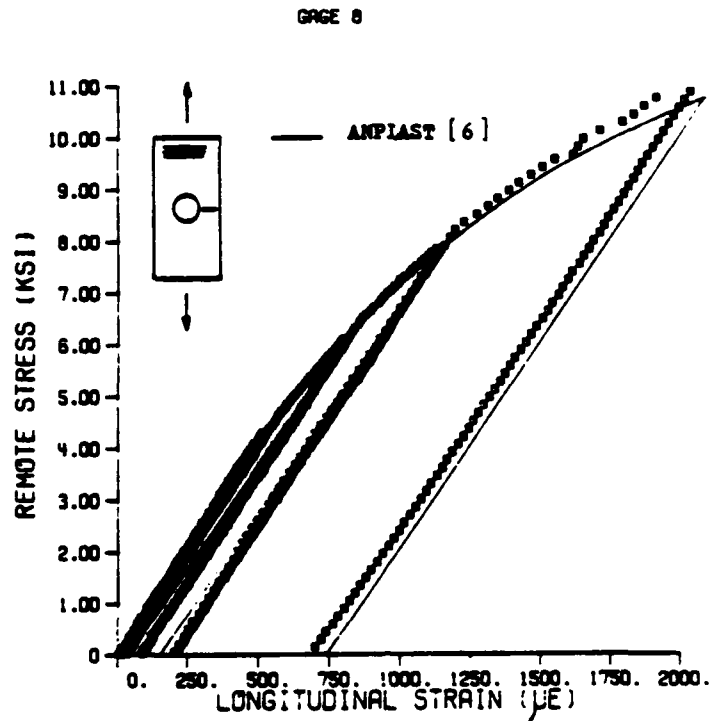


Figure 2.12 Strain history from gages along a line 90 degrees to the loading. Notice the high residual strains near the edge of the hole .

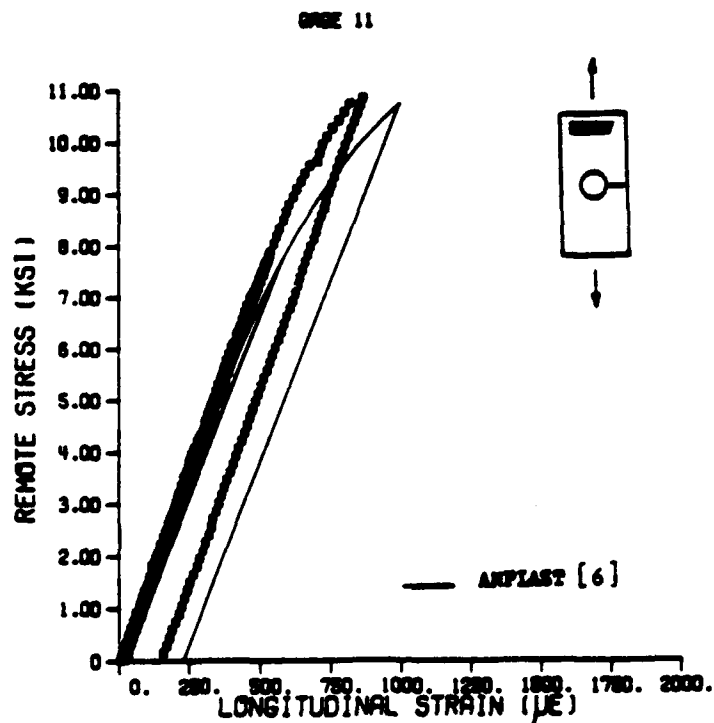
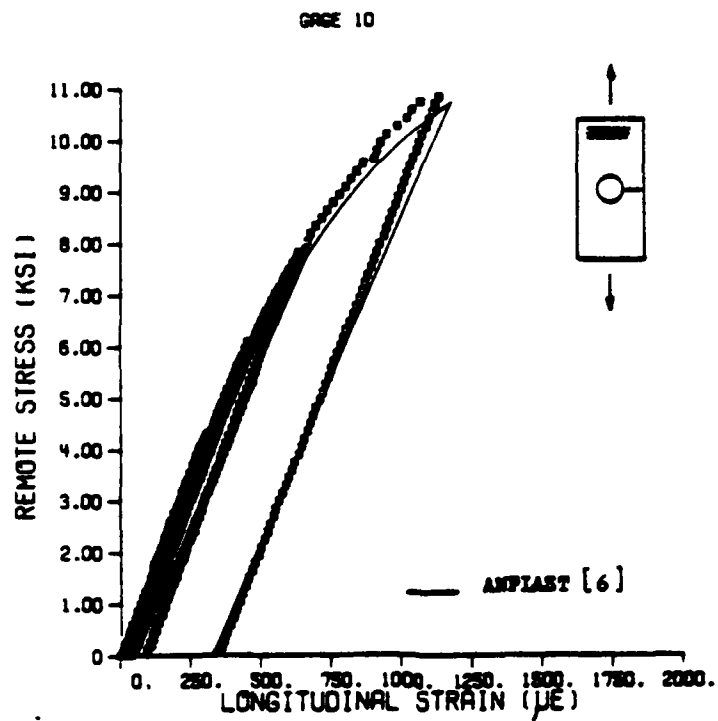


Figure 2.12 continued

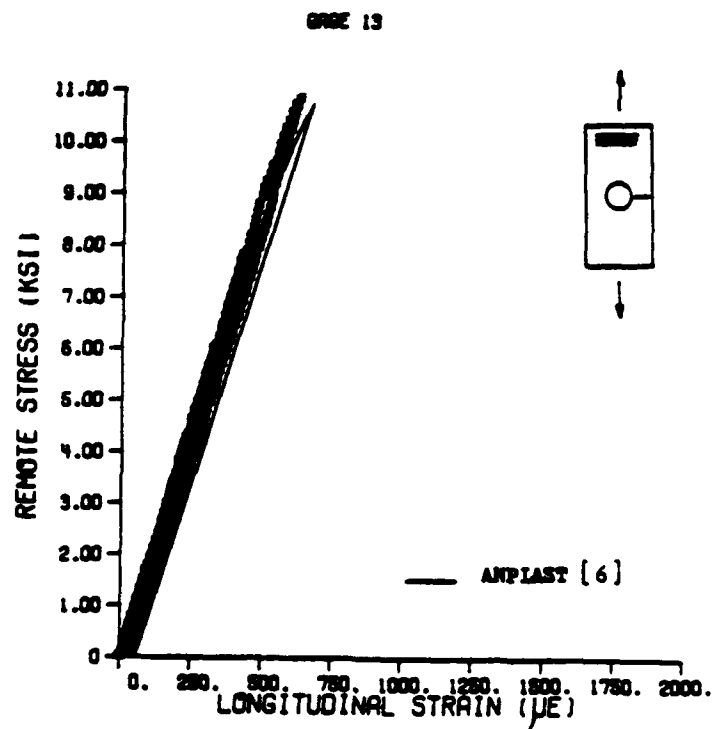
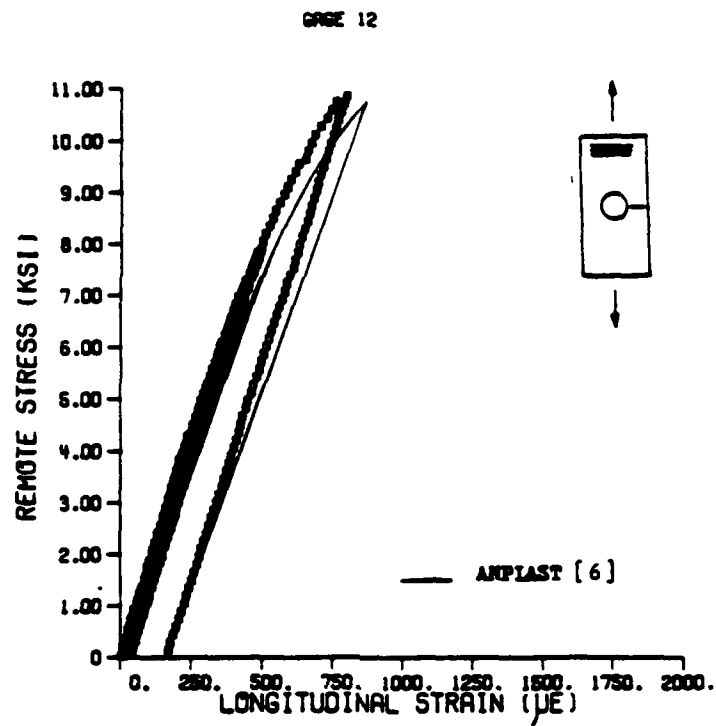
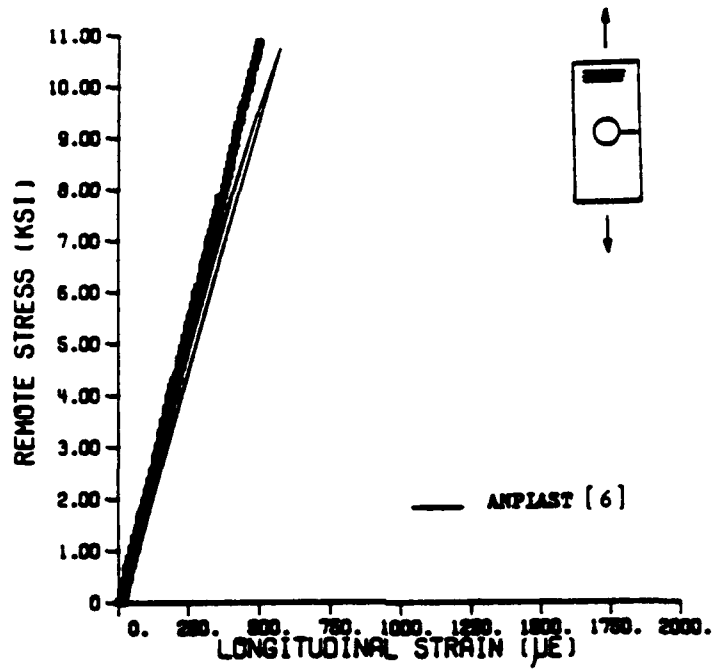


Figure 2.12 continued

GAGE 14



REMOTE GAGE

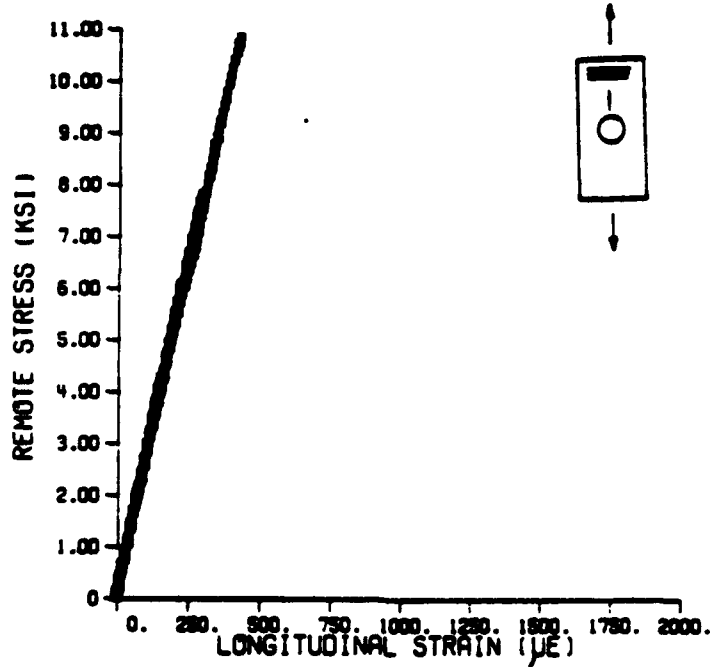


Figure 2.12 continued

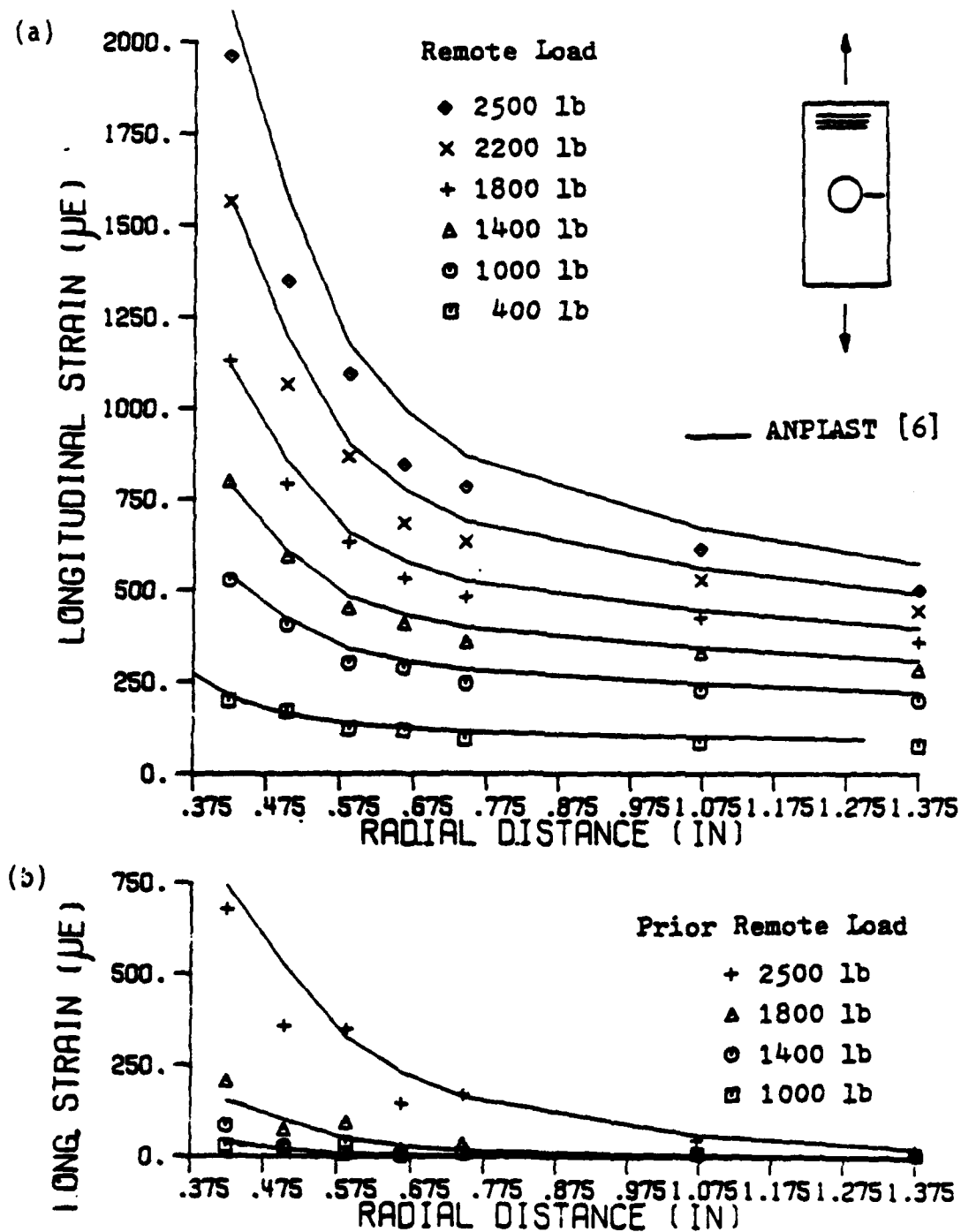


Figure 2.13 Longitudinal strain variation along a line 90 degrees to the loading. (a) Loaded State, (b) Residuals from prior loading.

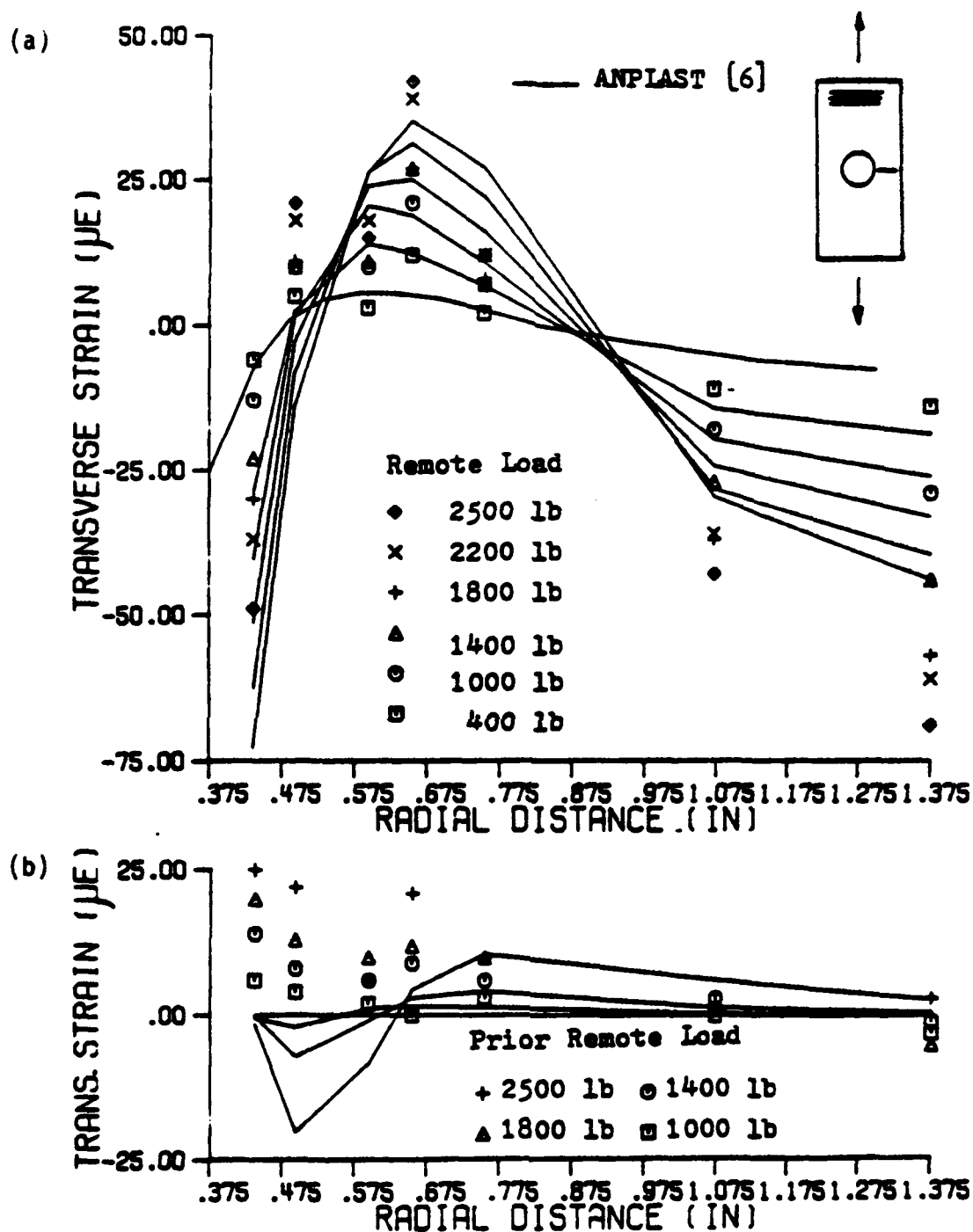


Figure 2.14 Transverse strain variation along a line 90 degrees to the loading. (a) Loaded State, (b) Residuals from prior loading.

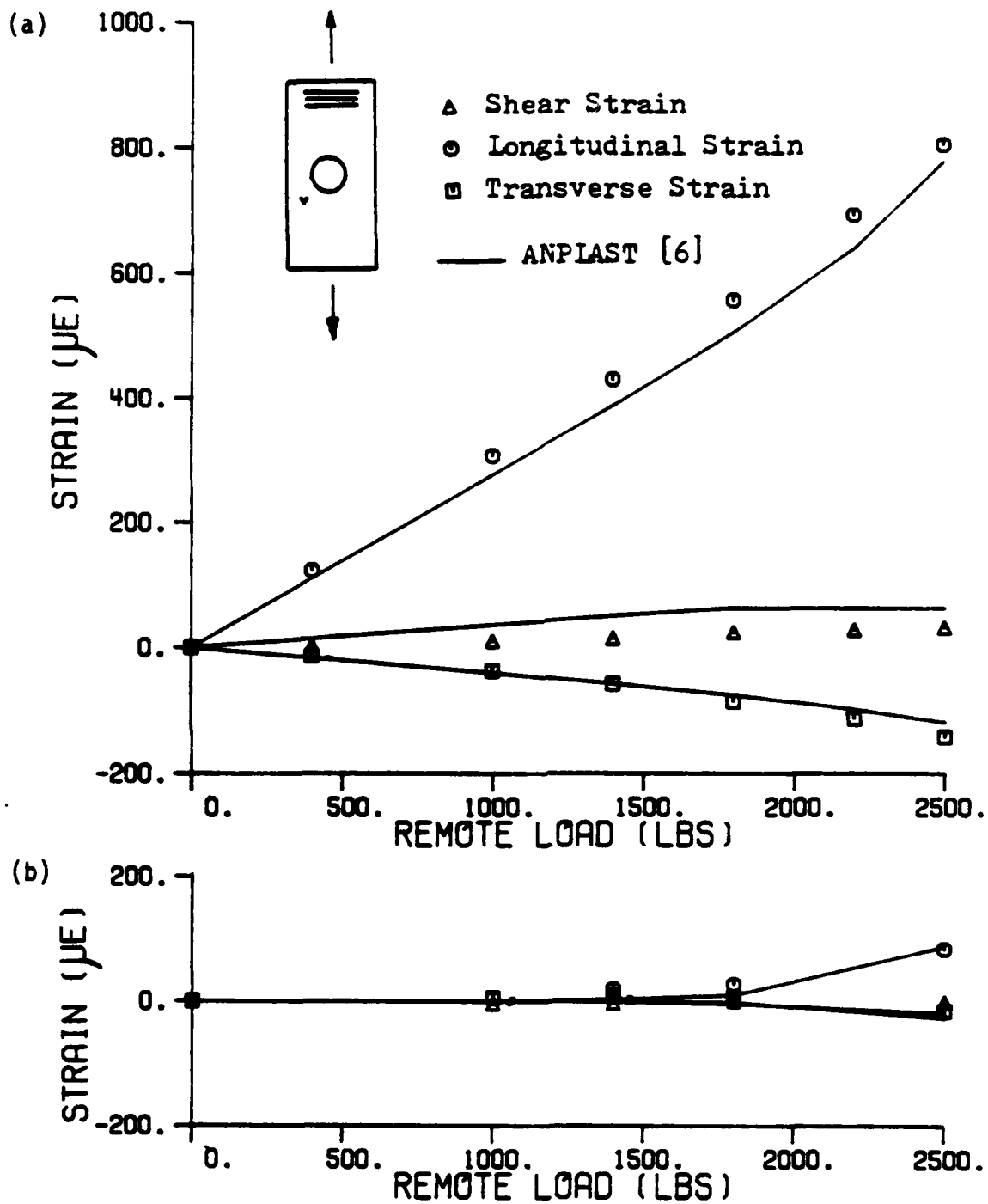


Figure 2.15 Longitudinal, transverse, and shear strain components at the delta rosette in the (a) Loaded State and (b) Residuals from prior loading.

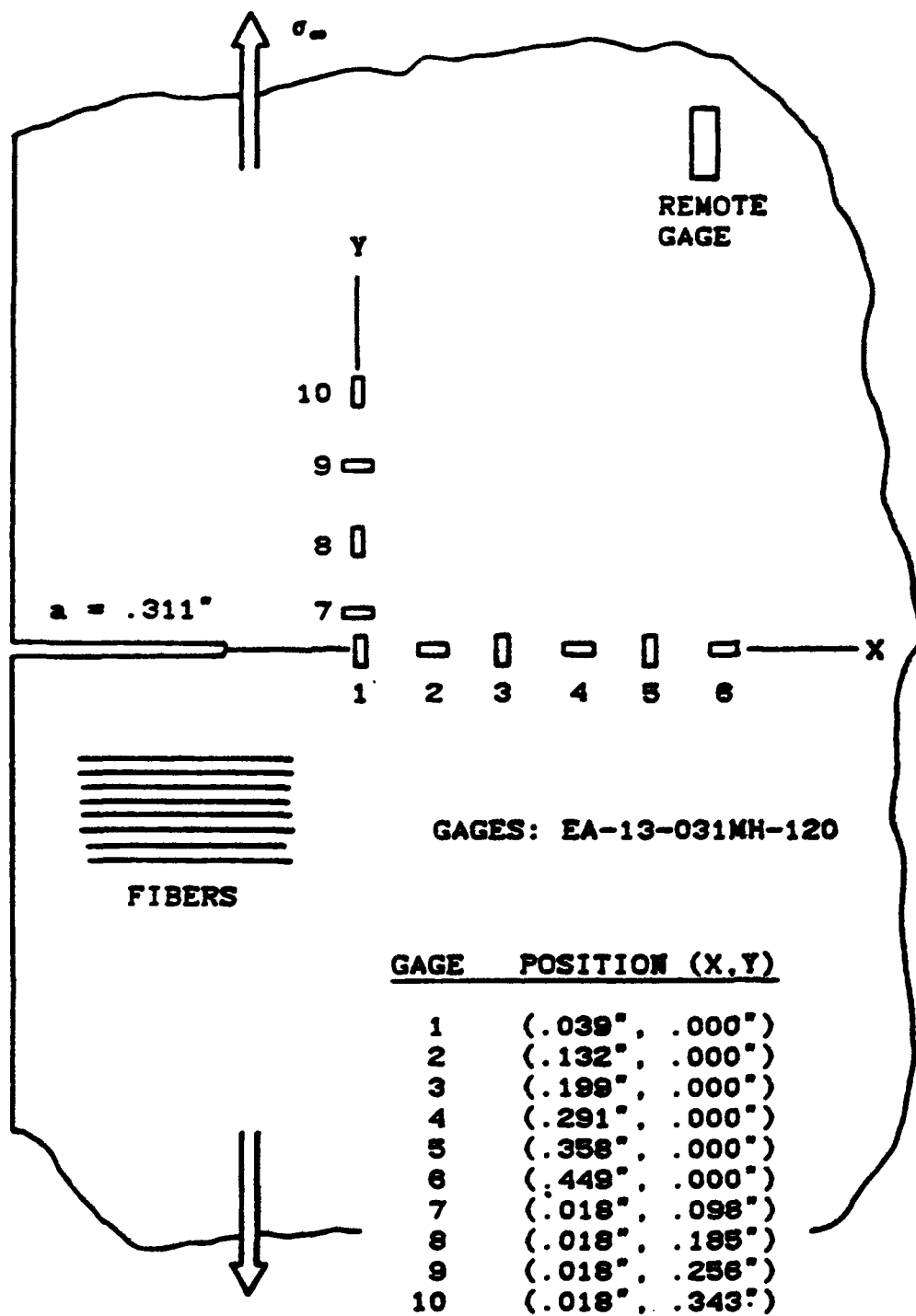


Figure 2.16 Schematic for the specimen with a transverse crack, B26 .

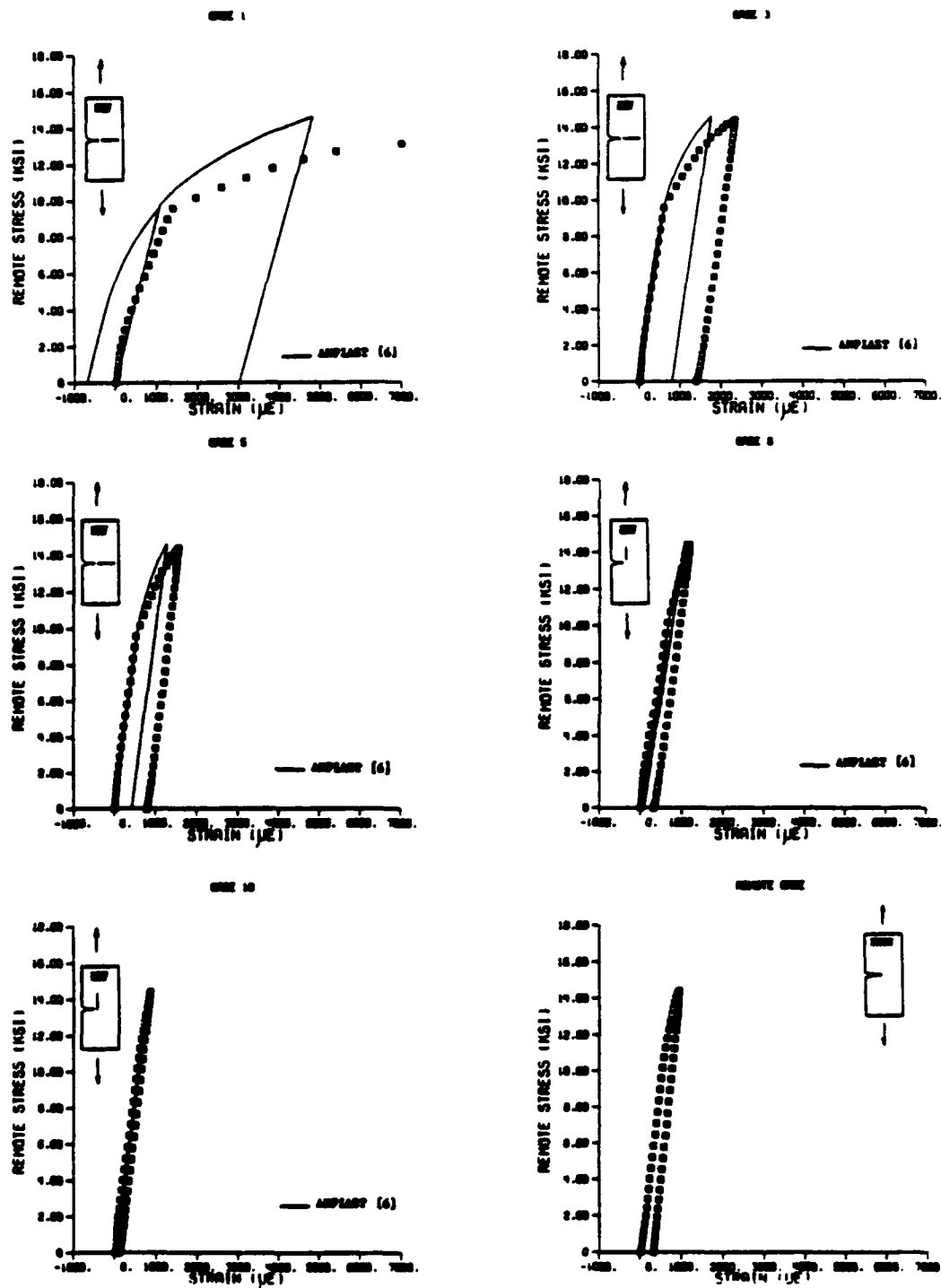


Figure 2.17 Strain history at the gages of specimen B26 during a 1.5 overload. Notice that gage 1 failed during the test.

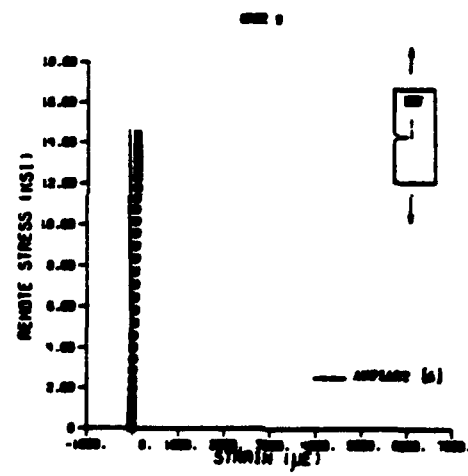
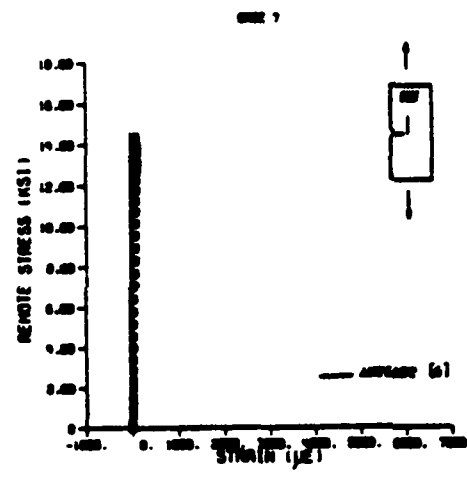
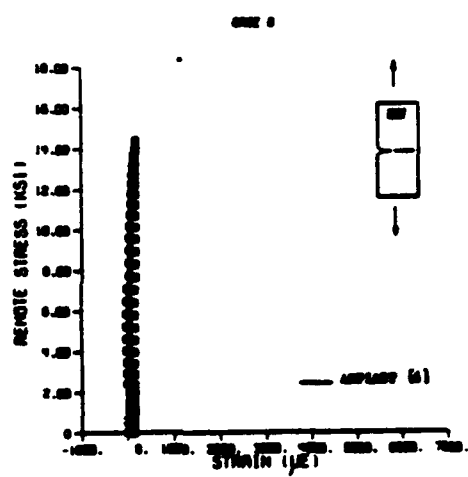
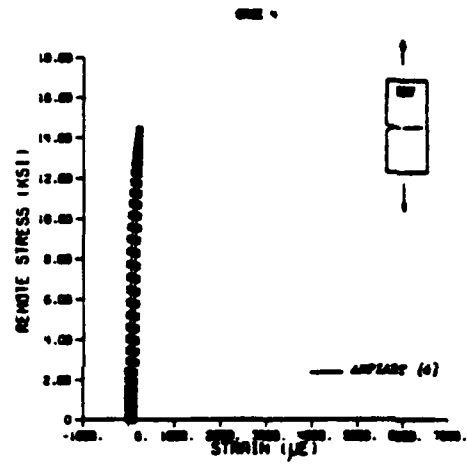
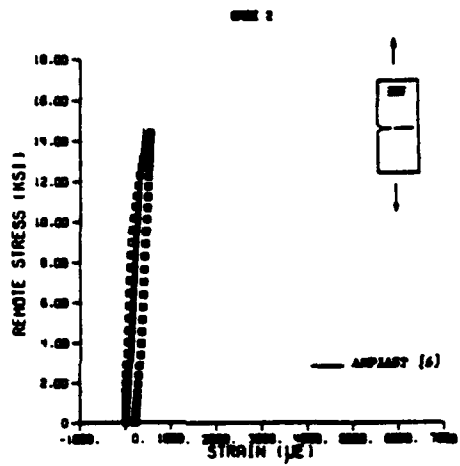


Figure 2.17 continued

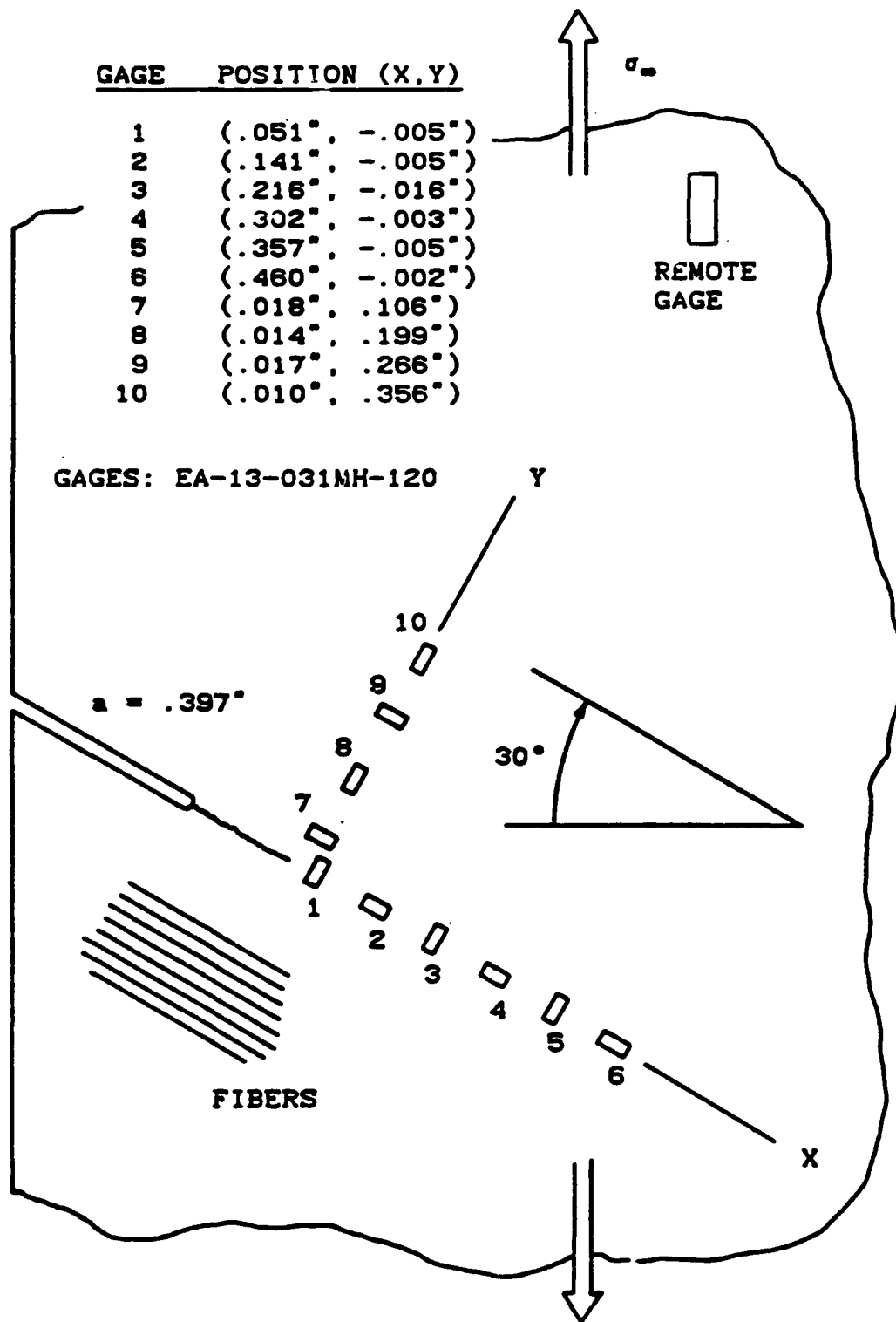


Figure 2.18 Schematic for the specimen with an oblique crack, B27 .

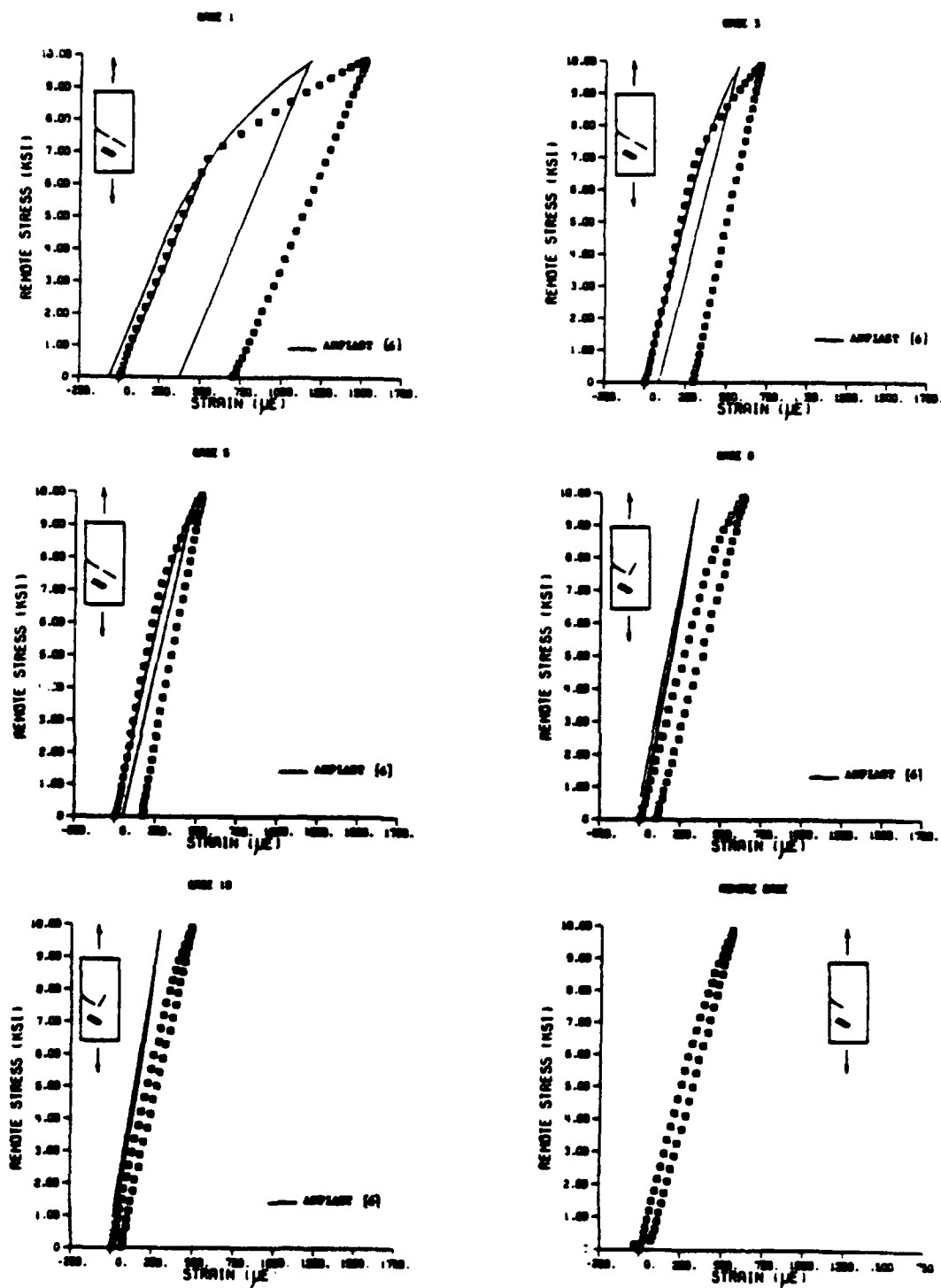


Figure 2.19 Strain history at the gages of specimen B27 during a 1.5 overload.

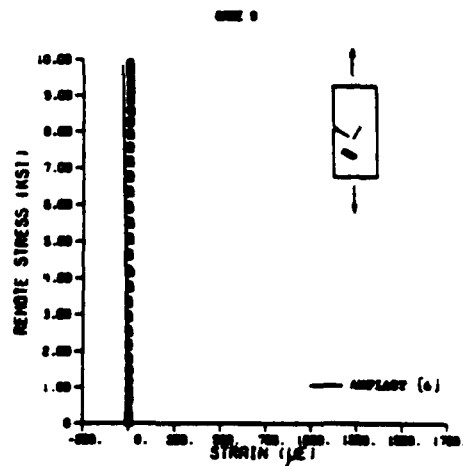
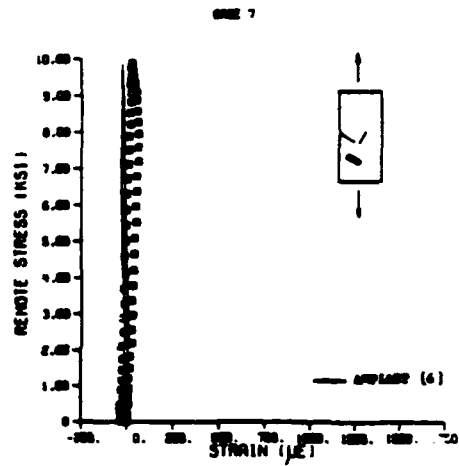
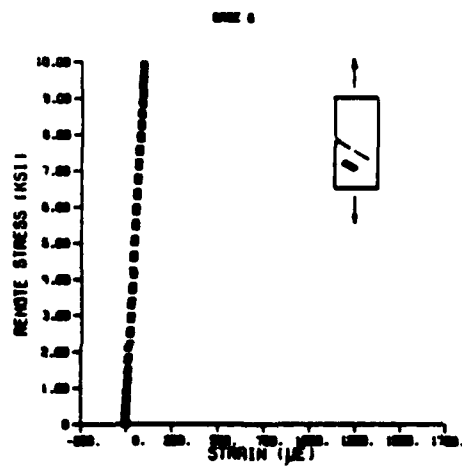
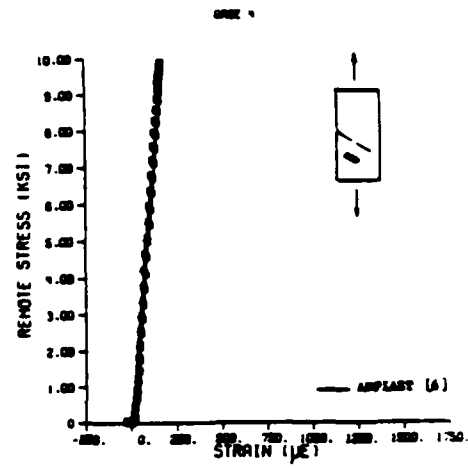
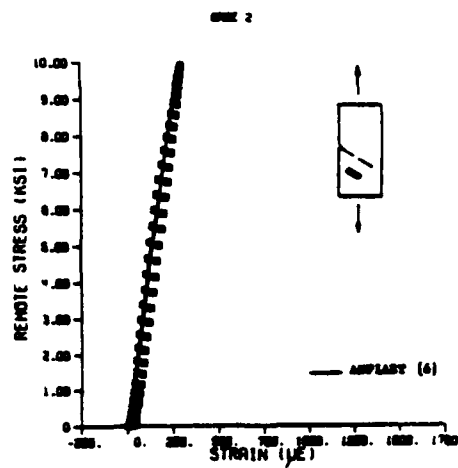


Figure 2.19 continued

SECTION 3 : BASELINE FATIGUE

A series of fatigue tests was performed on single edge cracked Boron/Aluminum specimens. Three fatigue specimen geometries were designed for fibers running 90, 45, and 15 degrees to the loading. All tests were conducted in an air environment at 10 Hz using a sinusoidal loading. Crack length versus cycles data were collected for each specimen.

FATIGUE SPECIMEN DESIGN

Specimens were cut using two methods. It was suggested in [1] that the specimens be cut using an electric discharge machine (EDM). Specimens C1, C2, and C3 were cut using the EDM. The plate was put in an oil bath to cool it during the cutting process. A brass electrode, 0.065" thick, was gradually lowered through the plate thickness to make the cut. This technique gave slightly beveled edges because the force of the electrode on the plate deflected it. It was also difficult to ensure that the orientation of fibers was as required since there was no convenient way to make small adjustments in the alignment of the plate when it was in the EDM. The rest of the specimens were cut using a milling machine. The table to which the plate was clamped automatically travelled at a rate of 2 inches per minute. A 6" x 0.040" circular diamond tip blade spinning at 1465 rpm was lowered approximately 0.010" between each pass. Water cooling was

used to preserve the blade and to reduce heating of the specimen. In both cutting methods, the orientation of the fibers was determined from an exposed fiber near the edge of the plate.

Notches were machined into specimens C1, C2, and C3 using the EDM by placing the specimens on edge and lowering an electrode into the edge. As the notch was cut, the electrode was gradually burned away, leaving a rounded notch. The notches in the other specimens were cut using the milling machine. The blade was manually fed into the edge of the specimen to the desired notch size. Again, the notch was partially rounded. To achieve a sharp notch root, the machined roots were tapped with a razor blade.

Aluminum tabs were affixed to the specimens to prevent the grips of the MTS machine from crushing them. The tabs were glued on with a 1:1 resin/hardener mix (by weight) of Thermoset Epoxy Resin 103 Variable Flex Adhesive to Thermoset Hardener 103 Variable Flex Adhesive. This gave a semi-rigid bond which was recommended by the manufacturer for this type of application. The glue was allowed to set up for 24 hours.

The specimens were sanded with 600 grit paper and polished on a buffing machine using Tripoli buffing compound.

The specimen cutting plans for plates A, B, C, and D are shown in Figures 3.1 and 3.2. A summary of the fatigue specimens manufactured is given in Tables 3.1 and 3.2. Figure 3.3 shows photographs of typical 90, 45, and 15 degree specimens. Specimens with the designation A are taken from Kenaga [1]. All other data is newly generated.

Design Criterion

The choice of notch size and loading was determined with the aid of Figure 3.4. A computer program called SIGMAA.F was written to calculate the remote stress at a given crack length for a constant value of the stress intensity factor using the relation:

$$\sigma = \frac{K}{\sqrt{\pi a}} \quad (3.1)$$

where:

$a \equiv$ crack length

$K \equiv$ stress intensity factor

Note that since there is no stress intensity factor solution for cracks in finite orthotropic sheets, one had to be obtained. This is done in Section 4.

For the present purposes, a numerical value was needed, so the infinite sheet solution, $K = \sqrt{\pi a}$, was used. The lower dashed line represents the lowest value of K at which the crack is known to grow for the various specimens. Hence, it is near a threshold level. The upper dashed line represents a value of K at which either fracture occurs or is imminent. Thus, it is near critical level.

Define the net section yield as the point when the material between the crack tip and the far side of the specimen has yielded.

$$\text{Net Section Yield Occurs When: } \sigma_{\infty} = \frac{1}{2} (\sigma_u + \sigma_y) \left(1 - \frac{a}{w}\right) \quad (3.2)$$

where:

σ_{∞} \equiv remote stress

σ_y \equiv yield stress

σ_u \equiv ultimate stress

w \equiv specimen width

The net section yield line is drawn as the solid line in Figure 3.4. The fatigue tests have to be conducted above the threshold level and below the critical level. Additionally, in order to have a minimum of plasticity, it is desired to stay below the yield line. The cross-hatched area of the plots show the design region. Note that the near threshold and critical values were determined with experimental data. Thus, when the first tests for each specimen angle were performed, only the yield line was known.

Data Acquisition

All fatigue tests were performed using an MTS Model 810 testing machine. The MTS was set up in load control on the 10% range with maximum loading of ± 5000 pounds. All testing was done in an air environment at room temperature, using a 10 Hz sinusoidal loading with a minimum load near zero.

Crack length and cycle data were collected using the apparatus pictured in Figure 3.5. In order to see the crack, Spotcheck penetrant (#SKL-H) was applied on the specimen. The excess dye was wiped off with cleaner/remover (#SKD-NF/ZC-7B). A developer (#SKD-NF/ZP-9B) was then sprayed on to draw the remaining dye out of the crack, leaving behind a bright red mark where the crack was. The dye penetrant materials were obtained from Magnaflux Corporation, of Chicago, Illinois.

A travelling microscope was used to measure the size of the crack. The microscope is manufactured by Precision Tool and Instrument Co., Ltd., and yields a magnification of 7x. The crack length was obtained by measuring the position of the edge and the position of the crack tip, then subtracting one from the other. Note that in the 45 and 15 degree off-axis tests, the crack length was measured as a projected crack length perpendicular to the loading and subsequently modified to obtain the actual crack length. This was done because it was not possible to get accurate measurements otherwise. This method of measuring the crack was accurate to ± 0.003 inch. The cycle count was recorded on a digital indicator on the MTS.

Fatigue Precracking

The American Society for Testing and Materials (ASTM) recommends that the fatigue precrack be a minimum of 0.1 times the specimen thickness, or the width of the notch, whichever is greater [17]. The guidelines were adhered to in the following way. The specimens were cycled until a steady rate of crack growth was achieved. This usually amounts to a precrack close to the ASTM recommendations.

Precracking was achieved in the following manner. A load level near the desired testing level, above the threshold level, was used to grow the crack. If a uniform crack growth rate was produced, the data was collected. If the crack had not grown after 25,000 or more cycles, the load was raised. This process was continued until a steady crack growth rate was established. The load level was then lowered in steps to the desired testing load level. The data were then collected.

The ASTM suggests [17] that the loads be reduced by no more than 20 percent and that the crack length extension over each step be determined by the equation:

$$\Delta a_{\min} = \frac{3}{\pi} \left[\frac{K'_{\max}}{\sigma_y} \right]^2 \quad (3.3)$$

where:

Δa_{\min} = Minimum Crack Extension

K'_{\max} = Maximum Stress Intensity Factor at Previous Loading

σ_y = Yield Stress

The main disadvantage of this method is that it was developed for isotropic materials, but the role of plasticity in anisotropic materials is not very well understood and could be quite different. Thus, the ASTM method was not used. Instead, the load level was lowered in small decrements until the desired level was reached. The duration of each decrement was such that a uniform crack growth rate was achieved.

90 DEGREE BASELINE TESTS

Three baseline fatigue tests were performed on specimens A10, C2, and C3.

A test on specimen A10 was first performed. In an attempt to find a threshold load level, the loading was started at a low level and gradually raised until the crack started to grow. The specimen was first cycled 5000 times using a maximum cyclic stress of 2143 psi

and a minimum stress of approximately zero. There was no observable crack growth up to this point. The maximum stress was raised to 3215 psi and the specimen was cycled an additional 5000 cycles with no crack growth. This process was repeated until, at a maximum cyclic stress of 9644 psi and stress ratio of $R = 0.01$, a small crack was observed after 10,000 cycles. Crack length versus cycles data were then collected.

Specimen C2 was tested next. The specimen was cycled 139,100 times, using a maximum cyclic stress of 2500 psi and minimum of 200 psi, without any observable crack growth. The load was then increased to a maximum cyclic stress of 3750 psi and a minimum of 225 psi. There was no crack growth after 90,500 cycles. The load was then increased to a maximum cyclic stress of 5000 psi and a minimum of 250 psi and cycled for 125,000 cycles with no crack growth. Increasing the maximum cyclic stress to 6166 psi caused the crack to extend 0.166 inch after only 30,000 cycles. This gave the impression that the threshold was actually well below this level. The load level was decreased to the original level to try and locate the threshold again. After 25,000 cycles at the original stress level the crack did not grow. The stress level was increased to a maximum of 3750 psi, and there was no crack growth after 35,000 cycles. The stress level was raised to a maximum of 5000 psi, giving no new crack growth after 30,000 cycles. The stress level was raised to a maximum of 5725 psi and the specimen cycled 40,000 times giving no crack growth. The load was then raised to the level at which the crack had previously grown and after 30,000 cycles there was still no growth. Finally, the

stress level was increased to a maximum of 6650 psi and minimum of 220 psi at which point the crack started growing again. The stress ratio was $R = 0.03$. The fatigue data were then collected

The next test was performed on specimen C3. The initial cyclic stress levels had a maximum stress of 9000 psi and a minimum stress of 220 psi. After 15,000 cycles, short discontinuous cracks had formed. The maximum stress was lowered to 7000 psi and the specimen given 1,368,000 cycles with no observable growth. This was similar to the initial crack growth behavior of specimen C2. The maximum cyclic stress was raised back to the original level to see if plasticity caused by the higher load had prevented the crack from growing at the lower load. After 13,000 cycles, the crack grew 0.075 inch. The load was then reduced in 500 psi decrements. The maximum cyclic stress was lowered to 8500 psi and after 12,500 cycles, the crack extended 0.071 inch. The maximum stress was then lowered to 8000 psi and after 7000 cycles, the crack extended 0.019 inch. The maximum cyclic stress was then lowered to 7500 psi and gave 0.008 inch of crack growth in 10,000 cycles. At 7000 psi maximum stress, there was no growth after 65,000 cycles, so the level was raised to a maximum of 7500 psi and minimum of 220 psi. This gave a stress ratio of 0.03. The remainder of the test was conducted at this level.

Crack length versus cycles data are plotted in Figure 3.6. Notice that these plots look similar to corresponding ones for homogeneous materials in that the crack growth rate increases as the crack length increases.

45 DEGREE BASELINE TESTS

One 45 degree baseline test was performed on specimen D1.

A maximum cyclic stress of 7000 psi and minimum of 200 psi was applied to specimen D1. The corresponding stress ratio was 0.03. The crack started to grow immediately at this level in the direction along the fibers and continued until fracture at a crack length of 1.817 inches. Note that the direction of crack growth differs from what might be expected in a homogeneous material. Crack length measurements were made by measuring the horizontal distance from the edge to the crack tip and dividing by the sin of 45 degrees.

Crack length versus cycles data are plotted in Figure 3.7. Again, this plot looks similar to that for a homogeneous material.

15 DEGREE BASELINE TESTS

Five 15 degree baseline tests were conducted on specimens A2, C6, C7, C8b, and C9.

The first baseline test was done on specimen A2. The notch was machined into the specimen perpendicular to the edge. To initiate the crack, a maximum cyclic stress of 15,820 psi and minimum of 550 psi was applied for 200 cycles. The crack turned and grew along the fibers a distance of 0.007 inch. The stress level was then lowered to a maximum of 11,020 psi and minimum of 236 psi, giving a stress ratio of 0.02. The crack was grown at this level to 2.543 inches after 83,000 cycles. Crack length measurements were made by measuring the horizontal distance from the edge to the crack tip and dividing by the sin of 15 degrees.

The second baseline test was on specimen C6. The notch put in this and all subsequent 15 degree specimens was machined at a 15 degree angle to the applied loading. Thus, it was along the fibers. It was desired to find a threshold level. A maximum cyclic stress of 6000 psi and minimum of 191 psi was first used. After 65,000 cycles, the crack grew 0.009 inch along the fibers. The maximum stress was then raised to 7000 psi and after 60,000 cycles, the crack grew 0.005 inch. The maximum stress was raised to 8000 psi and the crack extended 0.132 inch in 930,000 cycles. The maximum stress was raised to 8500 psi. The crack grew 0.008 inch in 110,000 cycles giving an even slower crack growth rate than the previous loading conditions. The stress was again increased to a maximum of 9000 psi and minimum of 319 psi and the crack grew 0.012 in 202,000 cycles. This was still a slower rate of growth than the last two conditions. The maximum stress was raised to 10,000 psi giving a stress ratio of 0.03. The crack grew at this level for the rest of the test. Notice that the rate of crack growth was at first high, then slowed down, and finally increased again, just as in some of the 90 degree specimens.

The third specimen tested was C7. A maximum stress of 10,000 psi and minimum of 320 psi was applied for 350,000 cycles. During this time, the crack grew 0.070 inch along the fibers in the first 175,000 cycles with no new growth in the remaining 175,000 cycles. The maximum stress was raised to 10,500 psi which gave a crack extension of 0.132 inch in 725,000 cycles. The crack growth was very sporadic; sometimes growing rapidly and sometimes not at all.

The stress was raised to a maximum of 11,000 psi which gave a crack growth of 0.024 inch in 20,000 cycles and no crack growth for the next 50,000. The maximum stress was increased to 11,500 psi. There was no crack growth in 70,000 cycles. Increasing the maximum stress to 12,500 psi finally made the crack grow regularly. The resulting stress ratio was 0.03 and the test was finished at the level.

A fourth baseline test was performed on specimen C8. The initial stresses were a maximum of 10,000 psi and a minimum of 322 psi. The crack grew 0.160 inch along the fiber direction in 1,300,000 cycles. The growth was very irregular with a period of fast growth in the beginning and finally stopping at the end.

Specimen C8 was then cut longitudinally about a half inch from the edge with the crack in it and renamed C8b. This was done to see if fibers adjacent to the crack, which were locked in both the upper and lower grips, caused the crack to arrest. A notch was cut into it so that the fibers adjacent to the crack were free from the grips. A maximum cyclic stress of 10,000 psi grew the crack 0.175 inch along the fibers in 610,000 cycles. During the next 133,000 cycles though there was no growth. The maximum cyclic stress was changed to 10,500 psi. Irregular crack growth occurred in the next 160,000 cycles. The maximum cyclic stress was raised in increments of 500 psi with the same results until the maximum stress was 13,000 psi. The crack grew continually and the rest of the test was performed at this loading. The stress ratio was 0.02.

The observed irregularity in the crack growth is believed to have been caused by the applied loads being too close to the threshold

level. To confirm this, a final baseline test was performed on specimen C9. The specimen was cut to the same dimensions as C8b. At a maximum stress of 13,000 psi and minimum of 200 psi, the crack grew 0.157 inch along the fibers in 270,000 cycles, rapidly at first, then slowing down. The maximum stress was raised to 13,500 psi. At this stress level, the crack grew steadily. The data were then collected. The stress ratio was 0.01.

The fatigue data for specimens A2, C6, C7, C8b, and C9 are plotted in Figure 3.8.

PRELIMINARY DATA REDUCTION

Crack growth rates were found by computing the slope of the crack length versus cycles curves using a linear least squares technique with three points. A utility computer program called MAKEFILE.F was used for this operation. The values of $\Delta\sigma\sqrt{\pi a}$ were also computed. The \log_{10} of these quantities were taken and plots of $\log_{10} da/dN$ versus $\log_{10} \Delta\sigma\sqrt{\pi a}$ were produced. The plots for the 90 degree specimens are shown in Figure 3.9. The plot for the 45 degree specimen is shown in Figure 3.10. Figure 3.11 shows the plots for the 15 degree specimens. Notice that in Figure 3.11 the reduced data for specimens A2, C6 and C7 do not fall in line with the reduced data from specimens C8b and C9. Since A2, C6 and C7 were cycled at lower loads, the difference may be due to the fact that these loads are near the threshold level and thus there is a lot of scatter in the data. The data from A2, C6 and C7 is not considered further.

DISCUSSION

Saw cutting the specimens was superior to using the EDM from the standpoint of convenience and accuracy. It is relatively easy to establish a design criterion for the fatigue specimens once the ultimate and yield stresses for the different fiber orientations have been obtained. An automated approach in the measurement of the fatigue crack would have been less time consuming than the current procedure.

The baseline fatigue tests for the 90, 45, and 15 degree specimens show that the fatigue crack growth is similar to that of homogeneous materials. Observation of the $\log_{10} da/dN$ versus $\log_{10} \Delta\sigma\sqrt{\pi a}$ plots indicate that there can be a considerable amount of scatter at crack growth rates near the threshold level. This is particularly evident in the data from the 15 degree tests of specimens A2, C6, and C7. Crack growth in the 45 and 15 degree specimens is mixed mode,

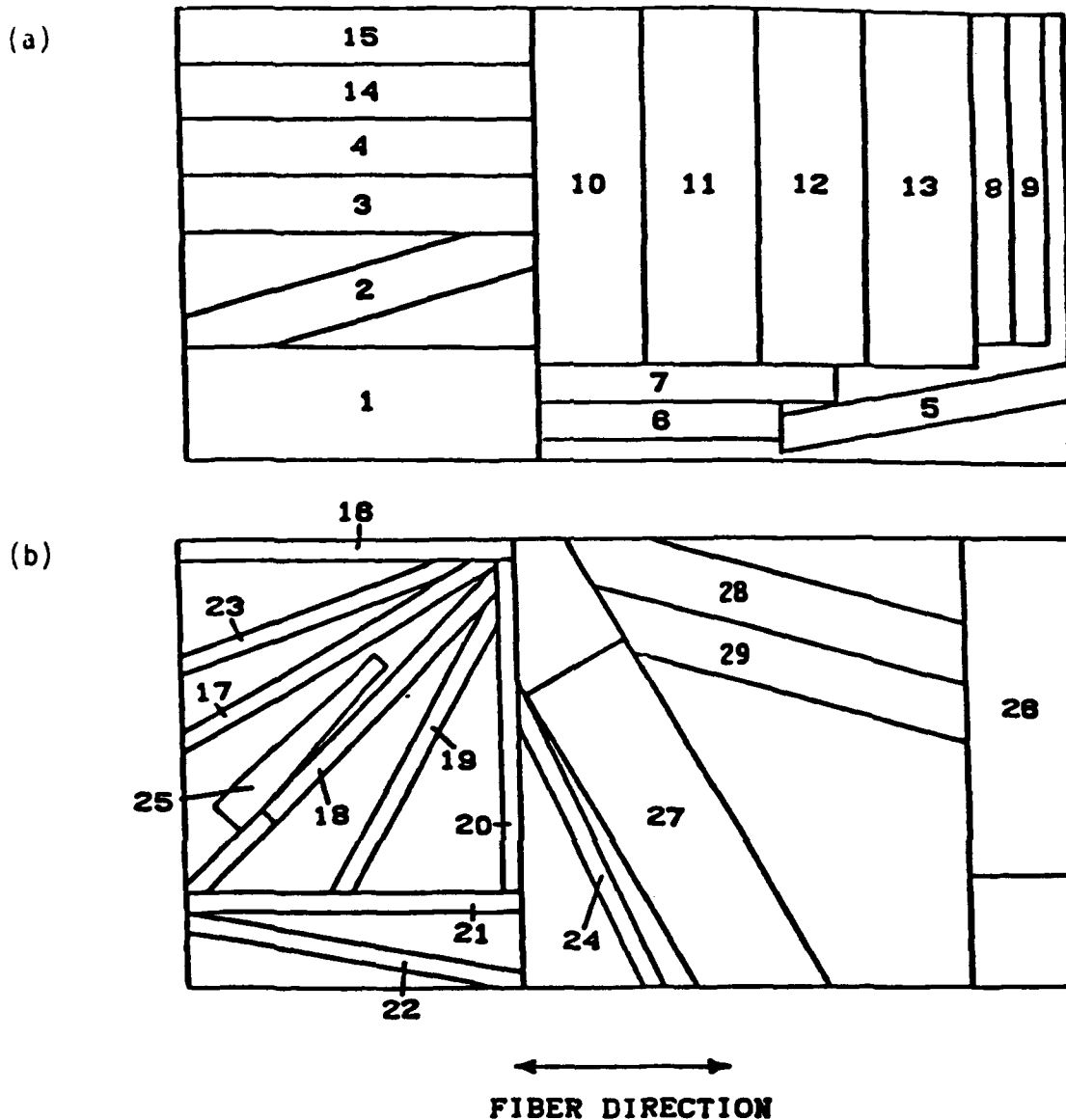
The scatter observed in the data at small crack lengths, regardless of the applied loading, is probably caused by local damage to the material when the notch roots are tapped with the razor blade.

Table 3.1 A listing of fatigue and characterization specimens cut from plates A and B as shown in Figure 3.1.

Specimen	Fiber Angle (Deg)	Dimensions (t x w x l) (inches)	Notch Size (inches)	Use
A2	15	.0770x1.65x10.0	0.465	Fatigue
A10	90	.0770x3.03x9.5	0.148	Fatigue
A11	90	.0770x3.08x9.5	0.150	Fatigue + 1.50x Overload
A12	90	.0770x3.061x9.7	0.136	Fatigue + 1.50x Overload
A13	90	.0770x3.07x9.7	0.142	Fatigue
B17	30	.0780x.502x10.0	-----	Uniaxial
B18	45	.0780x.527x9.0	-----	Uniaxial
B19	60	.0780x.524x9.0	-----	Uniaxial
B20	90	.0780x.538x9.3	-----	Uniaxial
B21	0	.0775x.500x9.0	-----	Uniaxial
B22	10	.0770x.443x9.0	-----	Uniaxial
B23	20	.0780x.465x8.0	-----	Uniaxial
B25	45	.0780	-----	Tapered
B26	90	.0775x2.950x9.8	0.163	Transverse Crack
B27	60	.0775x2.950x9.5	0.312	Oblique Crack
B28	15	.0780x1.491x5.7	1.019	Fatigue + 1.92x Overload
B29	15	.0780x1.571x5.7	1.077	Fatigue + 1.61x Overload

Table 3.2 A listing of fatigue and characterization specimens cut from plates C and D as shown in Figure 3.2.

Specimen	Fiber Angle (Deg)	Dimensions (t x w x l) (inches)	Notch Size (inches)	Use
C1	90	.0780x2.952x9.5	0.906	Fatigue + 1.25x Overload
C2	90	.0780x2.911x9.5	0.263	Fatigue
C3	90	.0780x2.918x9.5	0.173	Fatigue
C4	90	.0780x2.986x9.5	0.854	Fatigue + 1.35x Overload
C5	90	.0780x2.995x9.5	0.810	Fatigue + 1.45x Overload
C6	15	.0780x2.010x5.6	1.065	Fatigue
C7	15	.0780x2.001x5.4	1.104	Fatigue
C8b	15	.0780x1.993x5.7	0.837	Fatigue
C9	15	.0780x1.452x5.7	1.030	Fatigue
C10	15	.0770x1.509x5.8	1.110	Fatigue + 1.25x Overload
D1	45	.0780x1.977x6.1	0.694	Fatigue
D2	45	.0780x1.987x6.0	0.716	Fatigue + 1.25x Overload
D3	45	.0780x1.980x6.1	0.687	Fatigue + 1.35x Overload
D4	90	.0780x2.940x6.0	-----	Hole



SIZE: 12" x 24" x .077"

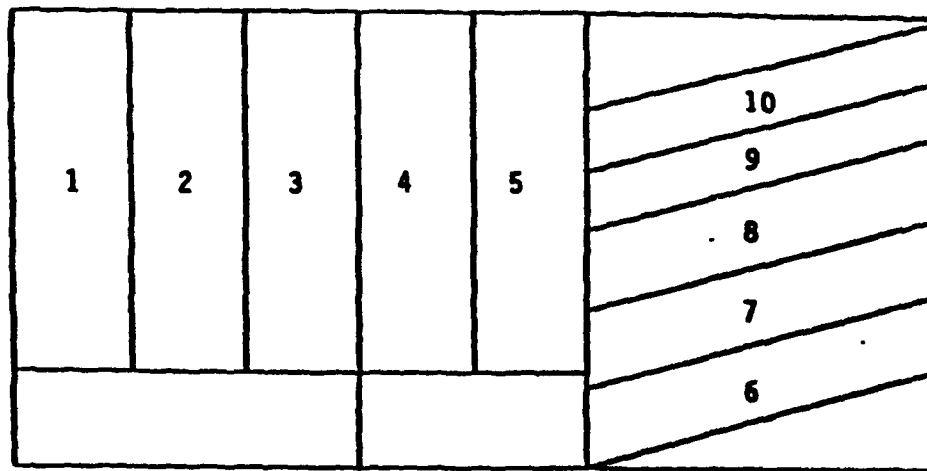
MATRIX / FILAMENT: 6061 Al / 5.6 B

11 PLIES, UNIDIRECTIONAL

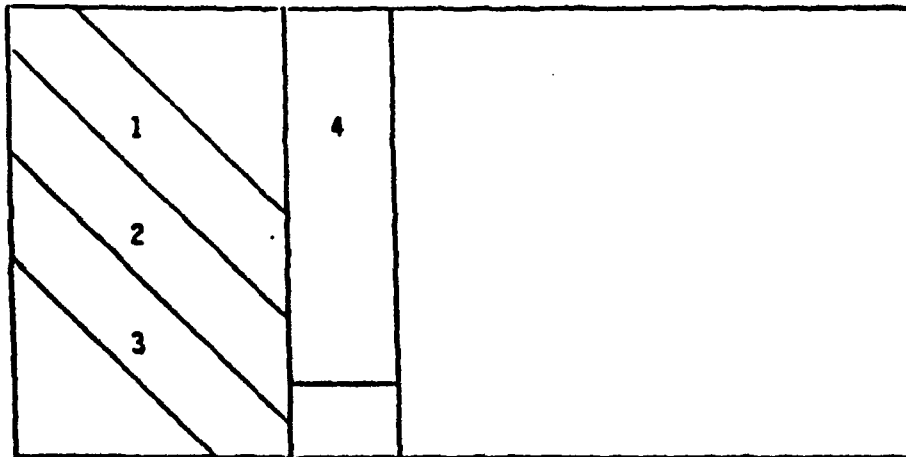
VOLUME FRACTION: 47.5% Fibers

Figure 3.1 Specimen cutting plan for plates A and B, in (a) and (b), respectively .

(a)



(b)



←→
FIBER DIRECTION

SIZE: 12" x 24" x .078"

MATRIX / FILAMENT: 6061 Al / 5.6 B

11 PLIES, UNIDIRECTIONAL

VOLUME FRACTION: 47.5% Fibers

Figure 3.2 Specimen cutting plan for plates C and D, in (a) and (b), respectively .

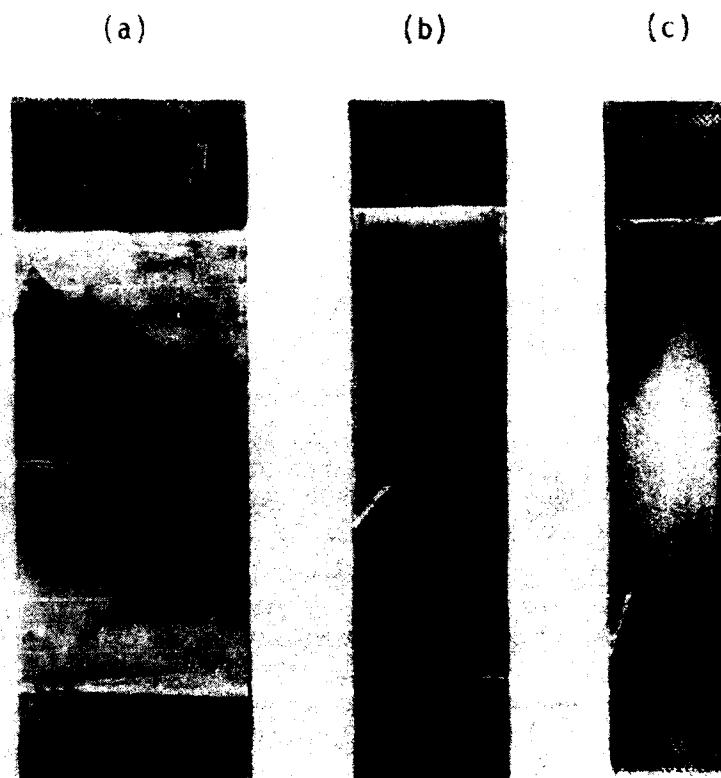


Figure 3.3 Some typical fatigue specimens. 90, 45, and 15 degree specimens shown in (a), (b), and (c), respectively.

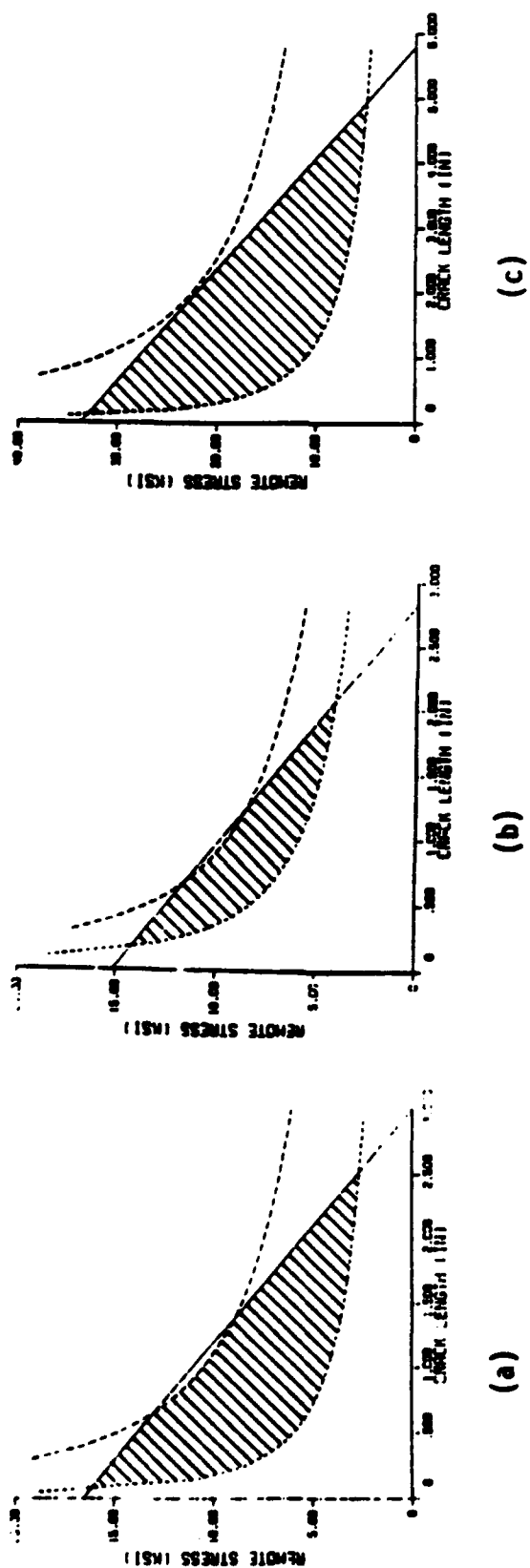


Figure 3.4 Fatigue specimen design curves for 90, 45, and 15 degree orientations in (a), (b), and (c), respectively. Hatched areas represent the design region.



Figure 3.5 Photograph of the experimental setup used in the fatigue testing. A travelling microscope was used to measure the crack length and the MTS recorded the cycles .

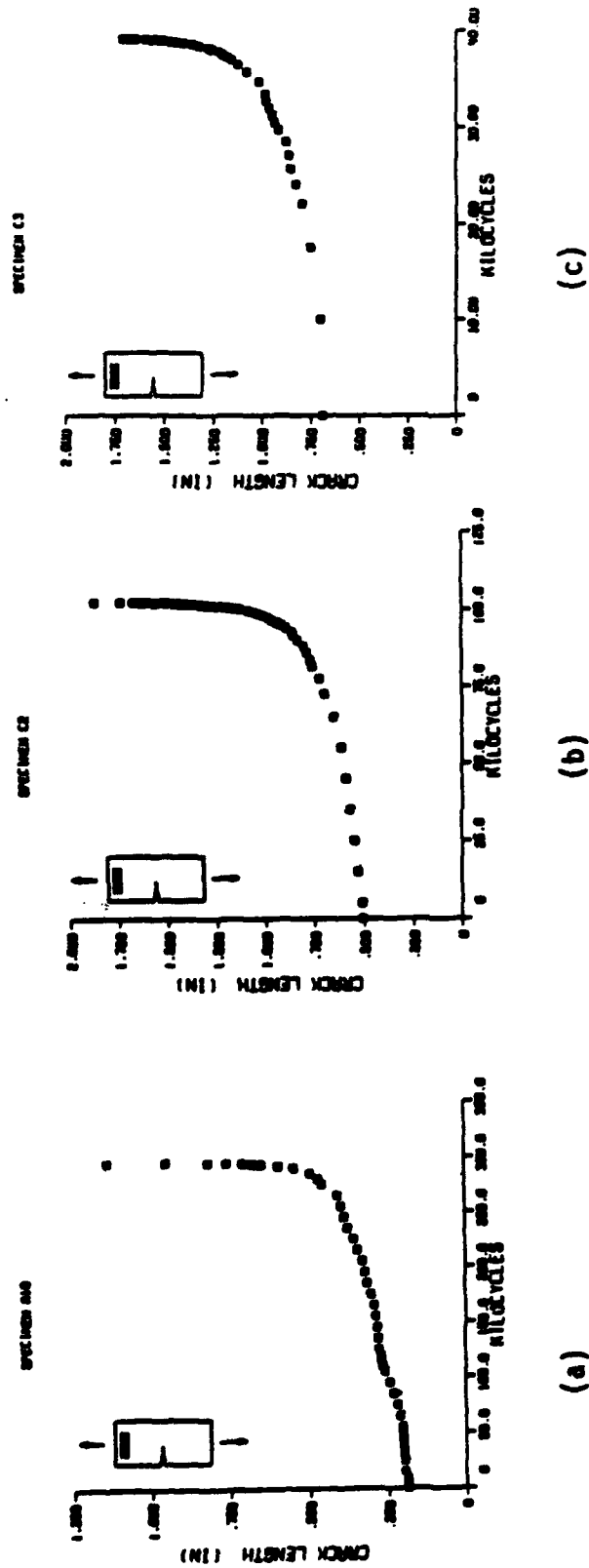


Figure 3.6 Crack growth data for 90 degree baseline tests.
 (a) Specimen A10 - $\Delta\sigma = 9537$ psi, $R = 0.01$.
 (b) Specimen C2 - $\Delta\sigma = 6430$ psi, $R = 0.03$.
 (c) Specimen C3 - $\Delta\sigma = 7280$ psi, $R = 0.03$.

SPECIMEN 01

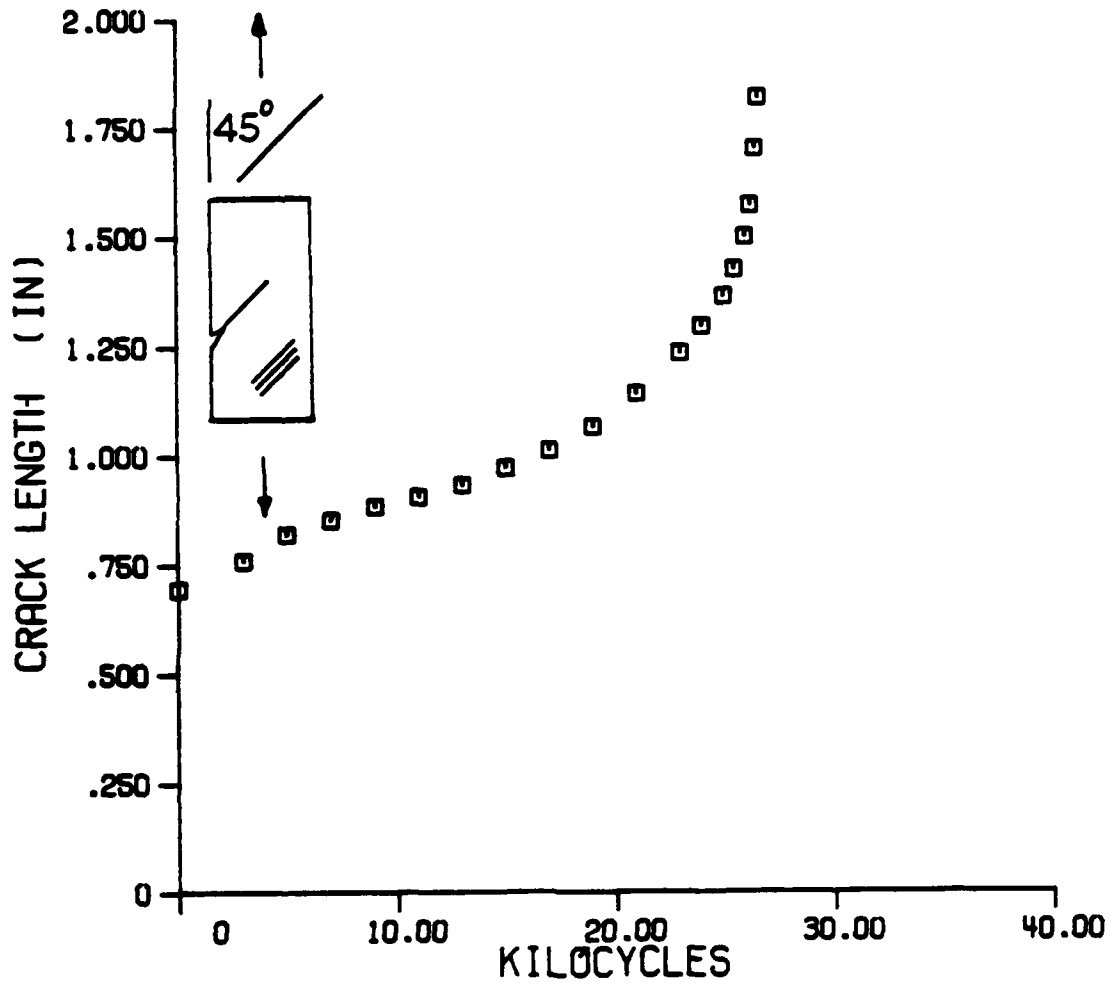


Figure 3.7 Crack growth data for 45 degree baseline specimen 01. $\Delta\sigma = 6,800$ psi, $R = 0.03$.

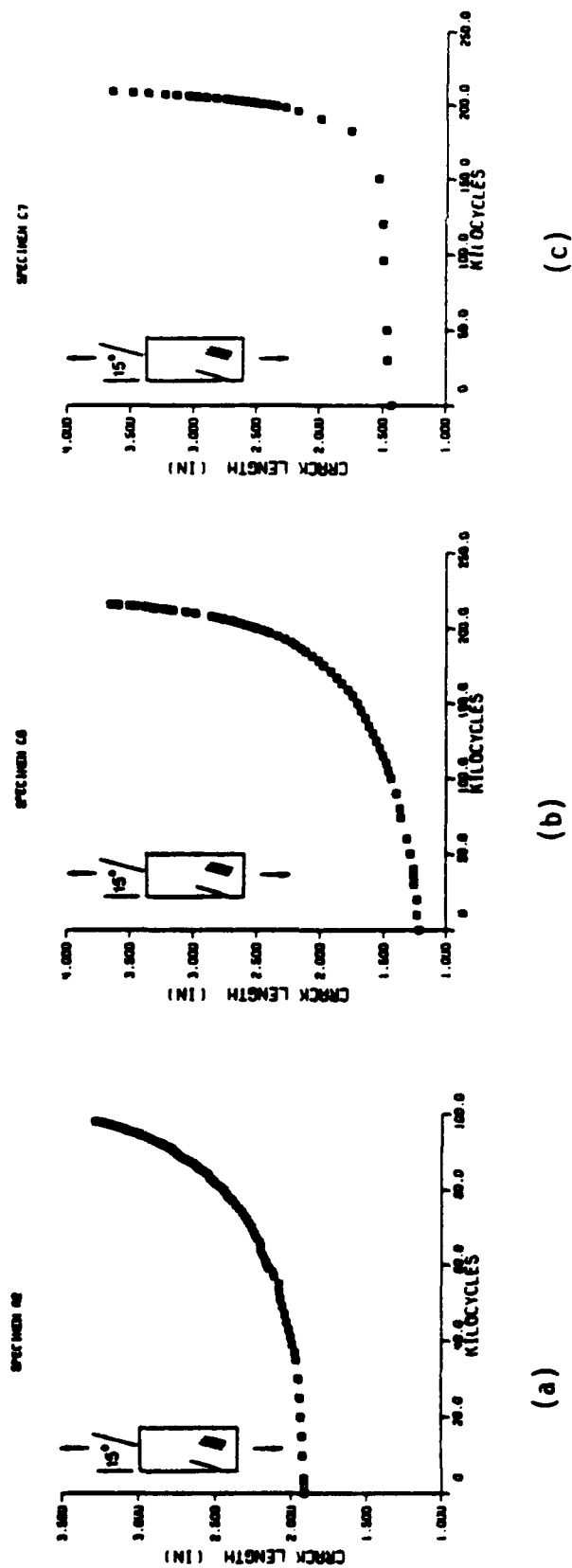


Figure 3.8 Crack growth data for 15 degree baseline tests.
 (a) Specimen A2 - $\Delta\sigma = 10,784$ psi, $R = 0.01$.
 (b) Specimen C6 - $\Delta\sigma = 9,681$ psi, $R = 0.03$.
 (c) Specimen C7 - $\Delta\sigma = 12,180$ psi, $R = 0.03$.
 (d) Specimen C8b - $\Delta\sigma = 12,800$ psi, $R = 0.02$.
 (e) Specimen C9 - $\Delta\sigma = 13,300$ psi, $R = 0.01$.

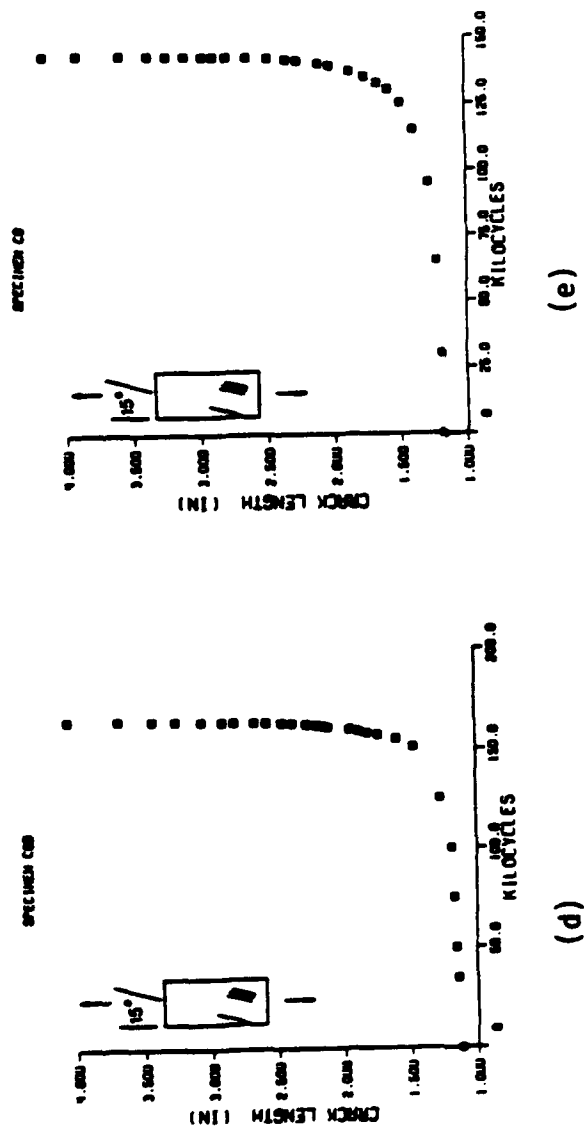


Figure 3.8 continued

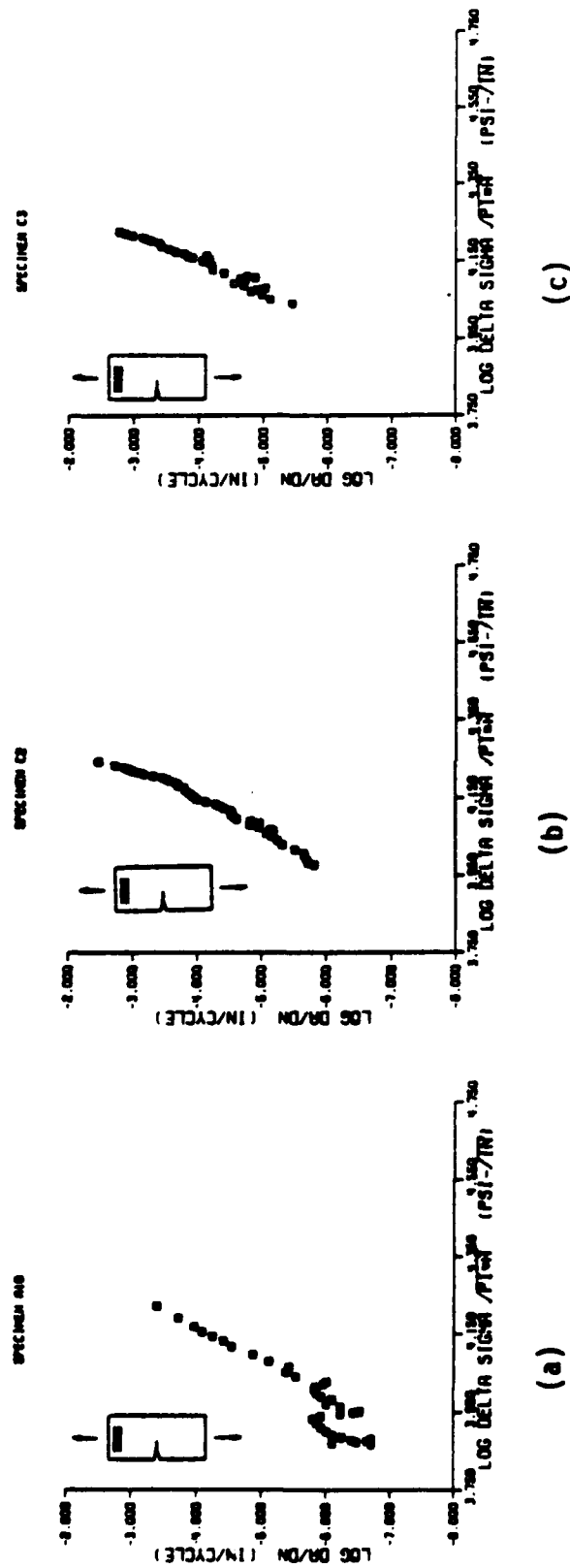


Figure 3.9 Crack growth rate data for 90 degree baseline tests.
 (a) Specimen A10 - $\Delta\sigma = 9537$ psi, $R = 0.01$.
 (b) Specimen C2 - $\Delta\sigma = 6430$ psi, $R = 0.03$.
 (c) Specimen C3 - $\Delta\sigma = 7280$ psi, $R = 0.03$.

SPECIMEN D1

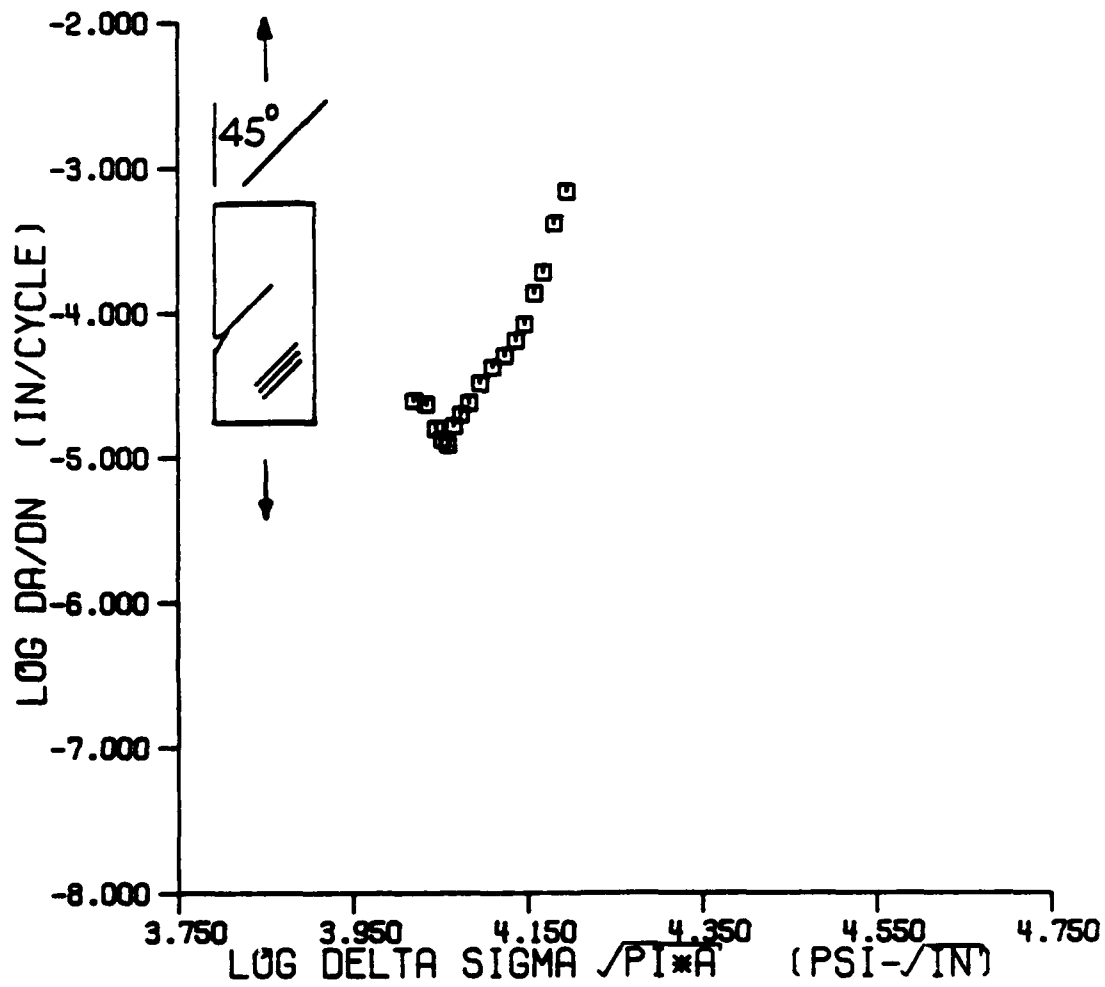


Figure 3.10 Crack growth rate data for 45 degrees baseline specimen D1. $\Delta\sigma = 6,800 \text{ psi}$, $R = 0.03$.

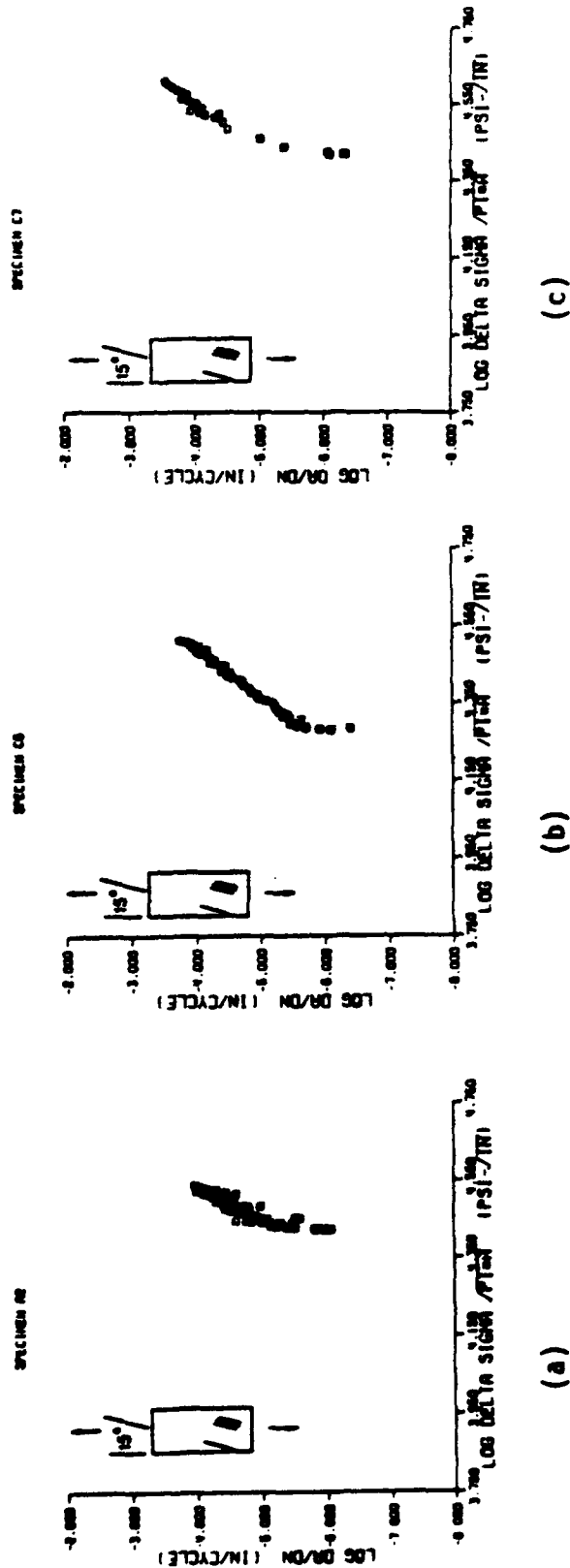
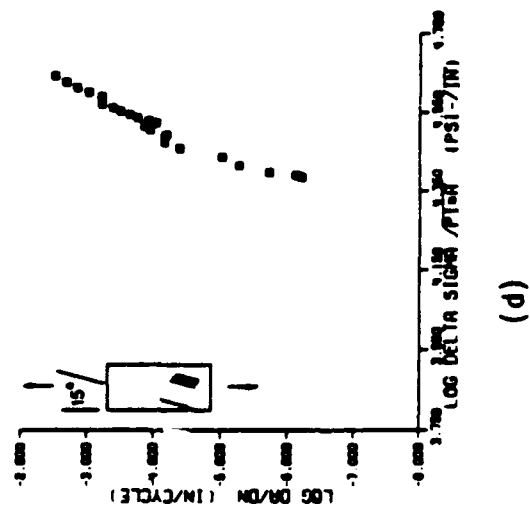
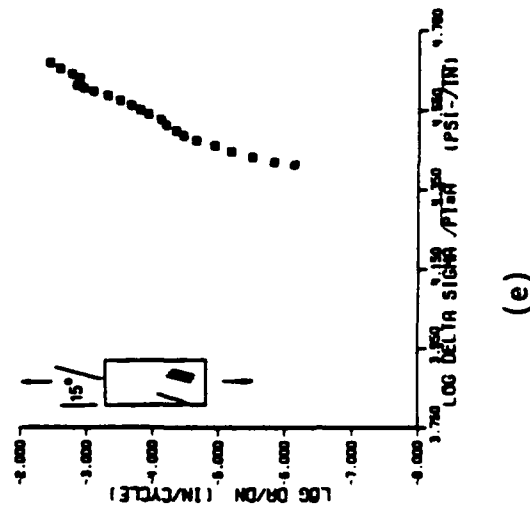


Figure 3.11 Crack growth rate data for 15 degree baseline tests.

(a) Specimen A2 - $\Delta \sigma = 10,784$ psi, $R = 0.01$.
 (b) Specimen C6 - $\Delta \sigma = 9,681$ psi, $R = 0.03$.
 (c) Specimen C7 - $\Delta \sigma = 12,180$ psi, $R = 0.03$.
 (d) Specimen C8b - $\Delta \sigma = 12,800$ psi, $R = 0.02$.
 (e) Specimen C9 - $\Delta \sigma = 13,300$ psi, $R = 0.01$.



(d)



(e)

Figure 3.11 continued

SECTION 4: DATA REDUCTION AND CORRELATION

It is necessary to establish a means of correlating all the baseline data. That is, it is necessary to have an effective stress intensity factor which characterizes the various geometries and orientations in a single $\log_{10} da/dN$ versus $\log_{10} \Delta K_{eff}$ curve. Once an effective stress intensity factor is developed, a least squares fit of the individual $\log_{10} da/dN$ versus $\log_{10} \Delta K_{eff}$ curves is performed to determine the Paris Law constants, c and n , in the equation

$$\frac{da}{dN} = c \Delta K_{eff}^n \quad (4.1)$$

These constants are then used to model the crack growth for a particular specimen.

ANISOTROPIC STRESS INTENSITY FACTOR FORMULATION

The following is a motivational, rather than rigorous, development of an effective stress intensity factor.

Consider a sheet of isotropic material. A failure criterion for plane stress can be written as:

$$\sigma_f^2 = \sigma_{xx}^2 + \sigma_{yy}^2 + \sigma_{xx}\sigma_{yy} + 3\sigma_{xy}^2 \quad (4.2)$$

or

$$\bar{\sigma} = \sigma_f = \sqrt{\sigma_{xx}^2 + \sigma_{yy}^2 + \sigma_{xx}\sigma_{yy} + 3\sigma_{xy}^2} \quad (4.3)$$

For an anisotropic material, the effective stress and failure criterion may be written as

$$\bar{\sigma} = \sigma_f = \sqrt{a_{11}\sigma_{11}^2 + \sigma_{22}^2 + 2a_{12}\sigma_{11}\sigma_{22} + 2a_{66}\sigma_{12}^2} \quad (4.4)$$

where the subscripts 1 and 2 refer to the principal material directions.

The anisotropy may be introduced by a reinforcing effect, such as fibers, or a weakening effect, such as a crack

Consider the case of the crack. The classical behavior of $\sqrt{\pi a}$ dependence on the crack size may be incorporated into (4.4) giving:

$$\begin{aligned} \bar{\sigma}\sqrt{\pi a} &= \sigma_f \sqrt{\pi a} = \\ &[a_{11}(\sigma_{11}\sqrt{\pi a})^2 + (\sigma_{22}\sqrt{\pi a})^2 + 2a_{12}(\sigma_{11}\sqrt{\pi a})(\sigma_{22}\sqrt{\pi a}) \\ &+ 2a_{66}(\sigma_{12}\sqrt{\pi a})^2]^{1/2} \end{aligned} \quad (4.5)$$

This can be viewed as the failure criterion that accounts for crack size. Define the quantities analogous to stress intensity factors as:

$$\begin{aligned}
\bar{K} &\equiv \bar{\sigma}\sqrt{\pi a} & K_{11} &\equiv \sigma_{11}\sqrt{\pi a} \\
K_{22} &\equiv \sigma_{22}\sqrt{\pi a} & K_{12} &\equiv \sigma_{12}\sqrt{\pi a}
\end{aligned} \tag{4.6}$$

so that (4.5) may be rewritten as:

$$\bar{K} = \sqrt{a_{11}K_{11}^2 + K_{22}^2 + 2a_{12}K_{11}K_{22} + 2a_{66}K_{12}^2} \tag{4.7}$$

This can also be thought of as a definition of an effective stress intensity factor. Equation (4.7) is valid for an infinite sheet. If the K's are written as:

$$\begin{aligned}
K_{11} &\equiv \sigma_{11}\sqrt{\pi a} f_{11}(a/w) \\
K_{22} &\equiv \sigma_{22}\sqrt{\pi a} f_{22}(a/w) \\
K_{12} &\equiv \sigma_{12}\sqrt{\pi a} f_{12}(a/w)
\end{aligned} \tag{4.8}$$

where (a/w) is the crack length to width ratio, then (4.8) is valid for finite width sheets. Note that it is assumed that the crack extends in the 1 direction.

Near Field Interpretation of K Effective

The expansion of the stress field in the vicinity of the crack at $\phi = 0$ degrees, for an orthotropic material, can be written as [18]:

$$\begin{aligned}
\sigma_{11} &= \frac{K_I}{\sqrt{2\pi r}} \operatorname{Re}[-\mu_1 \mu_2] + \frac{K_{II}}{\sqrt{2\pi r}} \operatorname{Re}[-(\mu_1 + \mu_2)] - \sigma_0 + O(r^{1/2}) \\
\sigma_{22} &= \frac{K_I}{\sqrt{2\pi r}} + O(r^{1/2}) \\
\sigma_{12} &= -\frac{K_{II}}{\sqrt{2\pi r}} + O(r^{1/2})
\end{aligned} \tag{4.9}$$

where r is the distance along the line $\phi = 0$, and μ_1 and μ_2 are related to the material properties.

For an orthotropic material and the crack along a principal direction, μ_1 and μ_2 are purely imaginary and (4.9) becomes:

$$\begin{aligned}
\sigma_{11} &= -\frac{K_I}{\sqrt{2\pi r}} \mu_1 \mu_2 - \sigma_0 + O(r^{1/2}) \\
\sigma_{22} &= \frac{K_I}{\sqrt{2\pi r}} + O(r^{1/2}) \\
\sigma_{12} &= -\frac{K_{II}}{\sqrt{2\pi r}} + O(r^{1/2})
\end{aligned} \tag{4.10}$$

Note the presence of the σ_0 term which is related to the remote loads. For example, for an infinite sheet with remote 11 and 22 stresses,

$$K_I = \sigma_{22_\infty} \sqrt{\pi a} \quad \sigma_0 = (\sigma_{22_\infty} - \sigma_{11_\infty})$$

For problems with complicated geometries, the value of K_I changes but not the form of the stress distribution. The same is true for σ_0 .

Define the stress intensity factors as:

$$\begin{Bmatrix} K_{11} \\ K_{22} \\ K_{12} \end{Bmatrix} = \lim_{\substack{r \rightarrow r^* \\ \phi = 0}} \begin{Bmatrix} \sigma_{11} \sqrt{2\pi r} \\ \sigma_{22} \sqrt{2\pi r} \\ -\sigma_{12} \sqrt{2\pi r} \end{Bmatrix} \quad (4.11)$$

giving

$$\begin{aligned} K_{11} &= -K_I \mu_1 \mu_2 - \sigma_0 \sqrt{2\pi r^*} \\ K_{22} &= K_I \\ K_{12} &= K_{II} \end{aligned} \quad (4.12)$$

Rewriting the σ_0 term as:

$$\sigma_0 \sqrt{2\pi r^*} = \sigma_0 \sqrt{2\pi a} \sqrt{\frac{r^*}{a}} = K_0 \sqrt{2\frac{r^*}{a}}$$

gives

$$\begin{aligned} K_{11} &= -K_I \mu_1 \mu_2 - K_0 \sqrt{2\frac{r^*}{a}} \\ K_{22} &= K_I \\ K_{12} &= K_{II} \end{aligned} \quad (4.13)$$

This definition is expected to be most useful when plasticity is present. Substitution of Equations (4.13) into (4.7) gives

$$\begin{aligned}\bar{K}^2 = & a_{11}(K_I^2 \mu_1^2 \mu_2^2 + 2K_I K_O \mu_1 \mu_2 \sqrt{2\frac{r^*}{a}} + K_O^2 2\frac{r^*}{a}) + K_I^2 \\ & + 2a_{12}(-K_I^2 \mu_1 \mu_2 - K_I K_O \sqrt{2\frac{r^*}{a}}) + 2a_{66} K_{II}^2\end{aligned}\quad (4.14)$$

or regrouping the coefficients

$$\bar{K}^* = \sqrt{a_{11}^* K_I^2 + a_{oo}^* (2\frac{r^*}{a}) K_O^2 + 2a_{10}^* K_I K_O \sqrt{2\frac{r^*}{a}} + 2a_{66}^* K_{II}^2} \quad (4.15)$$

Normalizing (3.15) with $a_{11}^* = 1$ gives,

$$\bar{K}^* = \sqrt{K_I^2 + a_{oo} (2\frac{r^*}{a}) K_O^2 + 2a_{10} K_I K_O \sqrt{2\frac{r^*}{a}} + 2a_{66} K_{II}^2} \quad (4.16)$$

The presence of the K_O term is always associated with a $\sqrt{2r^*/a}$ term. Thus, by setting $r^* = 0$, biaxial effects can be neglected.

For off-axis testing, the stresses in the principal material directions are:

$$\begin{aligned}\sigma_{11} &= \sigma_{\infty} \cos^2 \theta \\ \sigma_{22} &= \sigma_{\infty} \sin^2 \theta \\ \sigma_{12} &= \sigma_{\infty} \sin \theta \cos \theta \\ \sigma_0 &= \sigma_{22} - \sigma_{11} = \sigma_{\infty} (\sin^2 \theta - \cos^2 \theta)\end{aligned}\quad (4.17)$$

where θ is the angle between the loading direction and the fiber direction. This modifies Equations (4.8) to:

$$\begin{aligned}
K_I &= \sigma_{\infty} \sqrt{\pi a} \sin^2 \theta f_1(a/w, \theta) \\
K_{II} &= \sigma_{\infty} \sqrt{\pi a} \sin \theta \cos \theta f_2(a/w, \theta) \\
K_0 &= \sigma_{\infty} \sqrt{\pi a} (\sin^2 \theta - \cos^2 \theta) f_0(a/w, \theta) .
\end{aligned} \tag{4.18}$$

Combining (4.16) and (4.18) yields:

$$\begin{aligned}
\bar{K}^* &= \left\{ [f_1^2 + a_{00}(2\frac{r^*}{a})f_0^2 + 2a_{10} \sqrt{2\frac{r^*}{a}} f_1 f_0] \sin^4 \theta \right. \\
&\quad + [a_{00}(2\frac{r^*}{a})f_0^2] \cos^4 \theta + 2[-a_{00}(2\frac{r^*}{a})f_0^2 - a_{10} \sqrt{2\frac{r^*}{a}} f_1 f_0 \\
&\quad \left. + a_{66}f_2^2] \sin^2 \theta \cos^2 \theta \right\}^{1/2} \sigma_{\infty} \sqrt{\pi a} .
\end{aligned} \tag{4.19}$$

For the special case of $\theta = 90$ degrees, i.e. a transverse crack,

$$\bar{K}^* = \sqrt{f_1^2 + a_{00}(2\frac{r^*}{a})f_0^2 + 2a_{10} \sqrt{2\frac{r^*}{a}} f_1 f_0} \sigma_{\infty} \sqrt{\pi a} . \tag{4.20}$$

Thus, there are biaxial effects modulated by the size of r^* .

If brittle failure is assumed, (4.19) becomes:

$$\bar{K} = \sqrt{f_1^2 \sin^4 \theta + 2a_{66}f_2^2 \sin^2 \theta \cos^2 \theta} \sigma_{\infty} \sqrt{\pi a}$$

or

$$\bar{K} = \sqrt{K_I^2 + 2a_{66}K_{II}^2} \tag{4.21}$$

Computation of K Effective

The values for K_0 , K_I , and K_{II} , may be found as follows. Using a finite element analysis, a plot of $\sigma_{11}\sqrt{2\pi r}$ versus $\sqrt{2\pi r}$, at $\phi = 0$

degrees can be made. Extrapolation of the curve to $r = 0$ gives the intercept $-K_I \mu_1 \mu_2$ and the slope σ_0 . From the slope, the value of K_0 may be obtained. Plotting $\sigma_{22} \sqrt{2\pi r}$ versus $\sqrt{2\pi r}$ at $\phi = 0$ and extrapolating to $r = 0$ gives the intercept K_I . Plotting $\sigma_{12} \sqrt{2\pi r}$ versus $\sqrt{2\pi r}$, at $\phi = 0$ and extrapolating to $r = 0$ gives the intercept K_{II} . This can be done for many different geometries. For the edge crack, plots of $K_I/(\sigma_\infty \sqrt{\pi a})$ versus (a/w) give a series of curves for the various geometries. $K_{II}/(\sigma_\infty \sqrt{\pi a})$ and $K_0/(\sigma_\infty \sqrt{\pi a})$ versus (a/w) may similarly be plotted. By curve fitting the data, the stress intensity factor calibration for a particular problem may be obtained.

STRESS INTENSITY FACTOR CALIBRATION

A finite element analysis was performed to give values of K_I and K_{II} for the different specimen geometries at different crack length to width ratios [6]. The values obtained for K_I and K_{II} were non-dimensionalized by dividing by $\sigma_\infty \sqrt{\pi a}$. The finite element results are tabulated in Table 4.1. The calibration was performed by curve fitting plots of non-dimensionalized K_I versus crack length to width ratio.

The solution for the single edge crack in an isotropic material with bending restrained is [19],

$$\frac{K_I}{\sigma_\infty \sqrt{\pi a}} = \frac{5}{[20 - 13(a/w) - 7(a/w)^2]^{1/2}} \quad (4.22)$$

This form of the equation was used to perform the calibration of K_I . It was chosen so that

$$\lim_{(a/w) \rightarrow 1} \frac{K_I}{\sigma_{\infty} \sqrt{\pi a}} = \infty . \quad (4.23)$$

By multiplying (4.22) by an orthotropy factor α [14], the calibration is seen to fit the 90 degree data fairly well in Figure 4.1. Define an effective shear modulus as:

$$G_{\text{eff}} = \frac{E_1 + E_2}{2(1 + \nu_{12})} \quad (4.24)$$

and a shear modulus ratio as:

$$R_G = \frac{G_{\text{eff}}}{G_{12}} . \quad (4.25)$$

Note that for an isotropic material, $R_G = 1$. Using Section 2 material values for Boron/Aluminum, $R_G = 1.33$. An interpolation of the values for α given in [14] gives a value of $\alpha = 0.996$ for Boron/Aluminum. This, of course, indicates that Boron/Aluminum is not highly anisotropic. In addition, slightly modifying the coefficients of (a/w) and $(a/w)^2$ in the denominator of the expression on the right side of (4.22) provides a good fit of the finite element data. A short computer program was written to help determine these coefficients by trial and error. The resulting equation becomes:

$$\frac{K_I}{\sigma_{\infty} \sqrt{\pi a}} = \frac{4.98}{[20 - 12(a/w) - 8(a/w)^2]^{1/2}} . \quad (4.26)$$

An angle dependency was next added to account for the different geometries. This dependency was incorporated into (4.26) giving

$$K_I = \sigma_{\infty} \sqrt{\pi a} \sin^2 \theta f_1 \quad (4.27)$$

where

$$f_1 = \frac{4.98[1 + \beta_1 (\frac{a}{w} \cos \theta)^2]}{[20 - 12(\frac{a}{w} \sin \theta) - 8(\frac{a}{w} \sin \theta)^2]^{1/2}}$$

Notice that (4.27) reduces to (4.26) for $\theta = 90$ degrees. The parameter β_1 was found using a computer program called KCALIBIN.F, and adjusting β_1 by trail and error until (4.27) was found to fit the finite element solution for the three angles. A value of $\beta_1 = 0.7$ was found to be reasonable for all three angles. The plot of $K_I/(\sigma_{\infty} \sqrt{\pi a})$ versus (a/w) in Figure 4.1 shows the finite element data and the result of Equation (4.27).

A similar procedure was used to determine a calibration for K_{II} . Instead of using a handbook solution for K_{II} , the functional form of (4.27) was used giving

$$K_{II} = \sigma_{\infty} \sqrt{\pi a} \sin \theta \cos \theta f_2 \quad (4.28)$$

where

$$f_2 = \frac{0.48[1 + \beta_2 (\frac{a}{w} \cos \theta)^2]}{[1 - 0.6(\frac{a}{w} \sin \theta) - 0.4(\frac{a}{w} \sin \theta)^2]^{1/2}}$$

A value of β_2 was found with the help of a computer program, KCALIBIN.F, which allows a trial and error solution of (4.28) for β_2 . The value found was $\beta_2 = 0.05$. A plot of $K_{II}/(\sigma_\infty \sqrt{\pi a})$ versus (a/w) in Figure 4.2 shows the finite element data and equation (4.28).

Note that in both the K_I and K_{II} calibrations, the range of fitting the data is from $(a/w) = 0$ to $(a/w) = 3$, since the fatigue tests had a range of (a/w) on this order. Also note that equations (4.27) and (4.28) do not fit the finite element data perfectly. A certain amount of variation in K from the finite element data exists at each (a/w) , so the fit is judged to be sufficient.

CRACK GROWTH PREDICTION

It is necessary to determine a value of a_{66} so that all the baseline fatigue data collapse onto a single curve. The Paris Law constants are determined from a linear least squares fit of this curve.

Determination of a_{66}

The baseline data for the three angles is presented on a $\log_{10} da/dN$ versus $\log_{10} \sigma \sqrt{\pi a}$ plot in Figure 4.3. The data were reduced using MAKEFILE.F. Also using MAKEFILE.F, the values of a_{66} in (4.21) were varied until the curves fall onto each other. This single curve is presented in Figure 4.4. It corresponds to a value of $a_{66} = 6.00$. Notice that at large values of K effective in the 15 degree data there is a tendency for the curves to decrease in slope. It is possible that at these points, the effect of the grips becomes an important factor in the fatigue crack growth.

It is of interest to compare the fatigue crack growth data for B/Al with the fatigue crack growth data for bulk 6061 aluminum, the composite matrix. Plotted in Figure 4.4 are data for 6061-T651 aluminum from [20]. This material was chosen as it is the only 6061 aluminum fatigue data known. The heat treatment most likely changes the fatigue crack growth of the material compared to the non-heat treated material, but at least some idea of the behavior can be ascertained. Note that the slope of this curve is much less than that of B/Al. This indicates that the fatigue crack growth in 6061-T651 aluminum is slower than in B/Al for large $\Delta\bar{K}$ and more rapid for small $\Delta\bar{K}$.

Paris Law Parameters

A linear least squares fit of the B/Al data in Figure 4.4 was performed using MAKEFILE.F to obtain the Paris Law constants. The solid line in Figure 4.4 represents this fit. Recall,

$$\frac{da}{dN} = c\Delta\bar{K}^n$$

The constants for B/Al are $c = 2.6137 \times 10^{-34}$ and $n = 6.88405$. For comparison, a linear least squares fit of the 6061-T651 aluminum, represented by the dashed line in Figure 4.4, gives Paris Law constants of $c = 2.0568 \times 10^{-19}$ and $n = 3.37116$.

Computer Modelling

A computer program called PRED.F was written to predict the crack growth with the specimen geometry and loading conditions as input. It employs a Runge-Kutta method to solve the above equation.

for the dependent variable, N, by incrementing the independent variables, a. In order to minimize truncation errors in the predicting program, the Paris Law was rewritten in the form

$$\frac{da}{dN} = [CA\bar{K}]^n \quad (4.29)$$

The values of C and n are then $C = 1.3233 \times 10^{-5}$ and $n = 6.88405$. Using this predicting capability, the baseline crack length versus cycles curves were redrawn showing the model. In each case, the Paris Law constants used were determined from the least squares fit of the log-log plot for that particular test.

The 90 degree constants are as follows. For specimen A10, the constants are $C = 1.5102 \times 10^{-5}$ and $n = 7.47953$. For specimen C2, the constants are $C = 1.7273 \times 10^{-5}$ and $n = 8.28452$. For specimen C3, the constants are $C = 1.8503 \times 10^{-5}$ and $n = 8.80869$. The crack length versus cycles curves for A10, C2, and C3 are shown in Figure 4.5. The log-log plots for these tests are shown in Figure 4.6.

The 45 degree constants are as follows. For specimen D1, the constants are $C = 8.5495 \times 10^{-6}$ and $n = 5.22642$. The crack length versus cycles curve for D1 is shown in Figure 4.7. The log-log plot is shown in figure 4.8.

The 15 degree constants are as follows. For specimen C8b, the constants are $C = 1.1377 \times 10^{-5}$ and $n = 6.22253$. For specimen C9, the constants are $C = 9.1258 \times 10^{-6}$ and $n = 5.62048$. The crack length versus cycles curves for C8b and C9 are shown in Figure 4.9. The log-log plots for these tests are shown in Figure 4.10.

Note that the quality of the predictions is best for the 90 degree data and becomes less accurate for the 45 and 15 degree data. This is because the complete range of the data was used in each least squares fit to determine C and n. Since the Paris Law is valid only in the linear region, the beginning and ending $da/dN - \Delta\bar{K}$ data should be omitted in the fit. The resulting predictions should be more accurate.

DISCUSSION

The formulation of an effective stress intensity factor was successful in correlating the baseline fatigue data for angles of 90, 45, and 15 degrees. The 15 degree baseline crack growth appears to retard as the crack approaches the fixed grips. This is because the 15 degree crack growth model is the least accurate; see Figures 4.1 and 4.2. The fatigue crack growth in B/A1 is more rapid than in the bulk 6061-T651 aluminum for large $\Delta\bar{K}$ and slower for small $\Delta\bar{K}$.

Table 4.1 Summary of finite element data for SIF calibration

Angle (Deg)	Stress (psi)	a (in)	w (in)	$\frac{a}{w}$	K_I (psi- $\sqrt{\text{in}}$)	K_{II} (psi- $\sqrt{\text{in}}$)
90	5000	0.50	3.0	0.167	7068	0
90	5000	1.00	3.0	0.333	11075	0
90	6000	1.50	3.0	0.500	18807	0
90	5000	2.00	3.0	0.667	21923	0
45	4000	2.12	12.0	0.177	4400	2625
45	4000	2.12	3.0	0.707	8769	4625
45	4000	2.12	2.25	0.943	11933	5250
15	4000	5.80	15.0	0.386	2331	2250
15	4000	5.80	9.0	0.644	2331	2500
15	4000	5.80	3.0	1.932	3552	3875

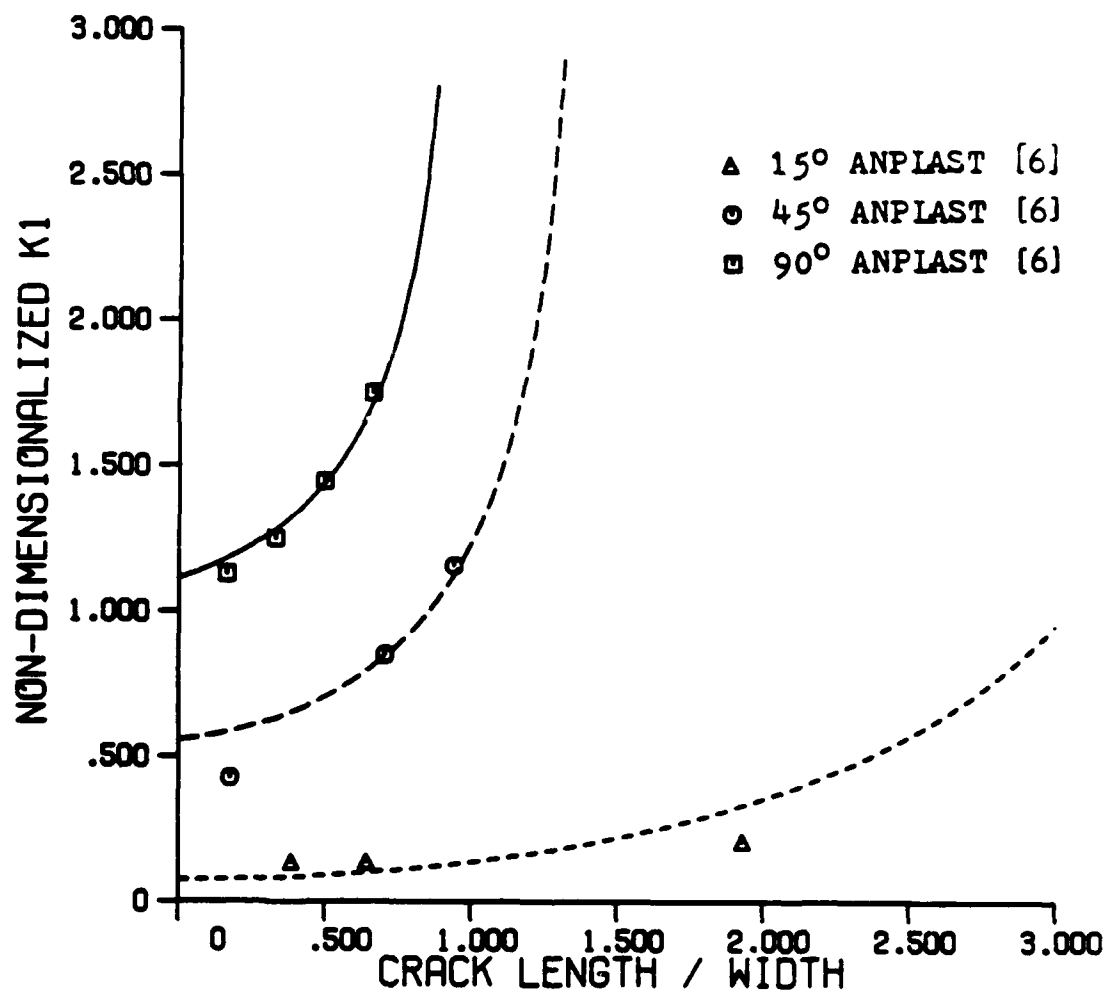


Figure 4.1 $K_I/\sigma\sqrt{\pi a}$ versus (a/w) . The lines represent Equation (4.27).

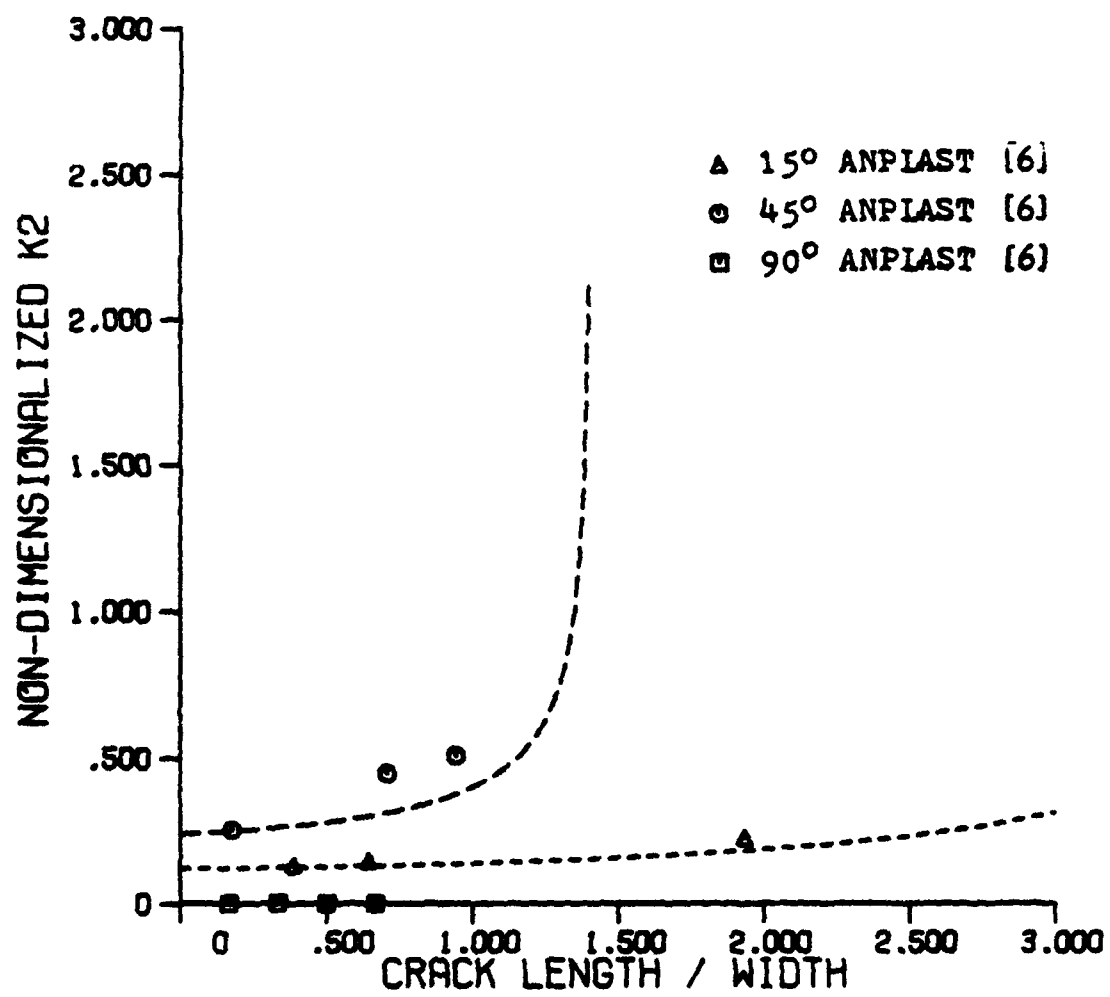


Figure 4.2 $K_{II}/\sigma\sqrt{\pi a}$ versus (a/w) . The lines represent Equation (4.28).

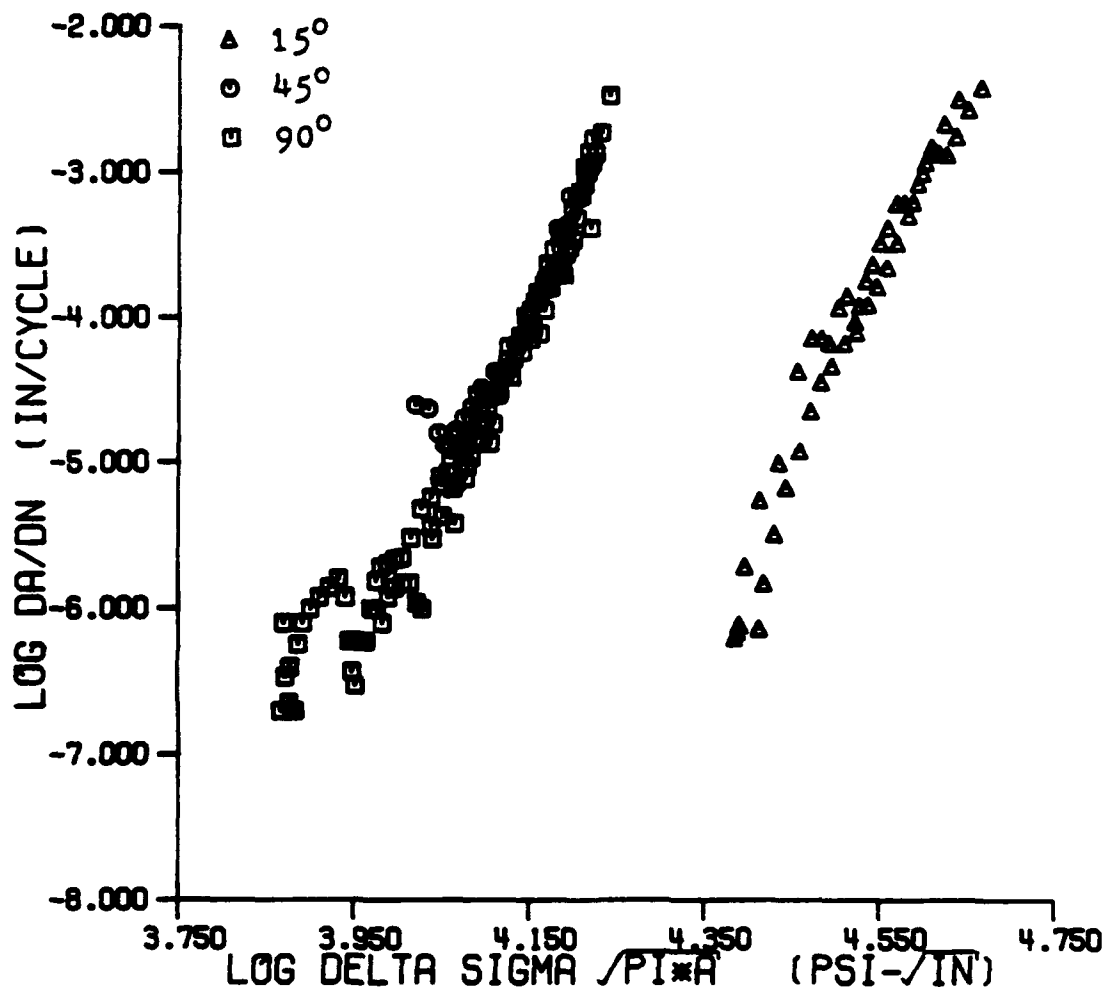


Figure 4.3 $\log_{10} da/dN$ vs $\log_{10} \sigma \sqrt{\pi a}$ for the 90, 45, and 15 degree baseline fatigue data .

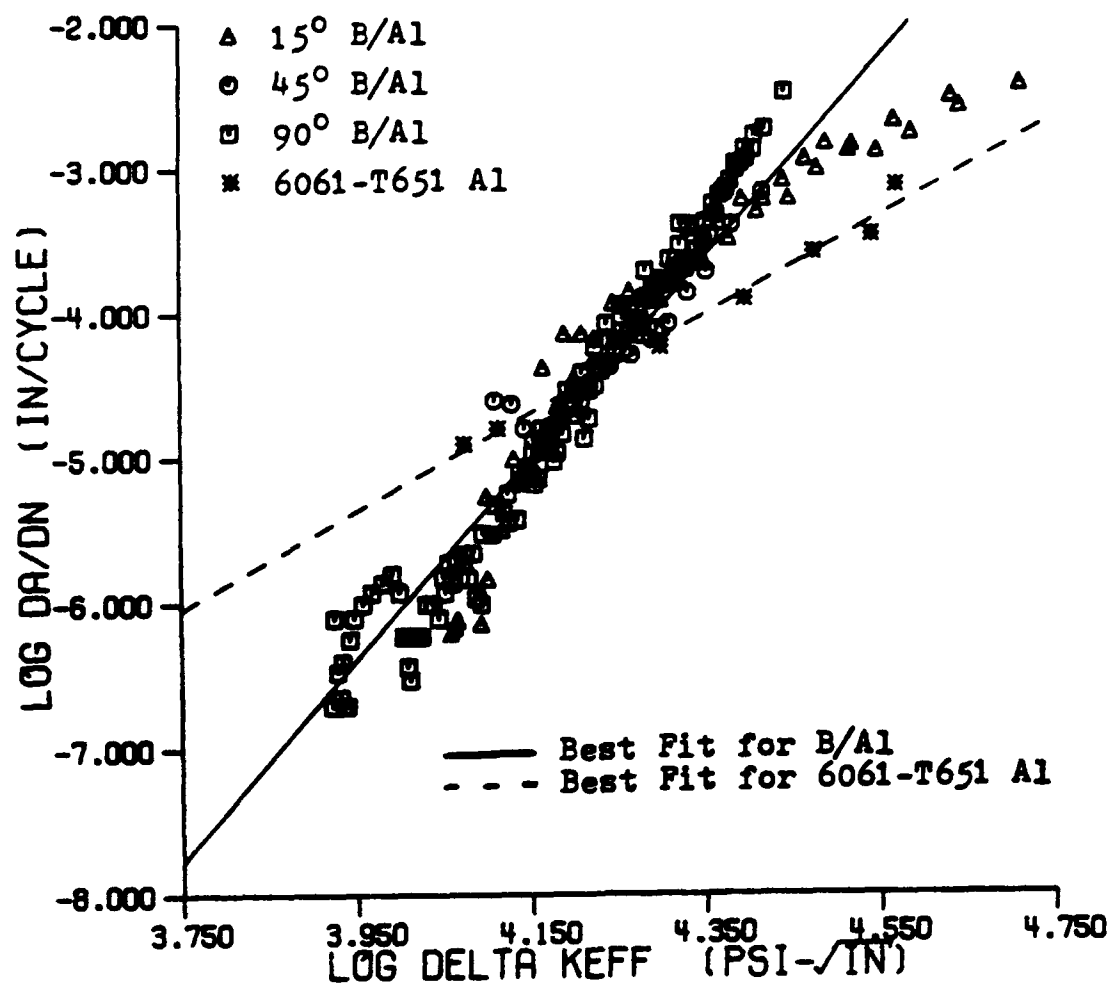


Figure 4.4 $\text{Log}_{10} da/dN$ vs $\text{Log}_{10} \bar{K}$ for the 90, 45, and 15 degree baseline fatigue data. Notice that the three sets of data collapse onto a single curve. The data from 6061-T651 aluminum is shown for comparison.

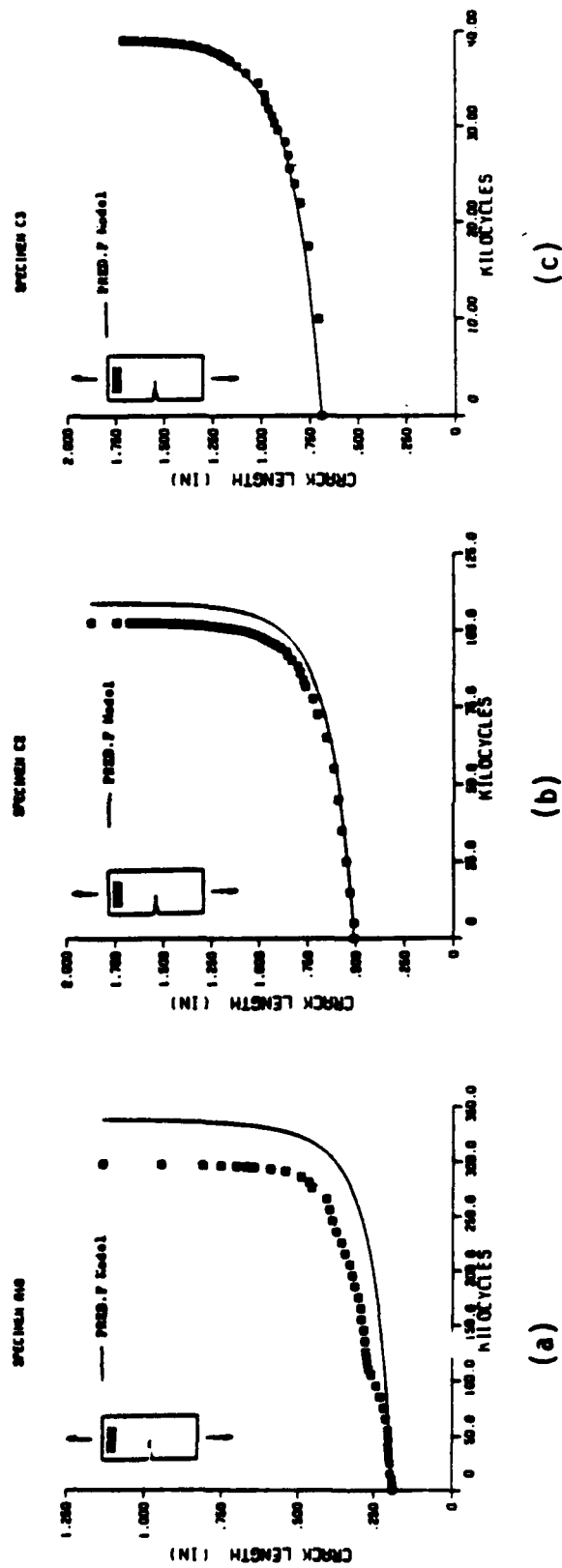


Figure 4.5 Crack growth data for 90 degree baseline tests.
 (a) Specimen A10 - $\Delta\sigma = 9537$ psi, $R = 0.01$.
 (b) Specimen C2 - $\Delta\sigma = 6430$ psi, $R = 0.03$.
 (c) Specimen C3 - $\Delta\sigma = 7280$ psi, $R = 0.03$.

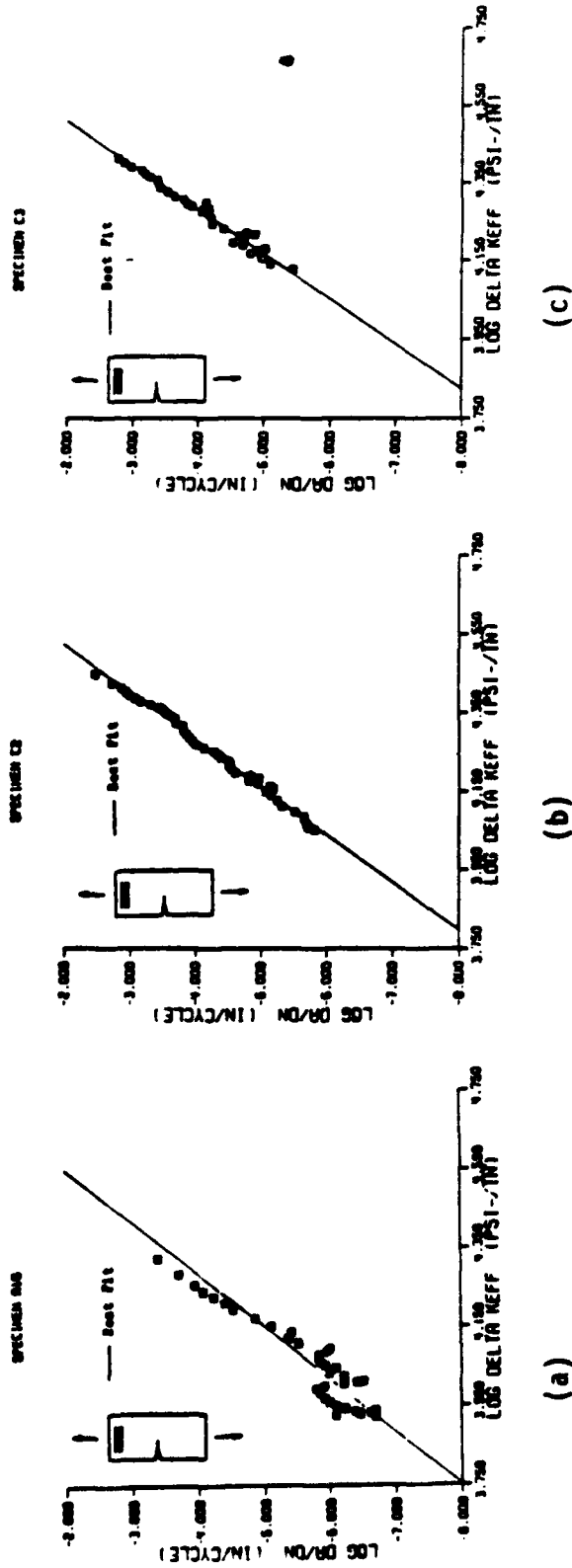


Figure 4.6 Crack growth rate data for 90 degree baseline tests.
 (a) Specimen A10 - $\Delta\sigma = 9537$ psi, $R = 0.01$.
 (b) Specimen C2 - $\Delta\sigma = 6430$ psi, $R = 0.03$.
 (c) Specimen C3 - $\Delta\sigma = 7280$ psi, $R = 0.03$.

SPECIMEN D1

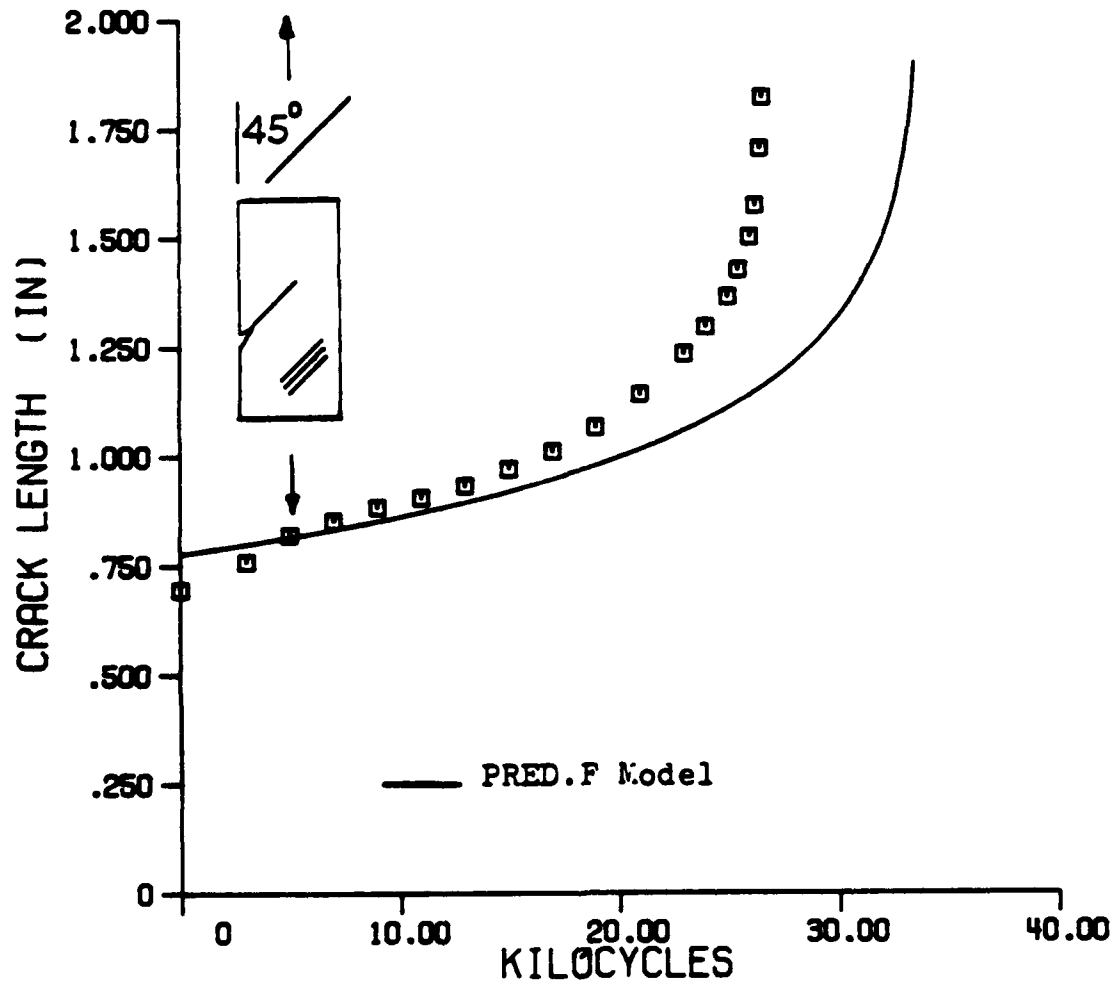
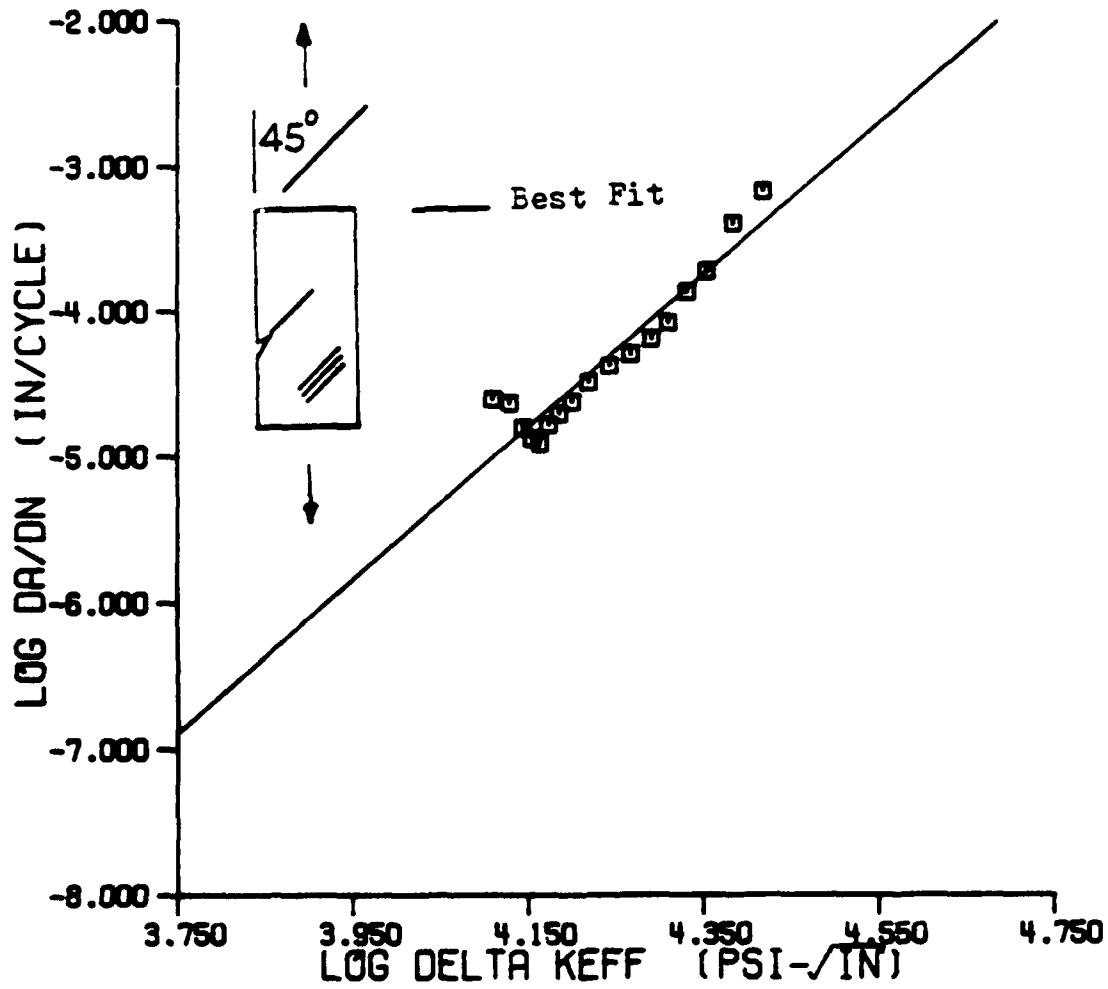


Figure 4.7 Crack growth data for 45 degree baseline specimen D1. $\Delta\sigma = 6,800$ psi, $R = 0.03$.

SPECIMEN Q1



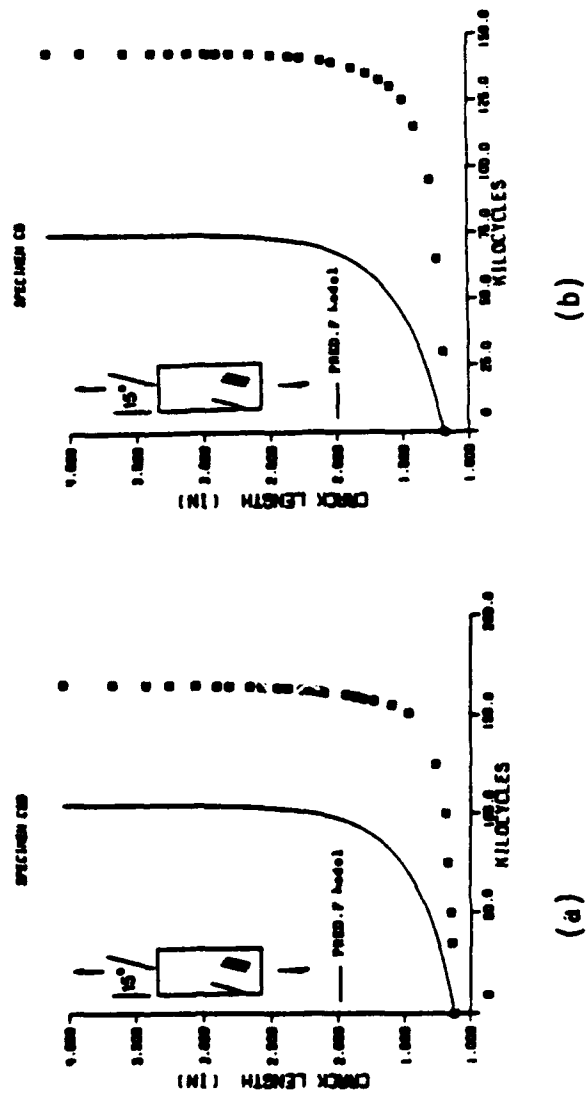


Figure 4.9 Crack growth data for 15 degree baseline tests.
 (a) Specimen C8b - $\Delta\sigma = 12,800$ psi, $R = 0.02$.
 (b) Specimen C9 - $\Delta\sigma = 13,300$ psi, $R = 0.01$.

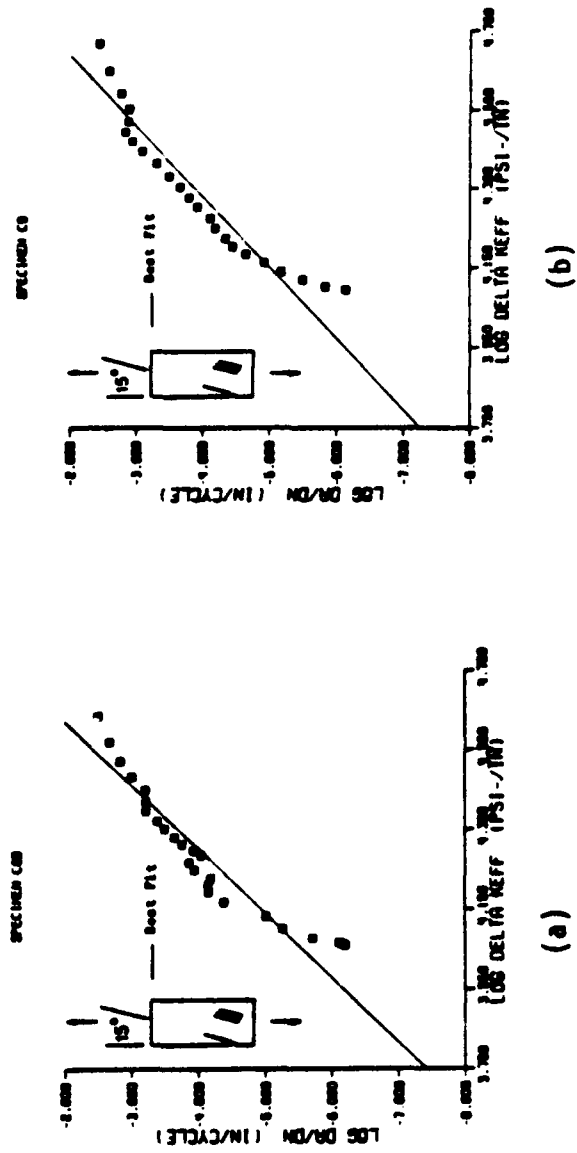


Figure 4.10 Crack growth rate data for 15 degree baseline tests.
 (a) Specimen C8b - $\Delta\sigma = 12,800$ psi, $R = 0.02$.
 (b) Specimen C9 - $\Delta\sigma = 13,300$ psi, $R = 0.01$.

SECTION 5: OVERLOAD TESTS

In this section, the effects of a single tensile overload are investigated for 90, 45, and 15 degree cracks. Six overload tests were performed on the 90 degree specimens, two on the 45 degree specimens, and three on the 15 degree specimens.

Cracks were grown as in the baseline tests and crack length versus cycles data were collected. Overloads were applied after the crack grew to a length such that the overload would not cause net section yielding (see Figure 5.4). The overloads were applied by manually adjusting the span on the MTS machine. The load was raised from the mean cycling load to some factor above the maximum cycling load. The load was then lowered to the minimum cycling load and subsequently raised back to the mean cycling load. Cyclic loading at the previous limits was continued and crack length versus cycles data were collected.

A correlation of the overload effects was performed so that different specimen orientations could be compared.

90 DEGREE OVERLOAD TESTS

Overloads of 1.25, 1.35, 1.45, two 1.5's, and an attempted 2.0 times the maximum cyclic loading were performed on specimens C1, C4, C5, A11, A12, and A13, respectively.

Specimen A11 was the first of two 1.5x overload tests. A maximum cyclic stress of 8,433 psi and minimum of 105 psi was used to grow the

crack to a length of 0.211 inch. This crack extension took 43,000 cycles. The maximum cyclic stress was raised to 9500 psi for 29000 cycles and the crack grown to a length of 0.260 inch. A 1.5x overload was applied with a maximum stress of 14,250 psi. The previous loading was continued for the remainder of the test. The crack length versus cycles data is plotted in Figure 5.1. Since it was difficult in this test to determine a baseline portion of the $\log_{10} da/dN$ versus $\log_{10} \Delta K_{eff}$, the Paris Law constants for this test were not determined. In other tests where the baseline portion of the corresponding curve was easily seen, that part was used to compute the constants. The plot of $\log_{10} da/dN$ versus ΔK_{eff} is shown in Figure 5.2.

The second 1.5x overload test was on specimen A12. A maximum stress of 9398 psi and minimum stress of 85 psi were used. When the crack length reached 0.260 inch, a 1.5x overload with a maximum stress of 14,107 psi was given. The rest of the test was conducted using the prior loading. The crack length versus cycles data are shown in Figure 5.1. For this test, the baseline portion of the $\log_{10} da/dN$ versus $\log_{10} \Delta K_{eff}$ was also difficult to determine, so the Paris Law constants were not determined. The plot of $\log_{10} da/dN$ versus $\log_{10} \Delta K_{eff}$ is shown in Figure 5.2.

A 2.0x overload was next attempted on specimen A13. Using the same loading as the test on A12, the crack was grown to a length of 0.301 inch. During the overload, the specimen fractured and no more fatigue data could be collected. The crack length versus cycles data are plotted in Figure 5.1. Since the crack growth was exceptionally sporadic in this test, the Paris Law constants were not determined.

The plot of $\log_{10} da/dN$ versus $\log_{10} \Delta K_{eff}$ is shown in Figure 5.2.

The next overload test was on specimen C1. Using a maximum cyclic stress of 6000 psi and minimum stress of 220 psi, the crack was grown to 1.298 inches in length. A 1.25x overload was then applied with a maximum stress of 7500 psi. The test was continued using the original loading. The crack length versus cycles data are shown in Figure 5.1. The PRED.F model, using the Paris Law constants from the master curve (Figure 4.4), is also shown, starting from the crack length at the overload. A least squares fit of the baseline portion of the $\log_{10} da/dN$ versus $\log_{10} \Delta K_{eff}$ data gives $C = 1.9831 \times 10^{-5}$ and $n = 8.83081$. The plot of $\log_{10} da/dN$ versus $\log_{10} \Delta K_{eff}$ is shown in Figure 5.2.

A 1.35x overload test was carried out on specimen C4. The same minimum and maximum stresses as for specimen C1 were used. When the crack grew to 1.300 inches, the overload was applied with a maximum stress of 8100 psi. The rest of the test used the original loading. The crack length versus cycles data are plotted in Figure 5.1. The PRED.F model using the Paris Law constants from the master curve is also shown. A least squares fit of the baseline portion of the $\log_{10} da/dN$ versus $\log_{10} \Delta K_{eff}$ data gives $C = 1.6600 \times 10^{-5}$ and $n = 7.41472$. The plot of $\log_{10} da/dN$ versus $\log_{10} \Delta K_{eff}$ is shown in Figure 5.2.

The last overload test was a 1.45x overload on specimen C5. The same minimum and maximum stresses as for specimens C1 and C4 were used. At a crack length of 1.302 inches, the overload was applied with a maximum stress of 8700 psi. The test was finished using the previous loading. The crack length versus cycles data are shown in Figure 5.1.

The PRED.F model using the Paris Law constants from the master curve is also shown. A least squares fit of the baseline portion of the $\log_{10} da/dN$ versus $\log_{10} \Delta K_{eff}$ data gives $C = 1.2620 \times 10^{-5}$ and $n = 6.51556$. The plot of $\log_{10} da/dN$ versus $\log_{10} \Delta K_{eff}$ is shown in Figure 5.2.

45 DEGREE OVERLOAD TESTS

Two overload tests of 1.25 and 1.35 times the maximum cyclic loading were performed on specimens D2 and D3, respectively.

The first overload test was a 1.25x overload on specimen D2. A minimum cyclic stress of 200 psi and maximum of 7000 psi was used to grow the crack to a length of 1.323 inches. The overload was applied and the specimen cycled at the pre-overload cyclic stress for the remainder of the test. The crack length versus cycles data are shown in Figure 5.3. The PRED.F model using the Paris Law constants from the master curve is also shown. A least squares fit of the baseline portion of the $\log_{10} da/dN$ versus $\log_{10} \Delta K_{eff}$ data gives $C = 1.2572 \times 10^{-5}$ and $n = 6.37095$. The plot of $\log_{10} da/dN$ versus $\log_{10} \Delta K_{eff}$ is shown in Figure 5.4.

The second overload test was performed on specimen D3 with a 1.35x overload. The same minimum and maximum cyclic stresses as were applied to specimen D2 were used to grow the crack to a length of 1.316 inches. The overload was applied and the specimen cycled at the previous loading. The crack length versus cycles data are shown in

Figure 5.3 The PRED.F model using the Paris Law constants from the master curve is also shown. A least squares fit of the baseline portion of the $\log_{10} da/dN$ versus $\log_{10} \Delta K_{eff}$ data gives $C = 1.5790 \times 10^{-5}$ and $n = 7.98129$. The plot of $\log_{10} da/dN$ versus $\log_{10} \Delta K_{eff}$ is shown in Figure 5.4.

15 DEGREE OVERLOAD TESTS

Three overload tests of 1.25, 1.61, and 1.92 times the maximum cyclic loading were conducted on specimens C10, B29, and B28.

The first overload test was done on specimen C10. A maximum stress of 13,000 psi and minimum of 200 psi was used. When the crack grew to 2.310 inches, a 1.25x overload was applied. The overload stress was 16,250 psi. The specimen was then cycled between the previous loads for the remainder of the test. The crack length versus cycles data are shown in Figure 5.5. The PRED.F model using the Paris Law constants from the master curve is also shown. A least squares fit of the baseline portion of the $\log_{10} da/dN$ versus $\log_{10} \Delta K_{eff}$ data gives $C = 9.7531 \times 10^{-6}$ and $n = 6.12370$. The plot of $\log_{10} da/dN$ versus $\log_{10} \Delta K_{eff}$ is shown in Figure 5.6.

The second overload test was an attempted 2.0x overload on specimen B28. Using the same cyclic loading as for specimen C10, the overload was applied when the crack grew to a length of 2.347 inches. During the overload, ping, indicating fiber breakage, was heard. The load was raised to only 25,000 psi, or 1.92 times the maximum, so that the specimen would not fracture. A crack length measurement was taken immediately following the overload and showed that the crack extended to 2.500 inches in length. Several fiber crossings also took place during the overload. Fatigue testing continued at the previous levels.

The crack length versus cycles data are shown in Figure 5.5. The PRED.F model using the Paris Law constants from the master curve is also shown. A least squares fit of the baseline portion of the $\log_{10} da/dN$ versus $\log_{10} \Delta K_{eff}$ data gives $C = 1.1452 \times 10^{-5}$ and $n = 6.03279$. The plot of $\log_{10} da/dN$ versus $\log_{10} \Delta K_{eff}$ is shown in Figure 5.6.

A third overload test was performed on specimen B29. Using the same cyclic stress levels as specimens C10 and B28, the crack was grown to 2.332 inches. A 1.61x overload with a maximum stress of 20,900 psi was then applied. Some pinging was also audible during this overload, yet there was no fiber crossing in the following fatigue. The crack length versus cycles data are shown in Figure 5.5. The PRED.F model using the Paris Law constants from the master curve is also shown. A least squares fit of the baseline portion of the $\log_{10} da/dN$ versus $\log_{10} \Delta K_{eff}$ data gives $C = 1.1396 \times 10^{-5}$ and $n = 6.10677$. The plot of $\log_{10} da/dN$ versus $\log_{10} \Delta K_{eff}$ is shown in Figure 5.6.

CORRELATION OF OVERLOAD EFFECTS

As seen in the plots of crack length versus cycles and $\log_{10} da/dN$ versus $\log_{10} \Delta K_{eff}$, subsequent to the overload there is an acceleration in the crack growth rate followed by a retardation. This is different from the overload effect on the fatigue crack growth rate in a homogeneous material which usually retards without any prior acceleration [21]. The total change in crack growth rate, i.e., the difference between the maximum and minimum crack growth rates near the overload, is of interest. Also, the change in total life of the overload specimen compared to the prediction is useful.

Change in Crack Growth Rates

The change in the crack growth rate was computed by subtracting the maximum crack growth rate from the minimum near the overload plotted against the (overload factor -1) on a log-log scale in Figure 5.7. Note that the change in crack growth rate generally increases with increasing overload for each geometry. The two 1.5x overloads on specimens A11 and A12 appear to contradict this. Since the $da/dN-\Delta\bar{K}$ plots from these specimens are quite sporadic, the specimens were not used for further analysis. The changes in the crack growth rate are tabulated in Table 5.1.

Change in Life

Since the specimens were tested to near failure, the total life of the specimens is approximately equal to the final cycle count. By subtracting the final prediction cycle from the final cycle count, an estimate of the change in life due to the overload may be found. Note that since the predictions did not always blend in smoothly with the experimental data before the overload, the calculated changes in life are only approximate. The change in life is plotted against the overload factor for the three specimen geometries in Figure 5.8.

For each geometry, the trend appears to be one in which the change in life is negative for small overloads and positive for larger overloads. Thus, for small overloads, the change in life is caused by the acceleration in the crack growth rate and not the retardation. As the overload increases, the retardation effect becomes larger, as there is more plasticity, and the change in life becomes positive. This means that there is an overload which will cause no change in the life.

DISCUSSION

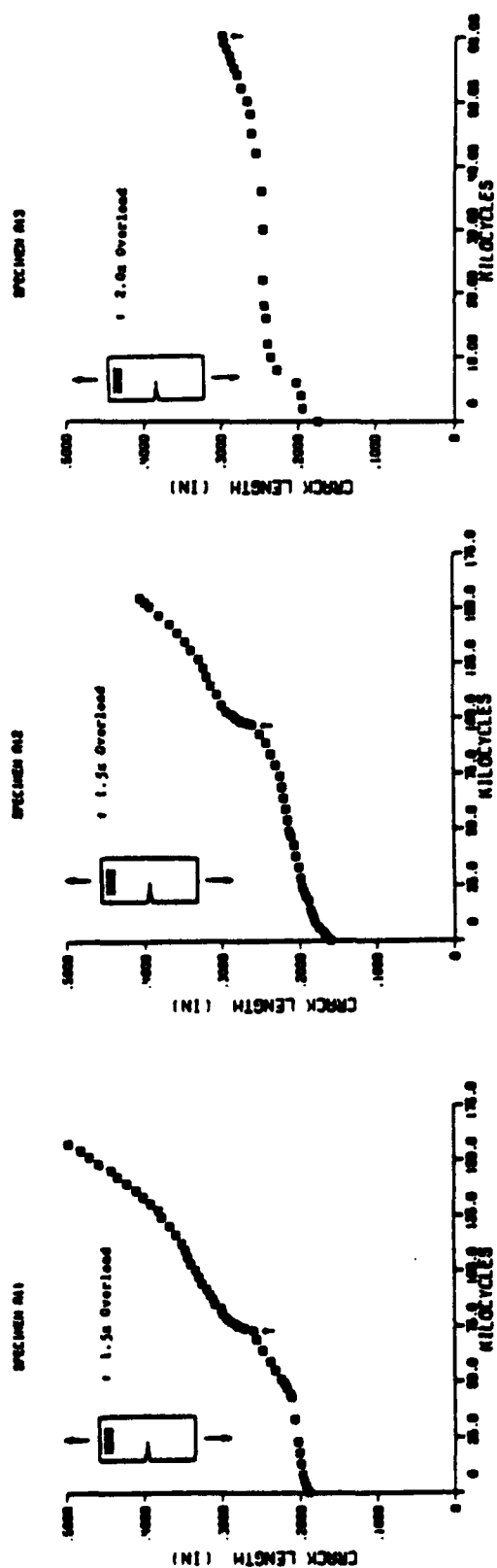
The effect of a single tensile overload on the fatigue crack growth in B/Al is seen to be different from that of a homogeneous metal. Instead of an immediate retardation following the overload, as is usually the case for the homogeneous metal, the B/Al exhibits an acceleration followed by retardation.

The total change in crack growth generally increases with increasing overload for the three specimen geometries.

The change in the total life of the specimen due to the overload depends on the overload. For small overloads, there is usually a net decrease in life, indicating that the predominant effect is due to the acceleration in the crack growth rate. For larger overloads, the retardation effect takes over giving a net increase in life.

Table 5.1 Change in fatigue crack growth rate after overload

Specimen	Angle (Deg)	Overload Factor	Change in da/dn (in/cycle)
C1	90	1.25	9.48×10^{-5}
C4	90	1.35	2.38×10^{-4}
C5	90	1.45	1.64×10^{-4}
A11	90	1.50	9.00×10^{-6}
A12	90	1.50	1.08×10^{-5}
D2	45	1.25	1.11×10^{-4}
D3	45	1.35	2.65×10^{-4}
C10	15	1.25	3.91×10^{-5}
B29	15	1.61	9.71×10^{-5}
B28	15	1.92	7.10×10^{-4}



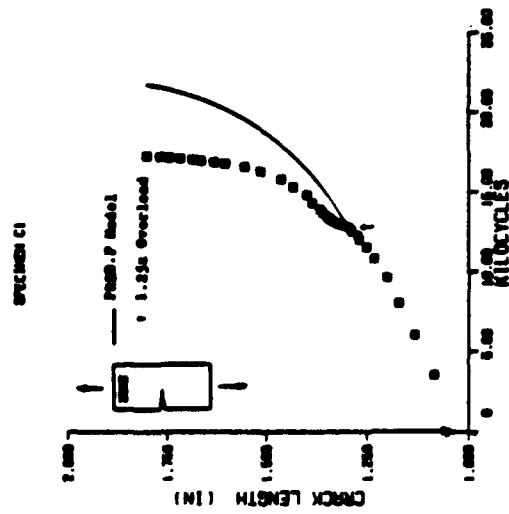
(a)

(b)

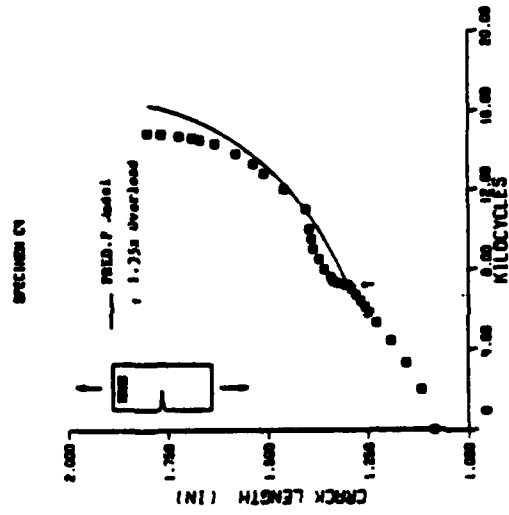
(c)

Figure 5.1 Crack growth data for 90 degree overload tests.

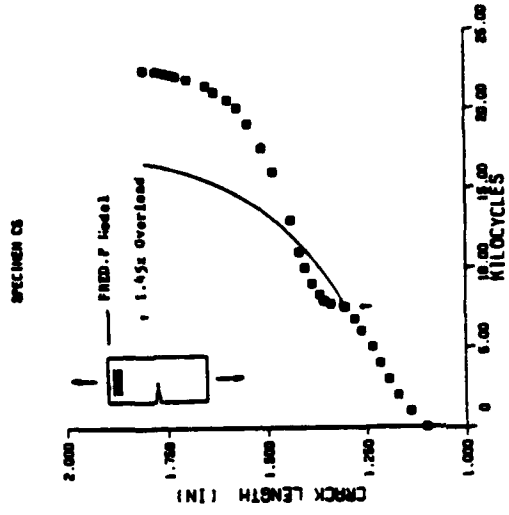
- (a) Specimen A11 - $\Delta\sigma = 9370$ psi, $R = 0.01$.
- (b) Specimen A12 - $\Delta\sigma = 9313$ psi, $R = 0.01$.
- (c) Specimen A13 - $\Delta\sigma = 9313$ psi, $R = 0.01$.
- (d) Specimen C1 - $\Delta\sigma = 5780$ psi, $R = 0.04$.
- (e) Specimen C4 - $\Delta\sigma = 5780$ psi, $R = 0.04$.
- (f) Specimen C5 - $\Delta\sigma = 5780$ psi, $R = 0.04$.



(d)



(e)



(f)

Figure 5.1 continued

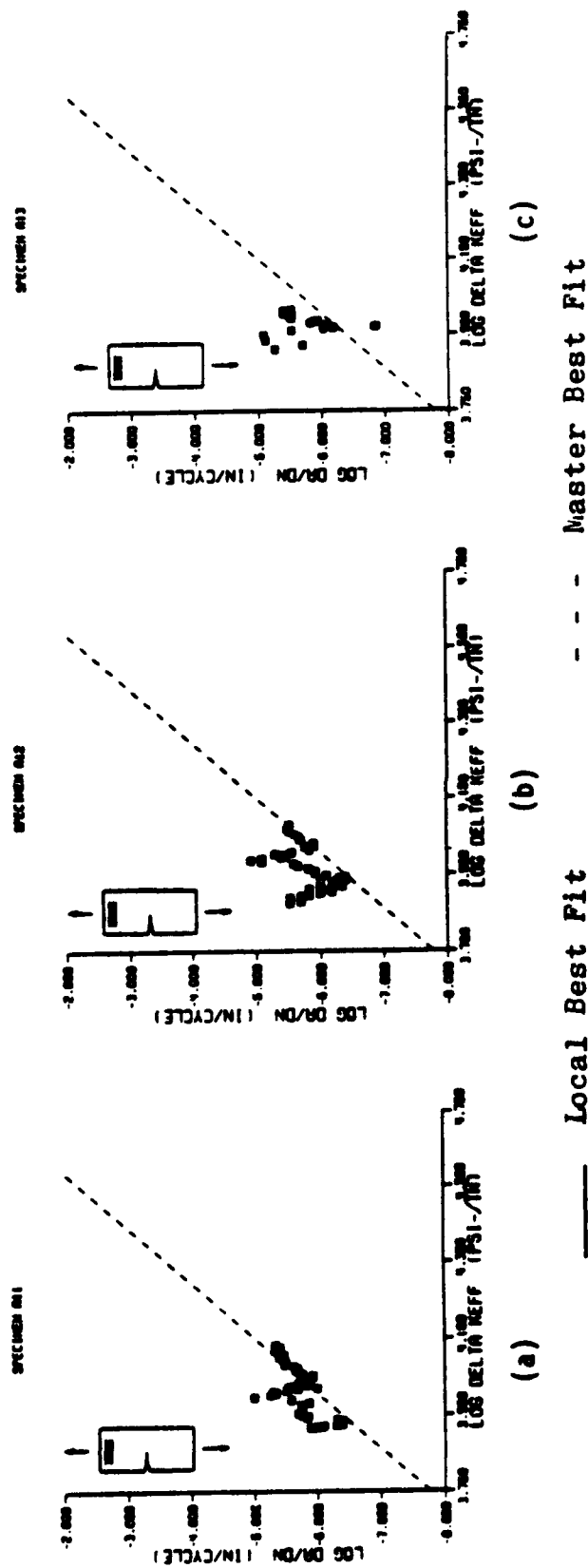


Figure 5.2 Crack growth rate data for 90 degree overload tests.

- (a) Specimen A11 - $\Delta\sigma = 9370$ psi, $R = 0.01$, 1.5x overload
- (b) Specimen A12 - $\Delta\sigma = 9313$ psi, $R = 0.01$, 1.5x overload
- (c) Specimen A13 - $\Delta\sigma = 9313$ psi, $R = 0.01$, 2.0x overload
- (d) Specimen C1 - $\Delta\sigma = 5780$ psi, $R = 0.04$, 1.25x overload
- (e) Specimen C4 - $\Delta\sigma = 5780$ psi, $R = 0.04$, 1.35x overload
- (f) Specimen C5 - $\Delta\sigma = 5780$ psi, $R = 0.04$, 1.45x overload .

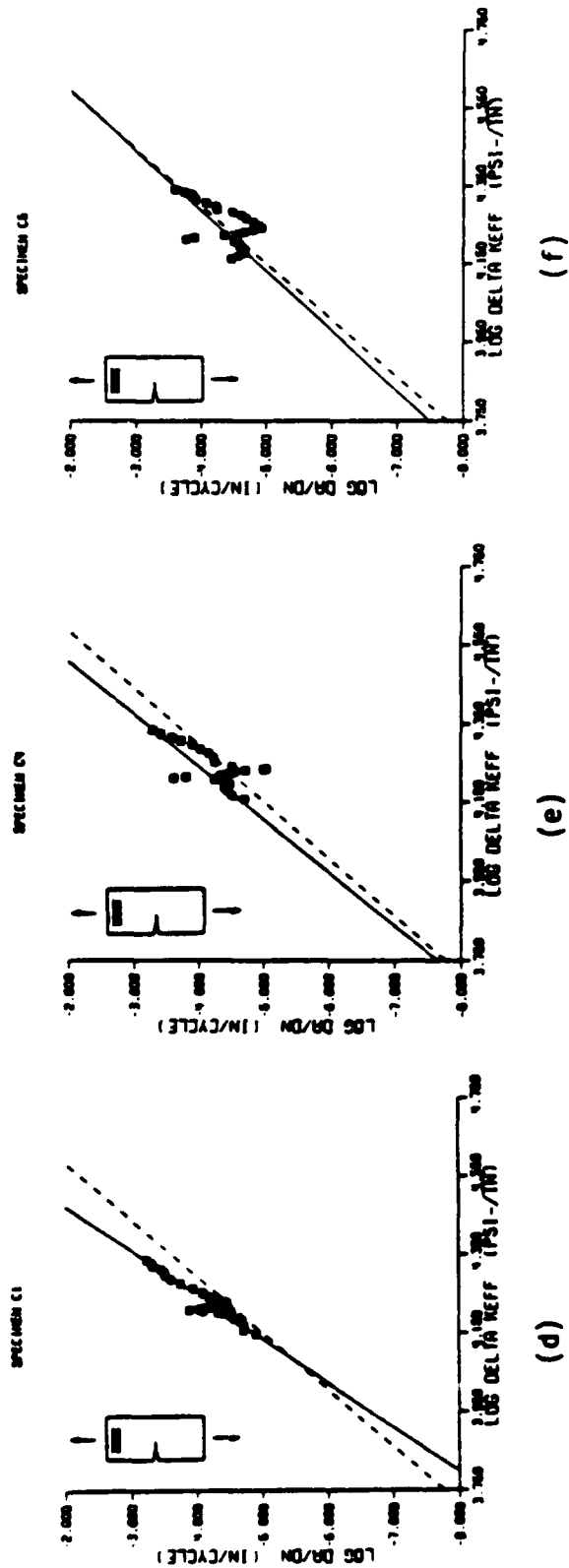


Figure 5.2 continued

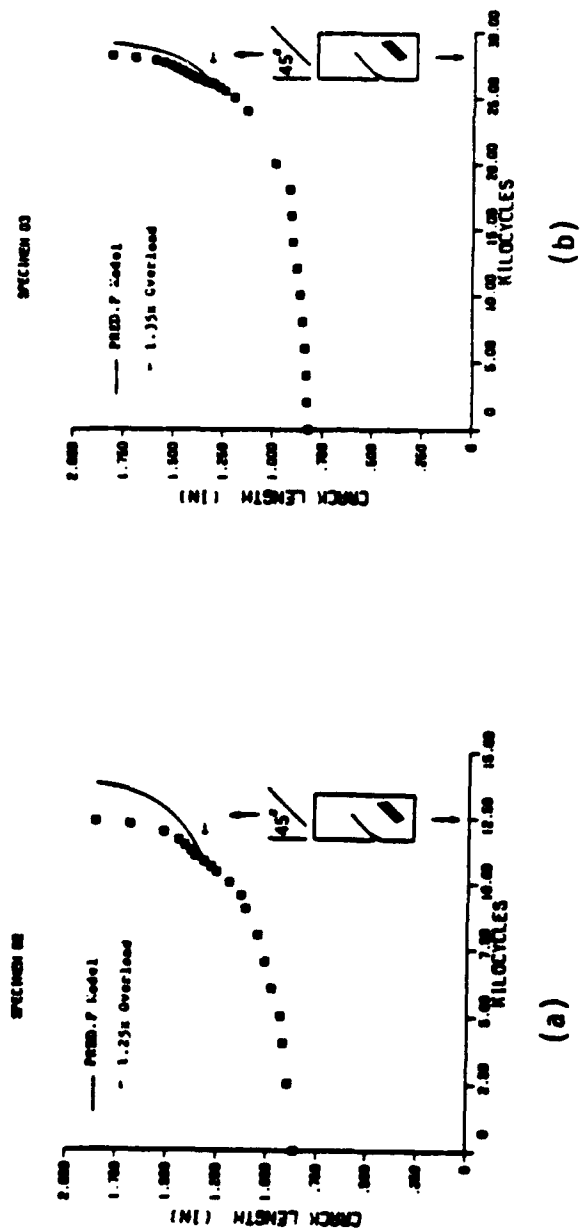
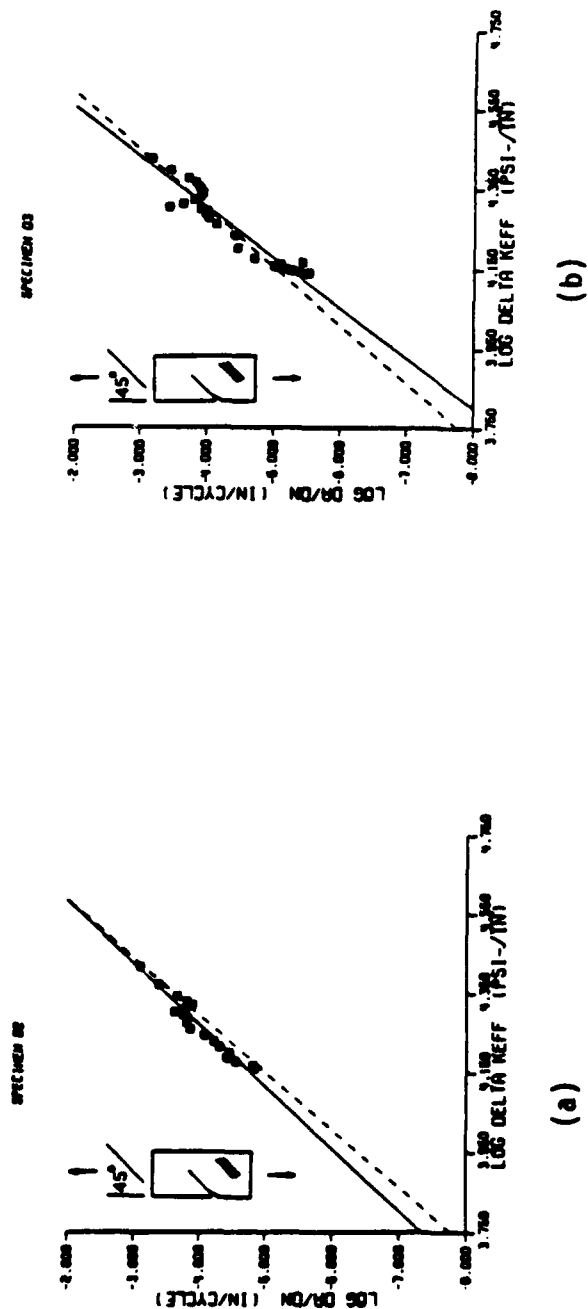


Figure 5.3 Crack growth data for 45 degree overload tests.
 (a) Specimen D2 - $\Delta\sigma = 6800$ psi, $R = 0.03$.
 (b) Specimen D3 - $\Delta\sigma = 6800$ psi, $R = 0.03$.



— Local Best Fit - - - Master Best Fit

Figure 5.4 Crack growth rate data for 45 degree overload tests.
 (a) Specimen D2 - $\Delta\sigma = 6800$ psi, $R = 0.03$,
 1.25x overload
 (b) Specimen D3 - $\Delta\sigma = 6800$ psi, $R = 0.03$,
 1.35x overload

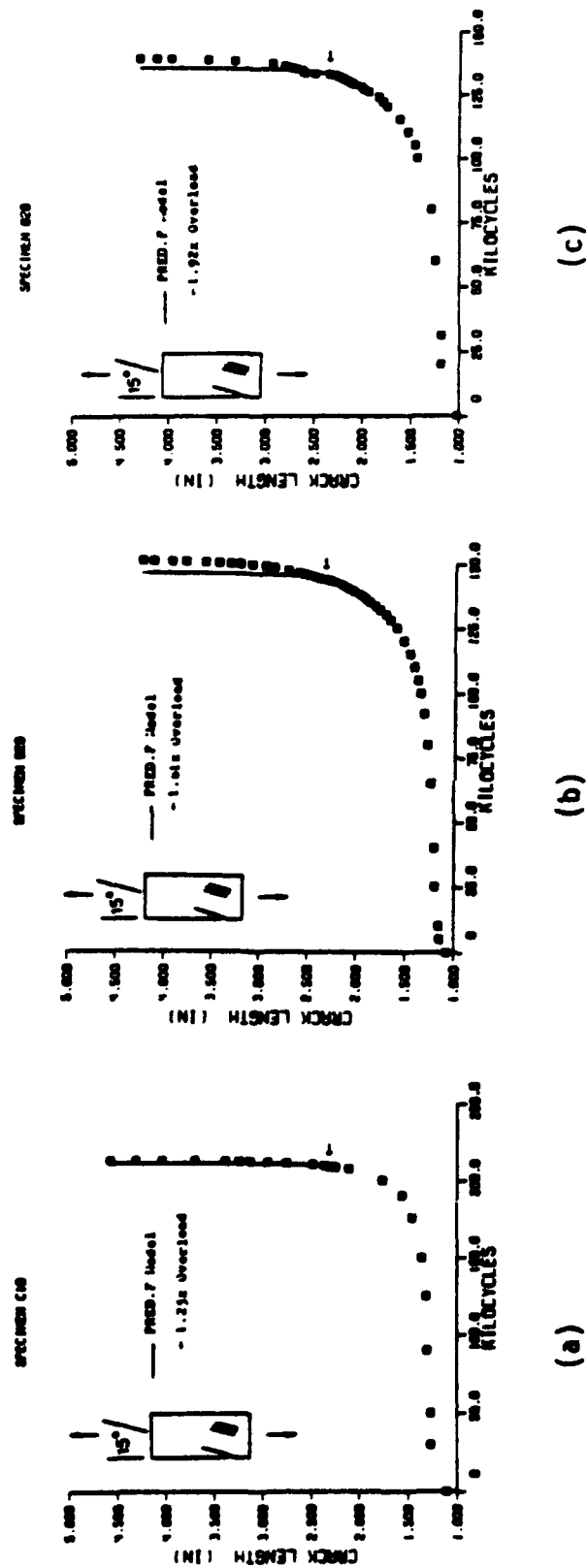


Figure 5.5 Crack growth data for 15 degree overload tests.
 (a) Specimen C10 - $\Delta\sigma = 12,800$ psi, $R = 0.02$.
 (b) Specimen B29 - $\Delta\sigma = 12,800$ psi, $R = 0.02$.
 (c) Specimen B28 - $\Delta\sigma = 12,800$ psi, $R = 0.02$.

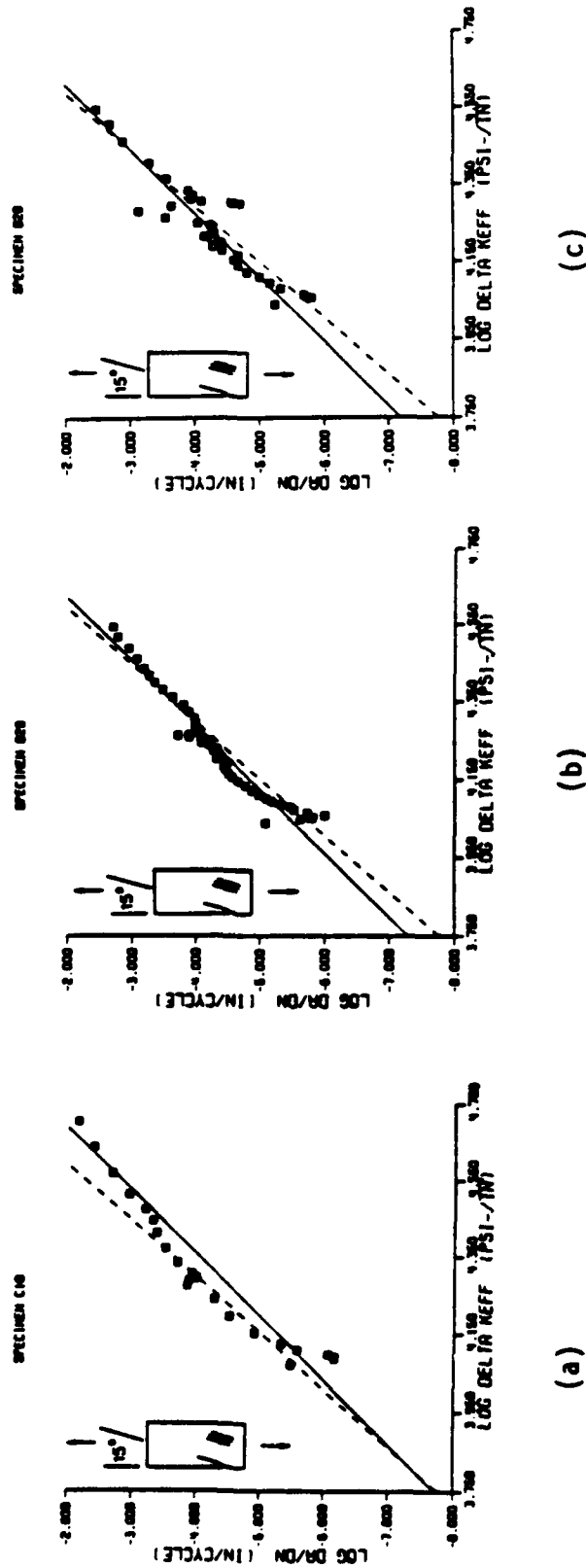


Figure 5.6 Crack growth rate data for 15 degree overload tests.

- (a) Specimen C10 - $\Delta\sigma = 12,800 \text{ psi}$, $R = 0.02$, 1.25x overload
- (b) Specimen B29 - $\Delta\sigma = 12,800 \text{ psi}$, $R = 0.02$, 1.61x overload
- (c) Specimen B28 - $\Delta\sigma = 12,800 \text{ psi}$, $R = 0.02$, 1.92x overload.

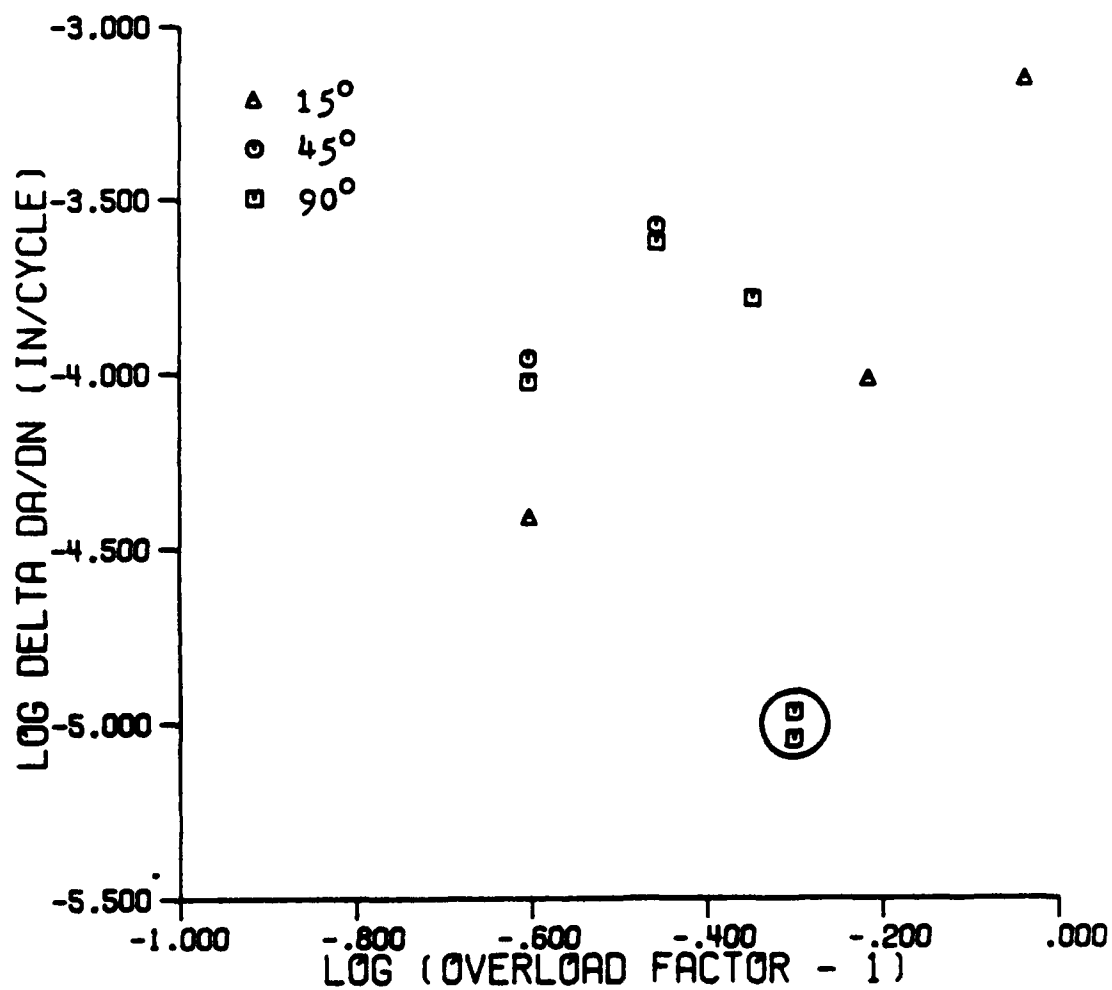


Figure 5.7 Change in crack growth rate as a function of the overload for the three specimen geometries.

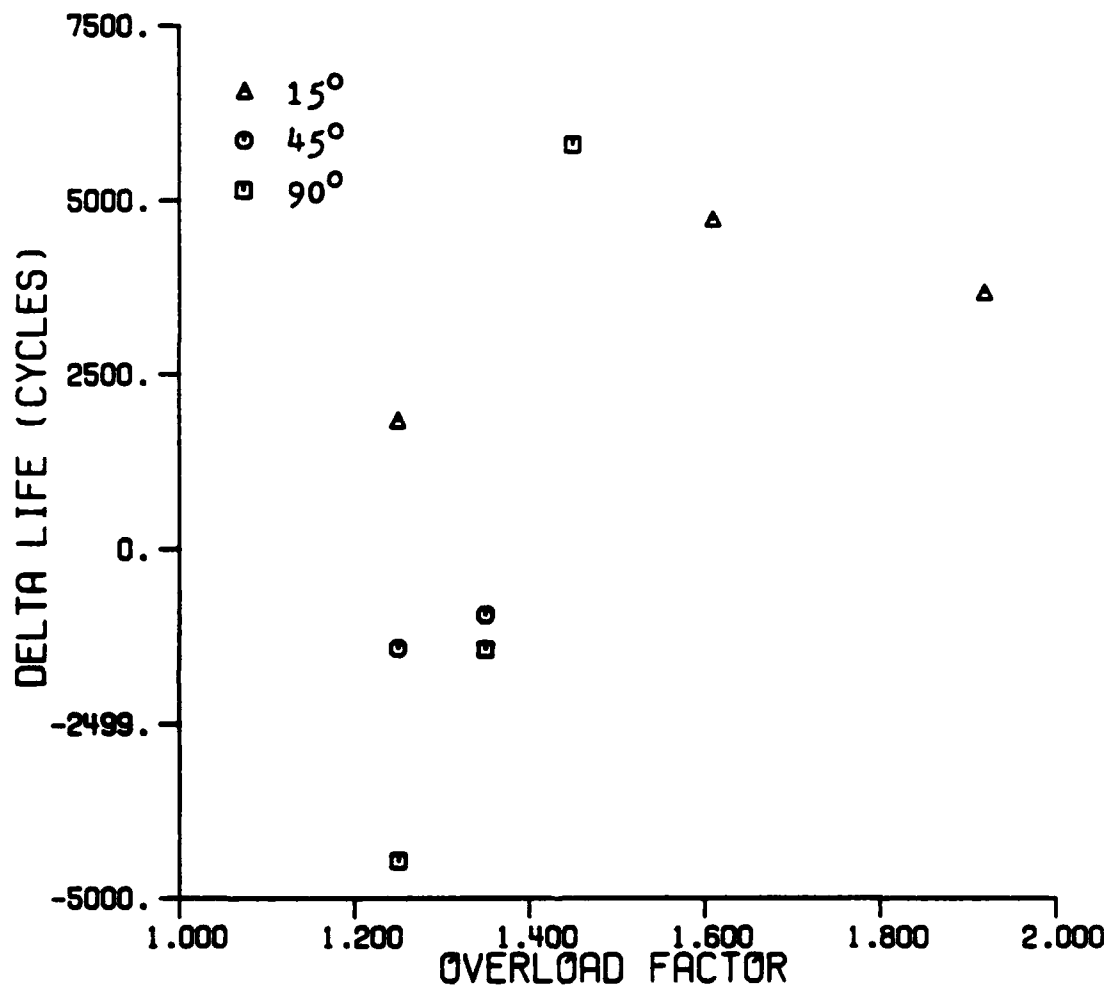


Figure 5.8 Change in life due to the overload as a function of the overload for the three specimen geometries.

SECTION 6: SUMMARY AND RECOMMENDATIONS

The purpose of this research was to develop a model for overload effects on the fatigue crack growth of a B/Al metal-matrix composite.

Recapitulation of Major Results

The first step in this effort was to obtain the mechanical properties. The B/Al composite was modelled as an orthotropic elastic-plastic material and characterized using uniaxial coupon specimens. Note that although no biaxial or compressive tests were performed, the uniaxial analysis models the tapered specimen well. The importance of this test is that it brings to light the constraint effect on the plasticity. The constraint effect is caused by the long elastic fibers hindering the plastic flow of the material. This behavior can, in general, be expected in all but the simple uniaxial coupon specimens. An increase in the slope of the work-hardening curve takes this effect into account in the modelling.

For the multi-axial stress states encountered in the specimen with a centered circular hole and the transverse and oblique crack specimens, the simple UNIAX model could not be used to find the strains. A finite element model, ANPLAST [6], was used instead. The FEM program was seen to do an excellent job in modelling the tapered specimen and a good job with the centered hole. The FEM analysis of the transverse and oblique crack specimens captured the essence of the strain histories.

Differences between the analysis and the data are probably due to cyclic work-softening of the specimen prior to the overload which is not included in the analysis.

Baseline fatigue tests were performed using a 10 Hz constant amplitude sinusoidal loading with a minimum load near zero. All tests were performed in air at room temperature. A number of tests were run with the fibers at 90, 45, and 15 degrees to the load. The crack length versus cycles curves resemble those of homogeneous metals. In off-axis testing, the crack growth is mixed mode.

A finite element analysis [6] was performed to extract the mode I and mode II stress intensity factors for the different geometries. A curve fit of these points was accomplished using the isotropic mode I stress intensity factor as a basis. In this way, the singularity as the projected crack length approaches the width of the specimen remains. A K effective was proposed based on an anisotropic stress intensity factor theory. The K effective formulation allows the baseline data for the three angles to collapse onto a single curve.

A series of overload tests were performed on the same type of specimens used in the baseline study. The fatigue cracks were grown to a predetermined length under a 10 Hz constant amplitude sinusoidal loading. A single tensile overload was applied and the tests continued at the loading prior to the overload. The overloads ranged from 1.25 to 2.0 times the maximum cyclic load. Following the overload, the crack growth rate increased, subsequently retarded and, in most cases, eventually recovered the pre-overload crack growth rate. The change in the crack growth rate generally increased with increasing overload for

the three specimen geometries. For small overloads, there was a net decrease in life and for larger overloads, a net increase in life.

The studies performed in Section 2 on the transverse and oblique crack indicated more plasticity near the crack tip in the transverse crack than the oblique crack. However, the effective stress intensity factors in the transverse and oblique cracks during the overload were 16,706 and 12,626 $\text{psi}\sqrt{\text{in}}$, respectively. A common basis for the comparison is needed. In the transverse case, the effective stress intensity factor was 1.14 times the applied stress. In the oblique case, the effective stress intensity factor was 1.28 times the applied stress. By requiring that the comparison be made at the same effective stress intensity factor, the maximum overload stress in the oblique case corresponds to a overload stress of 11,076 psi in the transverse case. The amount of residual strain in the oblique crack at gage 1 was approximately 700 micro-strain after the overload. By imagining an unloading from 11,076 psi in the transverse case, see Figure 2.17, the residual strain at gage 1 is in excess of 2000 micro-strain. This verifies that the residual strain, which is related to the plasticity, was greater in the transverse case. The retardation effect may thus be correlated with the amount of plasticity.

The acceleration effect, however, cannot be attributed to the plasticity. One must look at the micromechanics at the fiber-matrix interface and relate the damage at the crack tip with the increase in crack growth rate.

Recommendations for Further Study

A more complex characterization of the material should be performed in which shear and biaxial effects are modelled. This could be done by extending the present characterization utilizing data from a series of shear and biaxial tests with the fibers at various orientations, as was done in the uniaxial characterization. It would also be of interest to know the effect of cycling on the material properties.

To fully understand the baseline fatigue behavior, it is recommended that other types of baseline fatigue tests be performed, e.g., biaxial and shear fatigue. This would enable one to determine the a_{11} and a_{12} terms in the K effective formulation.

A series of overload tests at the same K effective should be performed in order to better correlate the amount of overload and crack growth rate between different specimen geometries.

In order to describe the acceleration in terms of the micro-mechanics at the crack tip, chemical etching of the material before and after the overload (in different specimens, of course) should be performed to assess the damage between the fiber and matrix near the crack tip. SEM photomicrographs of the material through the thickness would permit one to get an idea of what causes the acceleration. Such an examination was performed by Kendall [12] on other B/A1 laminates. Photomicrographs might also be useful in determining the grain structure of the matrix before and after the overload. This would help not only in determining the extent of the plasticity but also provide some insight into the nonlinear behavior. The finite element

analysis should be compared with the latter examination.

Sequence effects should be studied to find out what effect a small amplitude cyclic loading followed by a larger one has on the crack growth rate in comparison to a large amplitude cyclic loading followed by a smaller one.

Finally, crack tip opening displacements during fatigue might be correlated with the amount of plasticity.

LIST OF REFERENCES

- [1] Kenaga, D., "Fatigue Crack Growth and Overload Effects in Metal-Matrix Composites," Master Thesis, Department of Aeronautics and Astronautics, Purdue University, 1984.
- [2] Jones, R.M., Mechanics of Composite Materials, Scripta Book Company, Washington, D.C., 1975, pp. 32-54.
- [3] Kachanov, L.M., Fundamentals of the Theory of Plasticity, Mir Publishers, Moscow, 1984, pp. 60-97.
- [4] Mar, J.W. and Lin, K.Y., "Fracture of Boron/Aluminum Composites with Discontinuities," Journal of Composite Materials, Vol. 11, 1977, pp. 405-421.
- [5] Adist, N.R. and Waszczak, J.P., "Fracture Mechanics Correlation of Boron/Aluminum Coupons Containing Stress Risers," Fracture Mechanics of Composites, ASTM STP 593, American Society for Testing and Materials, 1975, pp. 163-176.
- [6] Leewood, A., "Numerical Studies of Problems in Anisotropic Plasticity," Ph.D. Thesis, Department of Aeronautics and Astronautics, Purdue University, 1985.
- [7] Peters, P., "Fracture Mechanical Investigations on Unidirectional Boron/Aluminum and Boron/Epoxy Composites," Journal of Composite Materials, Vol. 12, 1978, pp. 250-261.
- [8] Awerbuch, J. and Hahn, H.T., "Hard Object Impact Damage of Metal Matrix Composites," Journal of Composite Materials, Vol. 10, 1976, pp. 231-257.
- [9] Awerbuch, J. and Hahn, H.T., "K-Calibration of Unidirectional Metal Matrix Composites," Journal of Composite Materials, Vol. 13, 1978, pp. 222-237.
- [10] Awerbuch, J. and Hahn, H.T., "Crack-Tip Damage and Fracture Toughness of Boron/Aluminum Composites," Journal of Composite Materials, Vol. 1979, pp. 82-107.
- [11] Awerbuch, J. and Hahn, H.T., "Crack-Tip Damage and Fracture Toughness of Borsic/Titanium Composites," Tech. Report, Drexel University, 1980.

- [12] Kendall, D.P., "Mechanisms of Fatigue Crack Growth in Boron/Aluminum Laminates," ASTM STP 636, American Society for Testing and Materials, 1977, pp. 47-56.
- [13] Simonds, R.A., "Residual Strength of Five Boron/Aluminum Laminates with Crack-Like Notches After Fatigue Loading", NASA Contractor Report 3815, National Aeronautics and Space Administration, 1984.
- [14] Konish, H.J. Jr., "Mode I Stress Intensity Factors for Symmetrically Cracked Orthotropic Strips," ASTM STP 593, American Society for Testing and Materials, 1975, pp. 99-116.
- [15] Passage Users Manual, Arisbe Communications, Traverse City, MI., 1983.
- [16] Dally, J.W. and Riley, W.F., Experimental Stress Analysis, McGraw-Hill Book Company, New York, 1978, pp. 217-272.
- [17] "Standard Test Method for Constant-Load-Amplitude Fatigue Crack Growth Rates Above 10^{-8} m/cycle," ASTM E647-83, American Society for Testing and Materials, 1983.
- [18] Cherepanov, G.P., Mechanics of Brittle Fracture, McGraw-Hill Book Company, New York, 1979, pp. 71-78.
- [19] Rooke, D.P. and Cartwright, D.J., Compendium of Stress Intensity Factors, Her Majesty's Stationery Office, London, 1976.
- [20] Damage Tolerant Design Handbook, Vol. 3, Metals and Ceramics Information Center, Columbus, Ohio, 1983.
- [21] Fuchs, H.O. and Stephens, R.I., Metal Fatigue in Engineering, John Wiley and Sons, New York, 1980.